Development and Testing of a Tailored Resistance Heating Element for Resistance Welding with the Aim to Achieve Temperature Uniformity at the Welding Interface

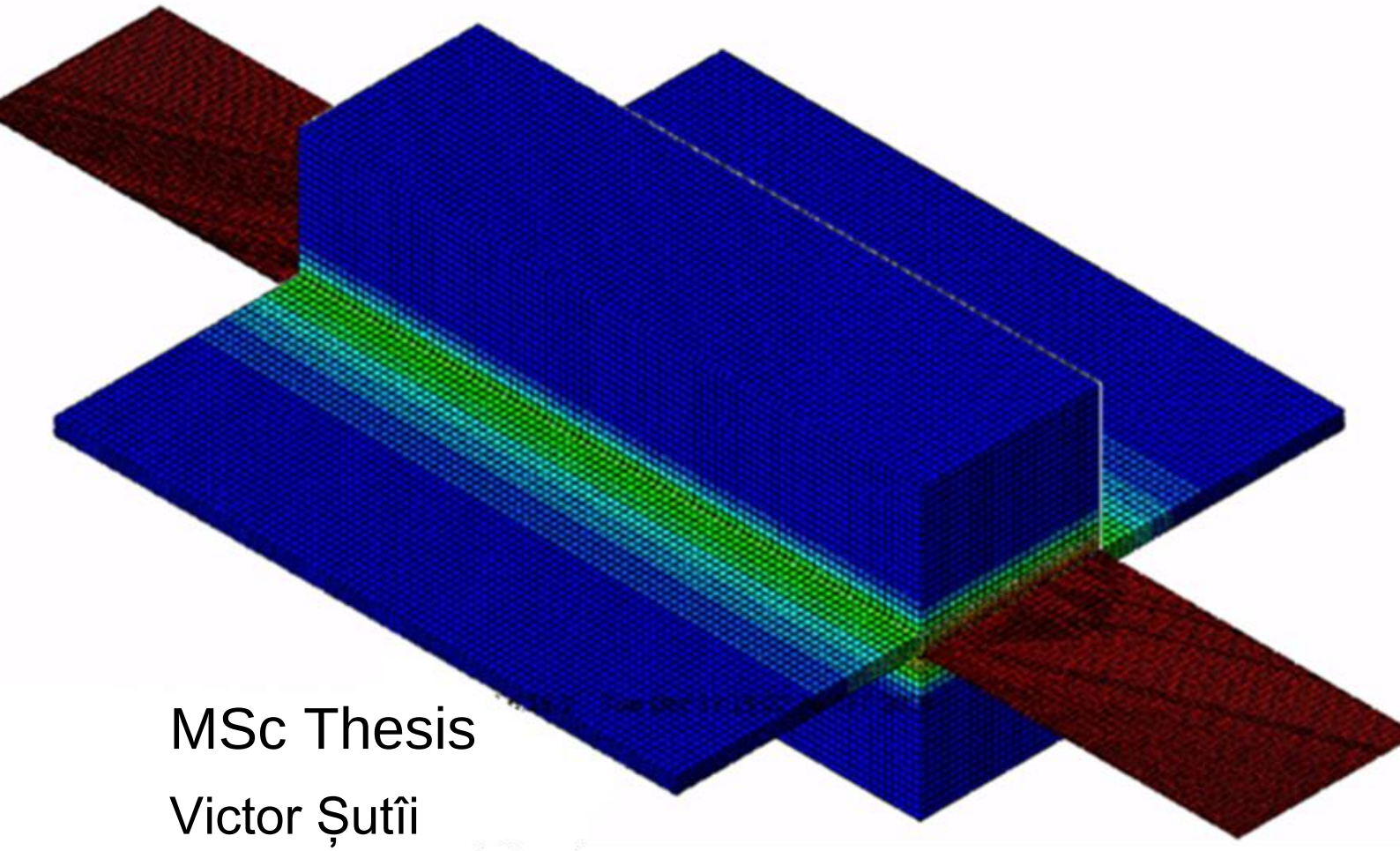

MSc Thesis

Victor Șutîi

CTC we are composites

TU Delft

Development and Testing of a Tailored Resistance Heating Element for Resistance Welding with the Aim to Achieve Temperature Uniformity at the Welding Interface

Master Thesis Report

By

Victor Șutîi

to obtain the degree of Master of Science

at the Delft University of Technology,

to be defended publicly on 27th of March 2020

Student number:	4747208	
Project duration:	January 20, 2019 — February 29, 2020	
Thesis committee:	Dr. I. Fernandez-Villegas	TU Delft, supervisor
	B. Eng. L. Finger	CTC GmbH, supervisor
	Dr. S.J. Garcia	TU Delft
	Dr. C.D. Rans	TU Delft

This thesis is confidential and cannot be made public until December 31, 2025.

CTC we are composites

TU Delft

Acknowledgments

This report is the result of 12 months of work and it is the last step towards my achievement of the Master in Science degree at the Delft University of Technology, Faculty of Aerospace Engineering. I would like to express my gratitude to Dr. I. Fernandez-Villegas for her patient supervision and for the invaluable feedback during the thesis project.
I am indebted to Lennart Finger for accepting to be my daily supervisor and giving me the opportunity to perform my thesis project at CTC GmbH located in Stade, Germany. Especially I am grateful that Lennart had a high level of trust in my ideas and gave me the freedom to steer the project in the direction I thought it was right, and for supporting me during my time at CTC GmbH.
I was lucky to have smart and funny colleagues at CTC GmbH who created a pleasant environment to work. Specifically I want to thank my peers from the “Barcelona” room at CTC GmbH who cheered me up in the stressful periods.
Last but not least I want to thank my family for their unconditional love and support.

Victor Șutîi

AIRBUS

Non-Disclosure Agreement

1. The entire / the marked part of the final thesis of:

   Mr. Victor Sutii

   contains confidential data of Airbus Operations GmbH which may only be used for the issue of the final thesis and the conjoint examination procedures.

   The contents of the thesis may only be made accessible to the supervisors and the members of the examination office.

   The use of the thesis particularly as part of lectures is not allowed without written consent of the Airbus Operations GmbH.

2. Confidential information shall not, either as a whole or in part, be published, reproduced or disclosed to a third party unless the express written consent of Airbus Operations GmbH has been obtained.

3. Secrecy shall be observed in regard to all corporate matters and operations of Airbus Operations GmbH and its affiliated companies which are not publicly known and of which knowledge is obtained by tutoring the student – in written or oral form – either from the student or from Airbus Operations GmbH itself.

4. The declaration of secrecy shall enter into force once this agreement has been signed and shall remain valid for 5 years.

Summary

Resistance welding is one of the best fusion bonding methods to weld thermoplastic composites, because heat is generated exactly at the welding interface in contrast to most other fusion bonding methods. One major problem of the process is uneven temperature distribution along the welding interface due to the boundary conditions changing. Generally, high temperatures are reported at the welding interface edges where the heating element enters into the welding stack and low temperatures are reported at the welding interface edges parallel to the heating element. There are two methods in the literature that focus on decreasing the temperature at the hot edges: air flow cooling and use of electrical camps as heat sinks.

The research in this report focuses on development and testing of a novel heating element which can combat temperature gradients at the welding interface. This can be achieved by tailoring the electrical resistance of the heating element with the aim to increase heat generation at the cold edges and decreasing it at the hot edges of the welding interface. The heating element with the desired resistance pattern was designed and manufactured by laser cutting of stainless steel sheets. As the result of this research two heating element concepts were developed: Concept_1 which is able to provide uniform temperature distribution along the welding interface length (parallel to the heating element) and Concept_2 which is able to provide uniform temperature distribution at the whole welding interface. To find the desired resistance pattern for the heating elements, a transient electrical/heat coupled FEM (Finite Element Method) model was built and experimentally validated.

Welding of carbon fibre reinforced thermoplastics requires electrical insulation of the heating element from the adherends to be welded. In this research the electrical insulation was ensured by sandwiching the heating element between two layers of glass fibre fabric prepreg. Three types of glass fabrics were tested. Results from the LSS (Lap Shear Strength) test (ASTM D5868) showed that the glass fibre fabric has a major impact on the welded joint lap shear strength. The highest LSS results were provided by the joints welded with sized glass fibre fabric with high open area ratio.

The effects of the geometric characteristics of the designed heating elements, such as linear wire density and open area ratio, on the welded joint lap shear strength was studied. The welded joints were tested according to the ASTM D5868 standard. The results showed that the joint strength is independent of the linear wire density. However an increase of LSS with the increase of open area ratio was observed. The LSS increased by 12% for the joints welded with a heating element with 0.7 open area ratio compared to the joints welded with 0.5 open area ratio heating elements. The LSS difference between joints welded with conventional M200 heating element and novel heating element with 0.7 open area ratio was found to be 3% in the favour of the conventional M200 mesh heating element. The main difference between the novel HE and M200 mesh is that the surface of the M200 mesh is wavy while the surface of the novel HE is completely flat. Highest LSS results in the case of M200 heating element are attributed to its wavy surface which creates a more tangled failure path compared to the novel heating element.

Uniform temperature distribution did not show any increase of joint lap shear strength. Instead it has other advantages: lower process temperature, lower welding time, lower fibre movement degree at the welding interface edges and smaller heat affected zone.

Fractography analysis of the tested joints showed that under peel stresses resin/heating element interface was found to be the weakest link while under shear stresses resin/glass fibre interface was found to be the weakest link. Also it was found that the relative size between the heating element wire size and the glass fibre gap size used as electrical insulator has an effect on the failure mode.

The lap shear strength of the joints welded with the novel heating element is comparable to the strength of the joints welded with conventional M200 mesh heating element, with the difference that novel heating elements do not require any cooling devices and fibre movement degree at the welding interface edges is decreased. The results showed that geometric properties of the heating element have an impact on joint lap shear strength. Therefore is recommended to focus further research on optimizing the heating element geometry towards higher LSS.

Contents

List of Figures

List of Tables

List of Abbreviations

CF	Carbon Fibre
CTE	Coefficient of Thermal Expansion
DSC	Differential Scanning Calorimetry
FEM	Finite Element Method
GF	Glass Fibre
HE	Heating Element
IR	Infrared
LSS	Lap Shear Strength
LWD	Linear Wire Density
MTPS	Modified Transient plane Source
OAR	Open Area Ratio
PAEK	Polyaryletherketone
PEI	Polyetherimide
PEKK	Polyetherketoneketone
PPS	Polyphenylene Sulfide
QIL	Quasi-Isotropic Laminate
RT	Room Temperature
TC	Thermocouple
UD	Uni-directional

List of Symbols

Δt	Time increment for FEM transient analysis
(T)	Denotes that material property or physical quantity is temperature dependent
cond	Electrical conductivity of the material
Cp	Material specific heat capacity
d	Wire diameter in the case of mesh heating element
E	Energy
g_l	Heating element gap length
q_w	Heating element gap width
h	Free convection coefficient
I	Current intensity
IPS	Initial power per surface (power per surface generated by the heating element at RT)
k	Material thermal conductivity coefficient
l_w	Longitudinal wire width in the case of the plate heating element
Length	Length
N_long	Heating element longitudinal wires number
N_trans	Heating element transversal wires number
P	Power
PS	Power per surface
PW	Path width, width sum of longitudinal wires
R	Electrical resistance
res	Electrical resistivity of the material
T	Temperature
t	welding time
t_w	Transversal wire width in the case of the plate heating element
Tc	Resin crystallization temperature
Tg	Resin glass transition temperature
th	HE thickness
Tm	Resin melting temperature
U	Voltage
Vol	Volume
Width	Heating element or joint overlap width
Δl	FEM model element size
ε	Emissivity coefficient
ρ	Material mass density
σ	Boltzmann constant
ν	Volumetric fraction

List of Subscripts

-3	Denotes that the property/physical quantity refers to the Concept_2 HE region 3
-4	Denotes that the property/physical quantity refers to the Concept_2 HE region 4
-eq	Denotes that the equivalent property assigned to the FEM modelled HE
-GF	Denotes that the property/physical quantity belongs to GF
-GF/PEKK	Denotes that the property/physical quantity belongs to GF/PEKK prepreg
-GF/PPS	Denotes that the property/physical quantity belongs to GF/PPS prepreg
-iws	Denotes that the property/physical quantity refers to the HE region inside the welding stack
-mesh	Denotes that the property/physical quantity belongs to the mesh HE
-ows	Denotes that the property/physical quantity refers to the HE region out of the welding stack
-PEKK	Denotes that the property/physical quantity belongs to PEKK resin
-plate	Denotes that the property/physical quantity belongs to the plate HE
-PPS	Denotes that the property/physical quantity belongs to PPS resin
-Steel	Denotes that the property/physical quantity belongs to steel
-str	Denotes that the property/physical quantity refers to the strip between two longitudinal wires (Concept_2 HE FEM modelling approach)
-x	Denotes property's orientation (along X axis)
-y	Denotes property's orientation (along Y axis)
-z	Denotes property 's orientation (along Z axis)

1. INTRODUCTION

1.1 BACKGROUND

Carbon fibre reinforced composites are largely used in the aerospace industry nowadays; the trend is to replace metal parts from the airplanes structure with composite parts. The composite weight percentage of the aircraft structure is increasing continuously from 15% in 1987 for the A320 aircraft to more than 50% for the A350 aircraft in 2015 [1]. The main advantages of using composite materials over aluminium for the aircraft structures are the following: carbon fibre composites have higher specific strength that allows lighter design solutions, leading to lower aircraft structure mass and consequently lower fuel consumption.
Based on the matrix type, the composites can be divided into two large categories: thermosets and thermoplastics. The main difference between these two is that thermoplastic composites can be remelted while thermoset composites will keep their solid state up to their thermal degradation point. Presently thermoset composites compared to thermoplastic composites are used more in the aerospace industry because in the past the mechanical properties of thermoset resins were superior to the thermoplastics. However, with the development of the high performance thermoplastics resins such as PEEK, PEKK and PAEK, currently there is a trend in the aerospace industry to switch to the thermoplastic resin based composites.
The advantages of thermoplastic composites over thermosets are the following: the shelf life of the thermoset prepregs is limited and they must be stored in the refrigerators, while the thermoplastic prepregs have an unlimited shelf-life. From the assembly point of view thermoplastics have an outstanding advantage over thermosets. Thermoset parts can be joined by using co-curing, co-bonding or secondary bonding processes. All of three mentioned processes require an autoclave, leading to high production costs and time. Another option is to rivet the parts together, riveting of the continuous carbon fibre reinforced composites has further drawbacks. To rivet two parts first the holes for the rivets must be drilled. During drilling some fibres will be cut, in addition the holes will act as stress concentrators, additionally the dust produced during drilling presents a health hazard. Further galvanic corrosion can occur between the aluminium rivets and the exposed carbon fibres, therefore titanium rivets need to be used instead, which are more expensive and heavier. On the opposite side joining of thermoplastics can be done through welding processes by locally melting the surface of the parts which need to be joined together. Resistance welding has been proven feasible for the industrial environment; it was used by Fokker to weld the leading edge of the A380 aircraft wing made from glass fibre reinforced PPS composite.

1.2 RESISTANCE WELDING

Resistance welding is one of the simplest and most cost efficient fusion bonding techniques. This technology requires a heating element made from electrically conductive material sandwiched between the parts to be welded. The heat necessary to melt the resin at the welding interface is generated by the heating element through the Joule effect when electrical current is applied to it. When the temperature at the interface reaches the melting temperature of the resin the current flow is switched off and the laminates cool down. The pressure is maintained on the welding interface during the whole process in order to impede voids growth and to ensure a good contact between the adherends and the heating element. The heating element remains trapped inside the welded stack, thus it is important to have a good compatibility between the welded laminates and the heating element. A schematic representation of resistance welding is shown below:

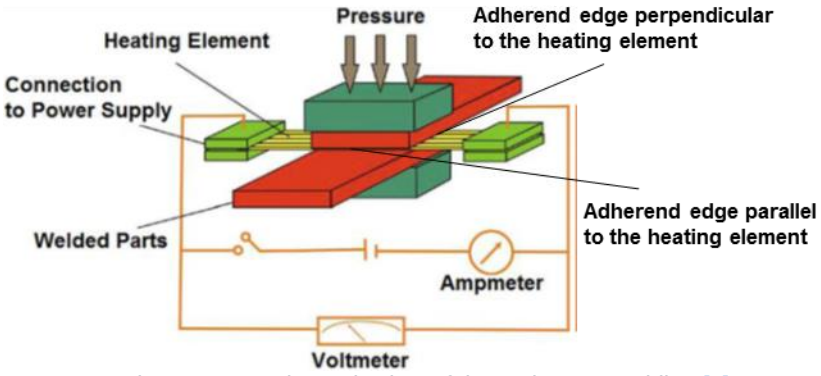

Figure 1.2-1 Schematic view of the resistance welding [2]

The energy generated by the heating element can be easily calculated according to Joule's law with the following formula:

$$E = U \cdot I \cdot t = I^2 \cdot R \cdot t$$

Where: $\boldsymbol{I}$ is the current intensity, $\boldsymbol{U}$ is the current voltage, $\boldsymbol{R}$ is the resistance of the heating element and $\boldsymbol{t}$ is the welding time.

1.3 MOTIVATION

In the frame of the "FUSELAGE OF TOMORROW" project CTC GmbH is looking for an industrialisation concept to weld cleats and clips to the fuselage skin or stringers foot and to the frames. All parts are manufactured from carbon fibre PEKK reinforced laminates. From the literature and from the trials made at CTC GmbH it was found that an issue during the welding is the overheating of the adherends edges perpendicular to the heating element. This might lead to a welded joint with low LSS close to the overheated edges due to the resin degradation. To impede edge overheating, several methods are reported such as active gas cooling of the edges [3] or by using the current contact clamps as a heat sink [4]. Both methods add complexity to the welding set-up. Using current contact clamps as heat sink involves their positioning in the proximity of the welding stack, in function of the welding stack material and of the welding power used, the position of the clamps can vary from less than 1mm [4] to 20 mm [5]. This method worked well in the laboratory conditions welding single lap shear joints, however in the industry, especially in the case of welding cleats and clips to the fuselage skin and frames it might not work since positioning of the clamp in the proximity of the welding stack will be difficult or even impossible due to the geometry of the parts to be joined. The problem with air-cooling is that the temperature of the edges to be cooled is very sensitive to the air flow speed and orientation, thus reproducibility of the welding experiments is problematic. Therefore it was decided to find a strategy to improve temperature distribution on the welding interface by developing a tailored resistance heating element which will increase the temperature uniformity on the welding interface.

1.4 OUTLINE

The report will start with the results from the literature study where background regarding resistance welding process will be provided in Chapter 2, together with the tailored heating element idea presentation, research question and research methodology taken to answer them. In Chapter 3 the experimental set-up, materials and methods used are described. In Chapter 4 the research results will be presented and explained. The report will end with Chapter 5 and 6 where conclusions and recommendation for the future work will be presented.

2. RESISTANCE WELDING OF THERMOPLASTIC CARBON FIBRE REINFORCED COMPOSITES

In this chapter the results of the literature review are presented. According to the topic, it was decided to steer the literature study on the following domains:

- Resistance welding process
- Resistance welding heating elements
- Temperature distribution at the welding interface
- LSS of the joints welded with metal mesh HE (Heating Element).

The main parameters of resistance welding process are: **power input, heating time, welding pressure** [4]. The temperature at the welding interface is dependent on the input power, material properties, welding time and on the boundary conditions. The desired process temperature at the welding interface is used to derive the welding power and the welding time [5, 6, 7]. The process temperature must be higher than the semi-crystalline resin melting point and lower than the resin degradation point. For an amorphous resin the temperature should be higher than the glass transition point and lower than the resins degradation temperature. Dubé [8] suggested a process temperature higher than the compression moulding temperature to ensure a good impregnation of the heating elements. For example the process temperature used to weld CF/PEKK laminates mentioned by M. Dubé [2] is 410 °C and 420 °C [9] [10]. To achieve the process temperatures at the welding interface the moderate input power levels between 70-100 $\frac{kW}{m^2}$. [3, 4, 11, 12, 13] were found in the literature for different resin systems. The power level is dependent on the thermal insulation material used during the welding process.

The role of **pressure** is to ensure an intimate contact between the parts to be joined, allowing the molecular diffusion between them. Another role is to impede delamination and porosities due to residual volatiles trapped in the laminate. The required pressure depends on the laminates to be joined residual stresses and of the trapped moisture or other volatiles inside the laminates. H. Shi [4] developed a model to calculate the required pressure on the welding interface to impede void formation due to fibre de-compaction and due to residual moisture. It was found that the required pressure to stop the void growth due to the volatile moisture is higher than the required pressure to stop the fibre deconsolidation. In the case of GF/PEI 8 HS fabric the minimum applied pressure to achieve void-free laminates is 0.8 MPa. M. Dubé [10, 2] used 1 MPa to weld CF/PEKK laminates built from UD prepregs. On the other hand, too high pressure on the welding interface can lead to fibre movement and to laminate deformation, consequently lowering the lap shear strength of the joint. In the case of welding GF/PEI C. Ageorges [14] noticed a reduction of the lap shear strength for pressure higher than 1.6 MPa.

2.1 METAL MESH HEATING ELEMENT

The metal mesh main parameters are the wire diameter and the open gap width, these parameters are depicted in the Figure 2.1-1:

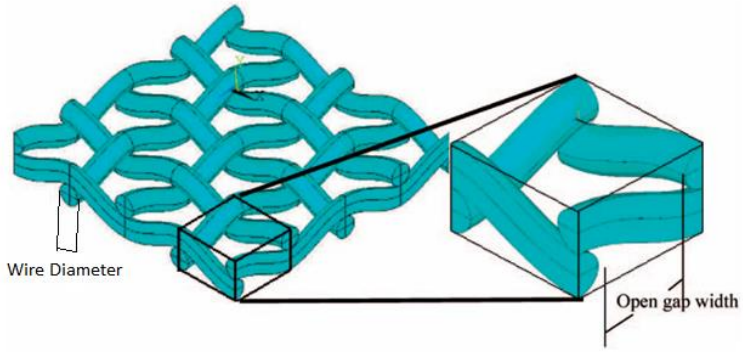

Figure 2.1-1: Stainless steel mesh schematic view [9]

Compared to the CF heating elements the main disadvantage of stainless steel mesh as a heating element is that a foreign material is added in the joint. Instead, stainless steel mesh heating element has numerous advantages over the CF heating element: Good electrical contact between the clamps and the heating element. H.Shi [15] found that contact resistance is independent on the clamping pressure above for clamping pressure values higher than 1 MPa in the case of stainless steel mesh with the wire diameter of 0.04 mm and open gap width of 0.09 mm. It is easier to control the temperature at the welding interface using a metal HE. Unlike carbon fibre heating elements metal heating elements have uniform temperature distribution when they are heated out of the welding [16].
To ensure that at the welding interface enough resin exists to fill the mesh gaps, additional layers of neat resin are added [17, 18, 9]. Alternatively, HE are impregnated with resin prior to the welding process by consolidating them together with neat resin layers. The pressure applied for the HE impregnation is lower than the pressure used to consolidate the laminate in order to avoid resin squeeze out [16]. The last method aids the heat transfer during the welding process, because the intimate contact between the heating element and the resin is achieved prior to the welding process.
An alternative metal instead of stainless steel is copper or bronze. Using bronze or copper as a material for the heating element is tempting in aerospace industry, because copper mesh is also used for the lightning strike protection. However the drawback of copper or bronze compared to stainless steel is the high electrical conductivity. Due to the high conductivity the generated heat through Joule effect is lower compared to stainless steel mesh for the same current and heating element geometry, consequently higher current input is necessary to generate the right amount of energy to achieve the welding temperature at the welding interface. Requena [19] reported a current of 48 A necessary to heat up a bronze mesh heating element up to 350 °C out of the welding stack. The heating element had the following properties: Length 150 mm, Width: 25 mm gap width 0.46 mm, wire diameter: 0.053 mm. While a stainless steel mesh with gap width of 0.08 mm and wire diameter of 0.35 mm reached 350 °C for a current input of 23 A though stainless steel mesh cross-section is twice bigger than the cross section of the bronze mesh. Under constant current input the energy generated through Joule effect by the HE is inverse proportional with the HE cross-section.
High current input becomes an issue when the current generated by the welding machine is limited. However the necessary current input can be decreased by decreasing the width of the heating element. Nonetheless at CTC GmbH resistance welding process is desired to weld clips and cleats, the cleat foot geometry is approximately 10 cm long and 2.5 cm wide, therefore decreasing the HE width is not an option since it is given by the overlap width. However using cooper/bronze as a heating element material might have potential to weld long stringers to the skin, where its high conductivity will become an advantage compared to the stainless steel material. Because this will lead to a lower electrical resistance of the bronze HE compared to a stainless steel HE with a similar geometry. A lower electrical resistance in the case of bronze HE will lead to a lower voltage required to weld. High voltage is one of the problems when welding long joint with stainless steel HE.

2.2 FACTORS INFLUENCING TEMPERATURE DISTRIBUTION AT THE WELDING INTERFACE

Temperature non-uniformity along the welding interface together with the current leakage in the CF laminates were identified as the main factors limiting the size of the welded joint [13]. Villegas [20] mentioned uneven temperature distribution at the welding interface as one of the obstacles to implement the in-situ temperature monitoring based on the relation between the temperature and electrical resistance of the heating element. Shi [17] suggested that a decrease of the temperature gradient at the welding interface will lead to an increase of the lap shear strength of the joint.
The temperature distribution at the welding interface and through the thickness of the adherends to be welded is dependent on three main factors:

- Current leakage
- Boundary Conditions
- Input power level

2.2.1 Effect of Current Leakage on the Temperature Distribution

Current leakage becomes an issue when CF reinforced laminates are welded, it has an impact on the temperature distribution at the welding interface. The temperature at the welding interface and in the welding stack is impossible to control once current leakage occurs. The reason of current leakage is electrical conductivity of the carbon fibres. During the heating process an electrical contact between the heating element and the carbon fibres may occur, this will lead to alternative electrical current flow paths. Therefore a part of the current will flow through the laminates and the overall electrical resistance will have a steep drop, thus the generated heat at the welding interface between the points where current penetrates the CF laminates will decrease, instead the whole welding stack will be heated. Resultantly the temperature in the middle of the welding interface will be lower than temperature of the transversal edges where the heating element penetrates the welding stack [13]., Transversal edges are depicted in Figure 2.2-2: Temperature distribution at the welding interface due to the boundary conditions The problem of the current leakage becomes more prominent with the increase of the welding length. The current penetrates the laminates stack close to the laminate edges where HE enters into the welding stack because of two reasons: First, the possibilities for creation of alternative conductive path will appear as HE enters the welding stack. Second, due to the longitudinal temperature gradients when no measures are taken to cool the transversal edges the temperature of the laminate edges where HE enters into the welding stack is higher than in the middle of the welding interface, thus the regions of the welding interface close to the transversal edges will reach resin melting point faster, allowing a direct contact between the carbon fibres and the HE. Therefore current leakage will further increase longitudinal temperature gradient and only a small part around the transversal edges will be welded while the rest of the joint will be unwelded. Moreover the longer the heating element, the higher will be the required current voltage for the welding process. Consequently the risk of current leakage occurrence will be higher as well. A schematic view with the temperature distribution and current flow path in the case of current leakage is presented in the Figure 2.2-1:

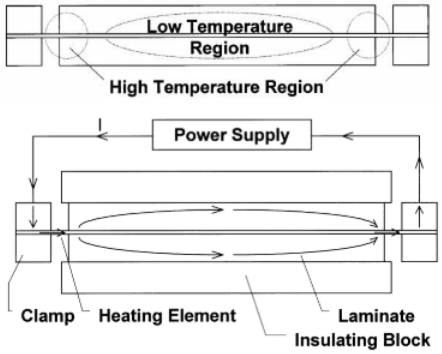

Figure 2.2-1: Current leakage phenomenon: Top-temperature distribution. Bottom-current flow paths [13]

In the literature there are several methods to avoid/diminish the current leakage. Dubé [18] claims that current leakage can be fully avoided by using a TiO_2-coated stainless steel heating element. Ageorges [13] achieved electrical insulation of the heating element by using a glass fabric prepreg with the cost of increasing the bond line thickness and of addition of a new foreign material at the welding interface beside steel. Thermabond® can also be a solution to prevent the current leakage. This method involves compression moulding of the semi-crystalline polymer based laminates as for example PEEK with a neat layer of amorphous resin as example PEI at the welding interface. During welding, the molecular diffusion will occur only between the PEI layers at the interface around the Tg point of the PEI resin at 210 °C, below the melting point of PEEK, therefore the carbon fibres embedded in the semi-crystalline material will not contact the heating element. However during the compression moulding some fibres from the semi-crystalline material may

migrate to the PEI resin contacting the heating element during the welding process, therefore electrical insulation cannot be fully achieved [21].

2.2.2 Effect of Boundary Condition on the Temperature Distribution

Boundary conditions are the main reason for the temperature gradients at the welding interface and influence the welding time. Well thermally insulated parts will reach the process temperature faster [6]. In the case of resistance welding the thermal insulation is ensured by sandwiching the parts to be joined between two thermal insulators.
In Figure 2.2-2 a typical temperature distribution at the welding interface is presented when transversal edges are not cooled or/and the electric contact clamps are far from the welding stack and do not have any influence on the temperature distribution on the welding interface.

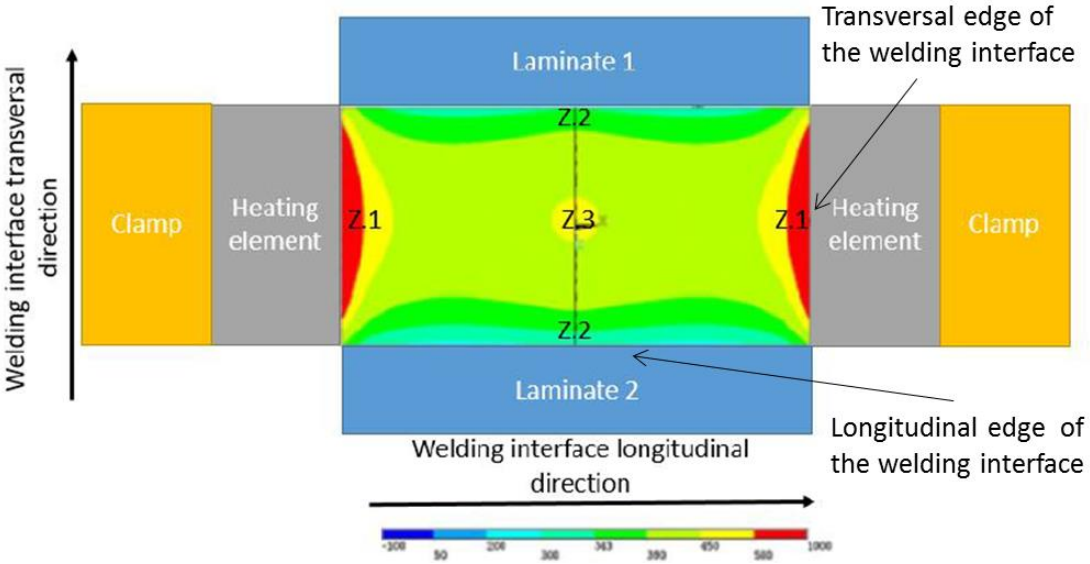

Figure 2.2-2: Temperature distribution at the welding interface due to the boundary conditions [5]

In the Figure 2.2-2 based on the temperature distribution three main zones can be distinguished. Zone1 is the region close to the edge where the heating element penetrates the welding stack. Zone2 is the area close to the edges parallel to the heating element and Zone3 is the middle of the welding interface. The temperature relation between these regions is the following:

$$T_{Zone1} > T_{Zone3} > T_{Zone2}$$

Longitudinal temperature gradient
The temperature gradient between Zone1 and Zone3 depicted in the Figure 2.2-2 was reported by numerous researchers [5, 17, 6, 15, 21, 13]. The temperature at the edges being higher than in the middle by about 100 °C [5] this extreme gradient can lead to the resin degradation at the edges or to fibre movement. The reason of the edge effect is the change of the heating element's boundary conditions. The heat generation per surface unit and the temperature distribution is uniform over the whole surface of the heating element in the case of conventional stainless steel mesh heating element if the boundary conditions are the same all over the heating element. When the heating element penetrates the welding stack its boundary conditions change from convection and radiation to conduction. The laminates to be joined are better heat conductors than air is, therefore the temperature of the heating element at the welding interface will be lower than the temperature of the heating element in the region exposed to air in the transient state.
The severity of the longitudinal edge effect is dependent on the power level. The heating element out of the welding stack reaches the steady state temperature within a few seconds depending on the power input, while the welding interface reaches the steady state temperature slower or does not reach it at all during the welding process. The higher the power level, the higher the steady state temperature of the exposed mesh will be and the faster the steady state will be achieved. Therefore

the temperature gradient will increase. Thus for the high power levels the temperature of the laminates edges where the heating element penetrates the welding stack could be above the degradation point while the middle of the joint will be under the melting temperature. Talbot [5] reported this situation for the following welding parameters and welding stack configuration: power level of 200 $\frac{kW}{m^2}$, the adherends consisted from 16 plies of unidirectional APC-2/AS4 composite laminates with total thickness of 2.16 mm, 101 mm long and 25.4 mm wide, the heating element used was M200 stainless steel mesh with the gap length of 0.09 mm and wire diameter of 0.04 mm, the welding interface was 25.4 mm long and 12.7 mm wide, the welding stack was thermally insulated using 37.5 mm thick "Wonderstone" alumina silicate, the distance between the clamps and the welding stack was 12.7 mm.

In the literature there are several methods to decrease the longitudinal edge effect. McKnight [3] suggested nitrogen gas air cooling of the edges as a strategy against the edge effect. Currently at CTC GmbH the transversal edges are cooled using the airflow. The advantage of this method is its flexibility, joints of different geometry can be welded. The issue is that the temperature at the edges is sensitive to the air flow speed and the airflow orientation, for this reason experiments repeatability is difficult to be achieved.

One of the methods against the longitudinal edge effect which gives a better control over the laminate transversal edges temperature is using the electric contact clamps as a heat sink by controlling the clamping distance (the distance between the clamps and the laminates to be welded) [5, 17, 12, 22]. Talbot [5] investigated the transversal edge temperature in function of the clamp position based on the transient heat transfer FEM model simulation results. A uniform longitudinal temperature distribution was achieved for a clamping distance of 0.65 mm for a power level of 160 $\frac{kW}{m^2}$., a welding time of 50 s and a process temperature of 380 °C. However this distance is dependent on other variables such as the joint geometry, power level, welding time, clamps material and size, insulator size and its thermal properties, the properties of the laminates to be joined and desired process temperature. For example Shi [12], for a different welding configuration found an optimum clamping distance of 9 mm for a welding process with the following parameters and welding stack configuration: the power input of $60\ \frac{kW}{m^2}$., welding time 104 s, process temperature 350 °C, adherends built from eight layers of GF/PEI 8-harness satin weave. The contact pressure between the heating element and the clamp has also an influence on the edge effect. A higher clamping pressure will lead to a better contact between the heating element and the clamps, thus facilitating the heat transfer between these two. A higher contact pressure will also decrease the contact electrical resistance, decreasing the generated heat [15].

Transversal temperature gradient

The temperature gradient between Zone2 and Zone3 pictured in Figure 2.2-2 was reported by [17, 5, 12], and in this report it will be referred as "transversal temperature gradient". Unlike the edge effect the temperature of the longitudinal edges is lower than the temperature in the middle of the welding interface. The reason of this gradient is that the longitudinal edges are cooled by the colder laminate adjacent to the welding interface, while in the middle of the joint the welding interface is heated by the heating element. However the transversal gradient is modest (30 °C [12], 50 °C [5]) compared to the longitudinal gradient caused by the edge effect.

2.3 FACTORS INFLUENCING LSS OF RESISTANCE WELDED JOINTS

The LSS is one of the common methods to evaluate the quality of resistance welded thermoplastic joints. The reference value is the strength of the compression moulded specimens [14, 21]. The LSS is dependent on the stress distribution along the overlap during the test. There are two stress types which have an impact on the LSS: the shear stress caused by the loading shear force and the peel stress caused by the secondary bending effect due to the eccentricity of the single lap shear joint. A typical shear stress and peel stress distribution can be seen in the Figure 2.3-1.

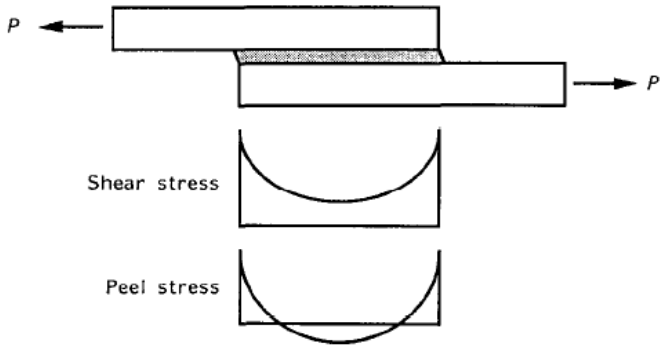

Figure 2.3-1: Typical shear and peel stress distribution of the adhesive in the SLS joint [23]

The shear stress peaks at the edges are caused by the higher strain of the adhesive at the edge compared to the strain in the middle of the joint. The shear stress peaks can be decreased by increasing the stiffness of the adherends and decreasing the stiffness of the adhesive. Both will contribute to a uniform loading of the adhesive parallel to the loading force. The peel stress is caused by the eccentricity of the joint, the joint loading forces are not aligned during the test, and consequently a bending moment will occur. The thicker the joint, the higher the bending moment, resultantly the higher the peel stress will be.

In the case of resistance welding, the LSS of the welded joints is also dependent on the resin type, the geometry of the heating element [9], the pressure and temperature distribution at the welding interface during welding [17], the bonding between the heating element and the resin [24], the bonding between fibres and resin [25]. Shi [25] showed that the fibre orientation of the adherend's layer adjacent to the welding interface influences joint lap shear strength. For that, Shi tested the LSS of the joints welded using four types of laminates: Type I $[(0°/90°)]_{4s}$ weft, Type I $[(0°/90°)]_{4s}$ yarn, Type II $[(90°/0°)]_{4s}$ weft, Type II $[(90°/0°)]_{4s}$ yarn. All four joints were welded under the same conditions using the same type of the heating element; M200 stainless steel mesh (0.04 mm wire diameter, 0.09 mm gap width).The adherends were built from 8 layers of 8HS woven GF/PEI. Type I laminate has the predominant orientation of the fibres in 0° direction, while Type II laminate has the predominant fibre orientation in 90° direction. The LSS test results are pictured below:

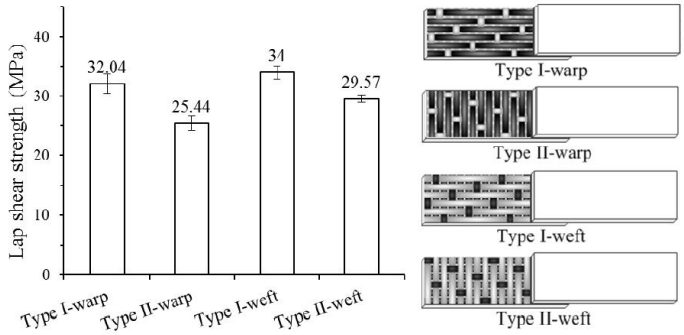

Figure 2.3-2: LSS test results of four different types of adherend layer orientation at the welding interface [25]

From Figure 2.3-2 it can be noticed that joints obtained by welding Type I laminates provided higher LSS than using Type II laminates. This can be explained by the fact than in the case of Type I the fibres are parallel to the load direction, therefore it aids the load transfer from the bonding interface to the rest of the adherend, consequently increasing LSS. Also it can be noticed that the weft layer at the welding interface provided higher LSS. This can be attributed to the waviness of the weft layer, which generates a more complex matrix/fibre debonding path. Shi [25] studied the effect of the fibre/matrix adhesion on the lap shear strength by comparing the LSS of the GF/PPS laminates with the same matrix and reinforcement but with different fibre sizing (Chromium Methacrylate and Aminosilane). The joints welded with Chromium Methacrylate sized fibres laminates provided higher LSS than joints welded with Aminosilane sized fibres laminates, 32 MPa, respectively 17.86 MPa. Chromium Methacrylate ensured a better adhesion between the matrix and the glass fibres. This

was proved by the SEM micrographs of the fracture surfaces where a better resin/ fibre adhesion was noticed in the case of Chromium Methacrylate.

2.3.1 Bonding Mechanism between Metal Mesh and Thermoplastic Resins

Fractographic analysis reported by numerous researchers showed weak adhesion between the stainless steel mesh and the thermoplastic resins for both amorphous and semi-crystalline thermoplastic resins, poor adhesion between PEEK/Steel [22, 9, 10, 2], poor adhesion between PEKK/Steel [2], poor adhesion between PPS/Steel [26, 27], poor adhesion between PEI/Steel [8]. Good adhesion between PEI/Steel was reported by Hou [16]. A possible explanation is that during the current flow through the metal mesh, generated ions could diffuse and react with the resin creating strong bonds. It is important to mention that the heating element was impregnated with PEI resin by compression moulding prior to welding, while in the previous mentioned sources neat resin films were added in the welding stack during the welding in order to fill the gaps of the mesh. Dube [18] reported a good adhesion of PEEK resin to TiO_2 coated mesh, however this did not increase the strength of the joint since a weak adhesion of TiO_2 to the metal mesh was reported. Recently Rohart [24] claimed that coating of the stainless steel mesh with silane sol-gel is increasing the adherence of the PPS matrix to the stainless steel mesh, consequently an increasing of the LSS up to 32% was reported. However for the un-treated metal meshes the main mechanism governing the bonding between the metal mesh and the thermoplastic resin is the mechanical interlocking [27] [28]. Mechanical interlocking between thermoplastic resin and stainless steel mesh is based on CTE difference. Resins have higher CTE than stainless steels, therefore during the cooling of the welding interface, the resin will contract more than metal. Consequently a compressive stress will act on the heating element surface [27].

2.3.2 Effect of Pressure and Temperature Distribution at the Welding Interface on Joints LSS

As it was discussed in section 2.2.2 during resistance welding there are two types of temperature gradients: along the length and along the width of the welding interface. The first one leads to a higher temperature at the edges perpendicular to the current flow than the temperature in the middle of the joint. This could lead to the resin degradation at the transversal edges. Longitudinal temperature gradient could also lead to the fibre movement or to the excessive resin squeeze out. Both effects are decreasing the thickness of the adherends at the overlap end, therefore the pressure applied by a hard plate will be carried by the overlap middle region mostly, where adherend thickness remained constant [22]. Low pressure might lead to a delamination if the pressure applied on the adherends is lower than the residual stresses. Or to the porosities if the compression pressure is lower than the minimum required pressure to impede void nucleation and growth [4]. Both, voids and delaminations caused by the uneven temperature distribution and consequently uneven pressure distribution may lead to a lower LSS value of the joint.
In the case of the transversal temperature gradient along the width of the welding interface, voids or delamination should not be expected since the temperature at the edge is lower than the temperature in the middle of the joint, therefore the resin squeeze-out should not occur thus sufficient pressure will be applied on the edges. Shi [17] in the case of welding GF/PEI, found porosities in the middle of the welding interface due to the residual moisture, this was attributed to the low pressure in that region. The pressure and temperature distribution are shown in the Figure 2.3-3.

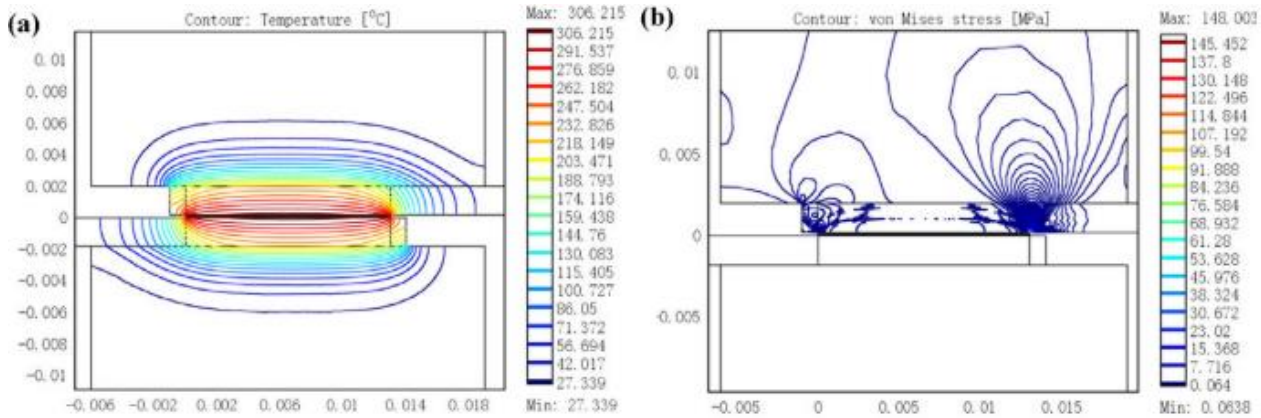

Figure 2.3-3: Temperature distribution through the width (a), Pressure distribution through the width (b) [17]

The following explanation of the voids presence in the middle of the joints was given. Young modulus is temperature dependent; it is increasing with the temperature decrease. At the longitudinal edges the temperature is lower relative to the temperature in the middle of the welding interface; therefore the material at the edges is stiffer. Consequently stiffer regions will carry more of the applied load, resulting in a higher compression stress in the stiff regions near to the longitudinal edges and lower compression in the less stiff regions in the middle of the welding interface, leading to void nucleation and growth in the middle of the joint.

2.3.3 Effect of the Mesh HE Geometry on Joints LSS

Dubé [9, 8] investigated the effect of the mesh geometry parameters on joints LSS by comparing the LSS results provided by the joints welded with five different meshes. The tested meshes are shown in the Table 2.3-1.

Table 2.3-1 Meshes investigated by Dubé [8]

Mesh type	Wire diameter [mm]	Open gap width [mm]	Open area fraction [%]	Linear wire density [wire/mm]
A	0.114	0.152	32.7	3.9
B	0.066	0.104	37.4	5.8
C/M200	0.041	0.089	46.9	7.7
D	0.036	0.043	29.6	12.5
E	0.025	0.038	36.4	14.3

The LSS result of the joints welded for three different resin/fibre system are provided in Figure 2.3-4.

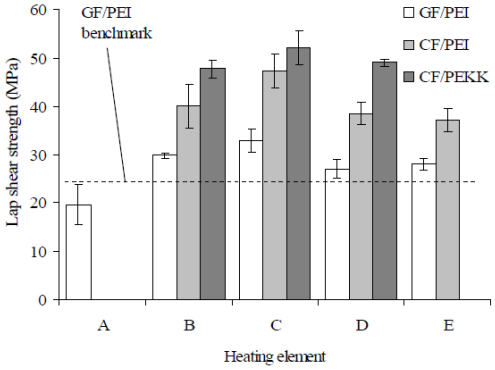

Figure 2.3-4: LSS in function of the mesh type and resin/fibre system obtained by Dubé [8]

From Figure 2.3-4 it can be seen that the best results are obtained using C type mesh. Dubé [8] attributed lower LSS results for the joints welded with the A and B meshes to the bigger wire

diameter and low value of the linear wire density. Mechanical interlocking is one of the mechanism on which bonding between thermoplastic resin and mesh relies. Therefore with the higher number of wires stronger interlocking should be expected.
The low LSS values of D and E meshes are attributed to the small mesh gap. The smaller the gap, the more difficult it will be for the resin to impregnate the mesh and to fuse with the resin from the opposite side of the mesh. This conclusion was supported by the fractographic analysis of the failure surface. In the case of the heating element D the joint failed at the interface between the adherend and the heating element, while in the case of the heating element C the damage to the adherends was noticed. The issue of the weak mesh impregnation in the case of the heating element D can be solved by impregnating the heating element prior to welding by using a hot press [16]. Based on the results described in this paragraph, Dubé [9] suggested to choose the heating element mesh based on the ratio between the open area ratio (OAR) and wire diameter. The higher the ratio, the higher LSS to be expected.
Shi [17] also investigated the effect of mesh geometry parameters on the joint's LSS in the case of adherends built from eight layers of 8HS GF/PPS semi-pregs. The meshes investigated by Shi are presented in the Table 2.3-2.

Table 2.3-2: Meshes investigated by Shi [17]

Mesh type	Wire diameter [mm]	Open gap width [mm]	Open area fraction [%]	Linear wire density [wire/mm]
M200/C	0.04	0.089	48	7.7
M24	0.2	0.858	66	0.9
M26	0.2	0.777	63	1
M45	0.2	0.364	42	1.7
M12	0.5	1.617	58	0.5
M8	0.7	2.475	61	0.3

The lap shear results obtained are presented in the picture below:

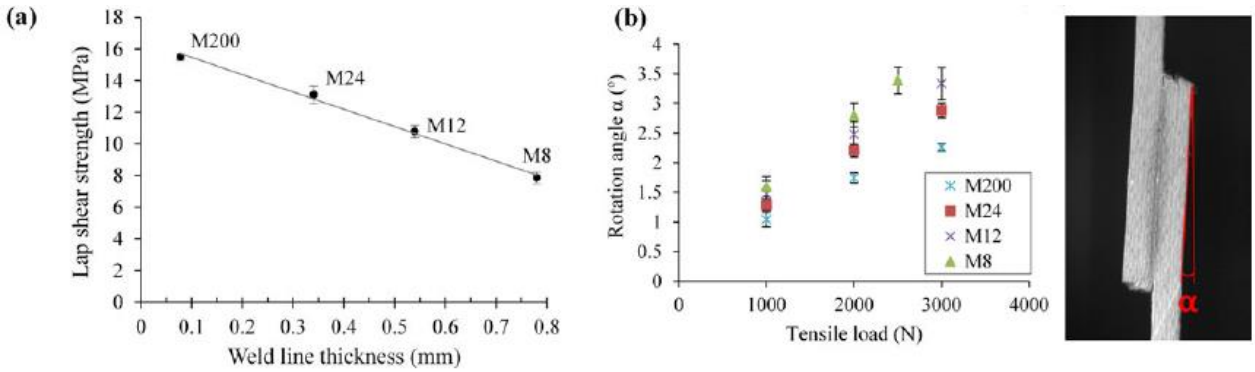

Figure 2.3-5: LSS in function of mesh thickness (a) rotation angle of the joint in function of the mesh thickness (b) obtained by Shi [17]

As Dubé [9, 8] Shi [17] obtained also the highest LSS values for the joints welded using M200 mesh. Shi attributed higher performance of M200 mesh to its smaller diameter providing a smaller bond line thickness compared to other tested meshes. The reduction of the bond line thickness caused the decrease of the secondary bending Figure 2.3-5(b) leading to decrease of the peel stresses, consequently increasing the LSS. To further investigate the effect of the bond line thickness on the LSS by excluding the effect of the OAR, Shi compared the LSS of the joints welded with the M200 mesh but with different number of the neat PPS layers at the welding interface Figure 2.3-6(a) (PPS layer thickness 0.09 mm). To study the effect of the open area fraction and excluding the mesh thickness factor, Shi compared the LSS of the joints welded with M24, M26, M45 meshes, which have the same diameter but different open area fraction consequently different linear wire density Figure 2.3-6 (b).

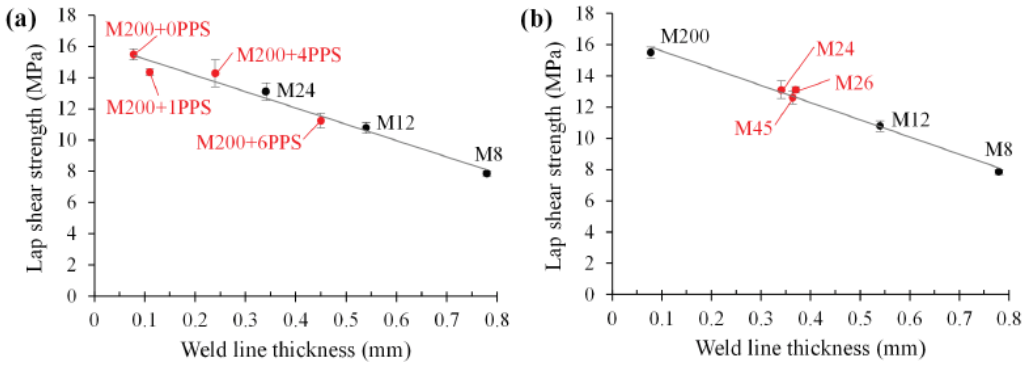

Figure 2.3-6 LSS comparison between the joints welded with M200 mesh but with different numbers of neat resin at the interface (a), LSS comparison between the joint welded with the meshes having the same diameter but different open area fraction (b). [17]

From Figure 2.3-6(a) it can be noticed that the LSS is decreasing with the increase of PPS layers number. Based on the results presented in the Figure 2.3-6(b), Shi [17] concluded that LSS depends on the heating element thickness only and is independent of the open area ratio and of the linear wire density (LWD). This contradicts Dubé's conclusion and results that LSS is also dependent on the OAR. Therefore a more in depth research is required to understand the link between LSS and mesh geometric parameters such as heating element thickness, LWD and OAR.

Ageorges [14] investigated the effect of the bond line thickness and the layer orientation at the bonding interface on the joint LSS. By testing the LSS of the compressed moulded laminates [CF/PEI$_{10}$] with different layer orientation at the bonding interface. The configuration of the tested compressed moulded specimens are presented in the Table 2.3-3.

Table 2.3-3: LSS results of the compressed moulded specimens with different stacking sequences [14]

Specimen	Stacking sequence of each adherend	Stacking sequence between adherends	Resultant stacking sequence	LSS [MPa]
1	[CF/PEI$_{10}$]	none	[CF/PEI$_{20}$]	35.2±1.8
2	[CF/PEI$_{10}$]	[PEI, CF/PEI(0°),PEI]	[CF/PEI$_{10}$,PEI, CF/PEI(0°),PEI, CF/PEI$_{10}$]	28.5±1.6
3	[CF/PEI$_{10}$]	[PEI, CF/PEI(90°),PEI]	[CF/PEI$_{10}$,PEI, CF/PEI(90°),PEI, CF/PEI$_{10}$]	28.3±1.8
4	[CF/PEI$_{10}$]	[PEI, CF/PEI(0°,90°)F,PEI]	[CF/PEI$_{10}$,PEI, CF/PEI(0°,90°)F, PEI, CF/PEI$_{10}$]	33.1±0.1

*Where **CF/PEI(0°,90°)F** denotes a fabric prepreg*

The highest LSS value was obtained for the specimens moulded without any additional layers at the joining interface, enforcing Shi's [17] conclusion that the bond line thickness has a big impact on the LSS of the welded joint. The higher LSS in the case of the specimen 4 compared to the specimen 2 and 3 was attributed to the failure mechanism involving fibre failure of the fabric layer in the case of the specimen 4 compared to the resin failure in the case of specimens 2 and 3 [14]. The resulted fibre breakage failure mechanism in the case of the specimen 4 compared with the resin failure for the specimen 2 and 3 could be attributed to the stronger interlocking in the case of the fabric layer compared to the UD layer due to the wavy surface of the fabric layer.

2.4 RESEARCH PROPOSAL

2.4.1 Identified Gaps in the Literature

From the literature study it was identified that important factors influencing the strength of the joint are: the temperature distribution at the welding interface, bonding between resin and fibres, layer orientation at the welding interface, bonding between HE and resin which partially relies on HE geometry. The uniform temperature distribution can be achieved by tailoring the generated heat by the heating element or by adjusting the boundary conditions of the welding interface.
A good bonding between the matrix and the heating element is important in order to provide high strength joints. As it was found in the literature the mechanical interlocking is the main mechanism on which the bonding between stainless steel mesh heating element and resin relies. The evidence is given by the fractographic analysis of the failed joints which showed that there is no resin attached to stainless steel mesh. Stainless steel mesh parameters such as the mesh thickness, the open area ratio, the linear wire density have an impact on the LSS of the joint. Shi [17] and Dube [9] studied individually the effects of these parameters on joints LSS. However the conclusions of their studies partially refute each other. On one side Shi concludes that the thickness is the most important factor since the thickness of the HE is influencing the thickness of the whole welding stack and has an effect on the secondary bending moment, increasing peel stresses. On the opposite side Dubé concludes that the open area ratio and the wire diameter are the most important factors influencing joint LSS. Therefore it is still unclear how the geometrical parameters of the mesh are influencing the LSS. The contradiction found in the literature might come from the fact that both researchers did not evaluate each parameter separately since this is impossible, because some of them are coupled. For example the heating element thickness is dependent on the wire diameter since the thickness of the mesh is equal to two diameters. The linear wire density is dependent on the wire diameter as well. A way to study the effect of each parameter on LSS is to uncouple them, this can be done by using a laser cut plate heating element. Thus the open area ratio, the heating element thickness and the linear wire density can be changed without affecting each other. In the section 2.4.2 the concept of the laser cut plate is presented.

2.4.2 Laser cut HE Idea Presentation

During this research two concepts of laser cut plate HE will be used: Concept 1 heating element will be oriented towards diminishing the longitudinal temperature gradient. Concept 2 heating element will be oriented to diminish both gradients, along the width and along the length of the joint.

2.4.2.1 Concept 1 HE Design Decreasing the Longitudinal Temperature Gradient

The Concept 1 heating element is presented in Figure 2.4-1:

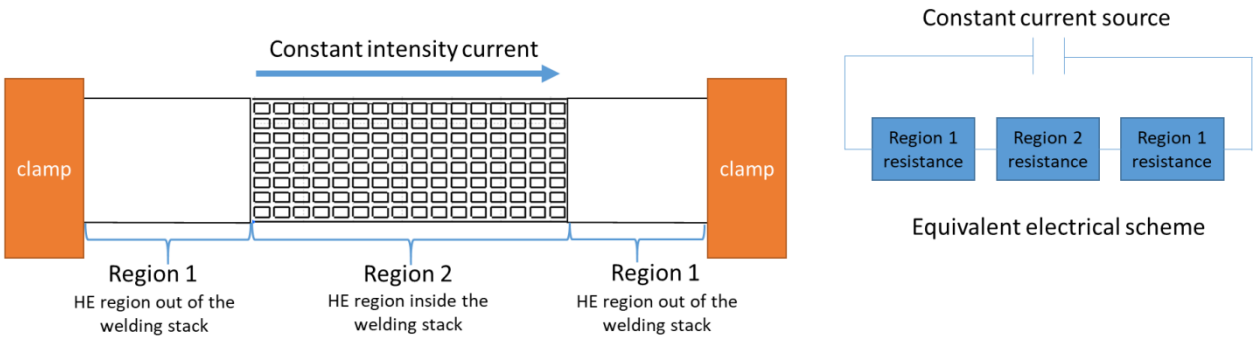

Figure 2.4-1: Concept: Laser cut plate design concept to decrease the longitudinal temperature gradient

From the Figure 2.4-1 it can be seen that the cuts into the plate are made only in the region sandwiched between the adherends (Region 2).
In Region 2 the electrical resistance per unit length will be higher than in Region 1 since the cross sectional area is smaller. The electrical resistances of Region 1 and Region 2 are connected in series therefore the intensity of electric current flowing in those regions will be equal. Thus according to the power formula $P = I^2 \times R$ the power per surface unit generated by Region 1 will be lower than the Power generated by Region 2. Consequently, because the generated heat per surface unit by the exposed region of the heating element will be lower, the temperature of the exposed region will decrease, decreasing the longitudinal temperature gradient. Because as it was identified in section 2.2.2 the overheating of the exposed region of the heating element was found the main reason of the longitudinal temperature gradient.

2.4.2.2 Concept 2 HE Design Decreasing the Longitudinal and Transversal Temperature Gradients

The concept of the heating element diminishing both gradients is presented in Figure 2.4-2.

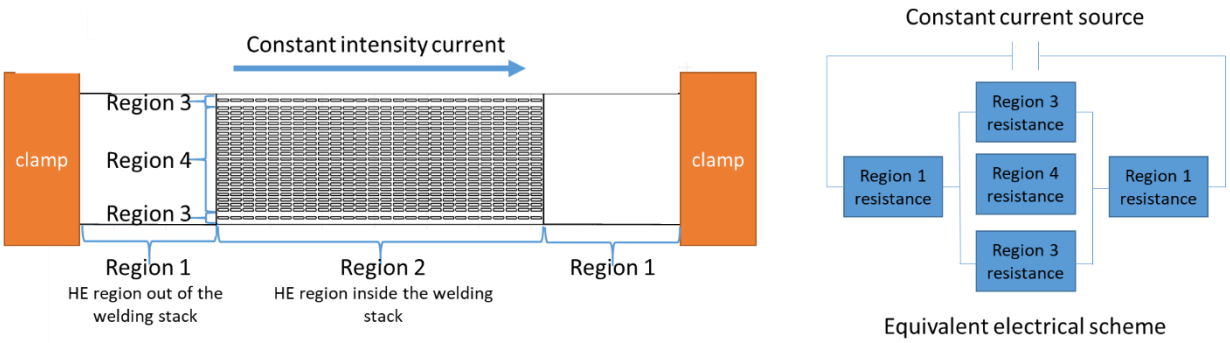

Figure 2.4-2:Concept_2: Laser cut plate design concept to decrease the longitudinal and transversal temperature gradient.

Compared to Concept 1 (Figure 2.4-1), the concept presented in Figure 2.4-2 does not have a constant cross section along the HE width, cross sectional area close to the longitudinal edges (Region 3) is bigger than in the middle of the HE (Region 4). Consequently electrical resistance of Region 3 is lower than Region 4 resistance. Thus current intensity per width unit in Region 3 will be higher leading to a higher heat generation rate per unit surface in Region 3 than in Region 4, leading to the transversal edges temperature increase diminishing the temperature gradient along the width of the welding interface.

2.4.3 Research Objective and Research Questions

The objective of the study is: *"Increasing the temperature uniformity along the welding interface, with the aim to increase the overall value of the lap shear strength by tailoring the power generation rate along the heating element*".

From the research objective viewed from the perspective of the laser cut plate heating element and from the literature study next research question can be drawn:

1. **What are welding parameters initial (initial power per surface and welding time) to achieve uniform longitudinal temperature distribution for a joint with predefined geometries and boundary conditions using Concept 1 heating element?**

2. **What are welding parameters initial (initial power per surface and welding time) to achieve uniform temperature distribution for a joint with predefined geometries and boundary conditions using Concept 2 heating element?**

The first two questions will result into the input data for the laser plate design with the purpose to generate uniform temperature distribution at the welding interface.

3. **What is the relation between the heating element linear wire density and the lap shear strength of a welded joint?**

Dube [9, 8] and Shi [17] investigated the effect of the mesh geometry on the joint LSS. The beneficial effect of the lower bond line thickness is irrefutable. However the effect of LWD on LSS is unclear. The interlocking mechanism depends of the open area ratio and the linear wire density. In the case of metal meshes for a constant thickness it is impossible to keep one of these parameters constant, since the change of the linear wire density will also change the open area ratio. In the case of the laser cut stainless steel plate heating element the thickness and the open area fraction can be kept constant while varying only the linear density. Thus the LWD effect on LSS can be studied while eliminating other factors. It is expected that higher linear density will increase the lap shear strength of the joint.

4. **What is the relation between the heating element open area ratio and the lap shear strength of a welded joint?**

Shi [17] concluded that LSS of the welded joints is independent of the stainless steel mesh OAR. This conclusion seems to be debatable according to the following reasoning: The bonding between resin and stainless steel is weak; there is no chemical reaction between these two. Consequently it is desired to have direct interaction between the resin of the laminates to be joined, rather than to have stainless steel material between them as a coupling material. Higher OAR means that the contact surface interface between resin and steel will be smaller. This should increase the lap shear strength of the welded joint.

5. **What is the uniform temperature distribution effect on lap shear strength?**

The uniform temperature distribution on the welding interface should lead to a stronger joint because of two reasons: First, uniform temperature distribution is an important factor to ensure uniform pressure distribution over the overlap which has a positive effect on LSS. Second, welding temperature in the case of Concept_2 will be lower compared to Concept_1 and the conventional M200 mesh heating element, where due to the transversal gradient resin in the middle of the overlap and at the transversal edges will be kept above resin melting temperature until longitudinal edges reach resin melting temperature as well. Long exposure of the transversal edges above resin melting point will lead to the fibre movement phenomenon, which is a cause of void formation within the adherends.

The planned work flow in order to answer the research questions is presented in the picture below.

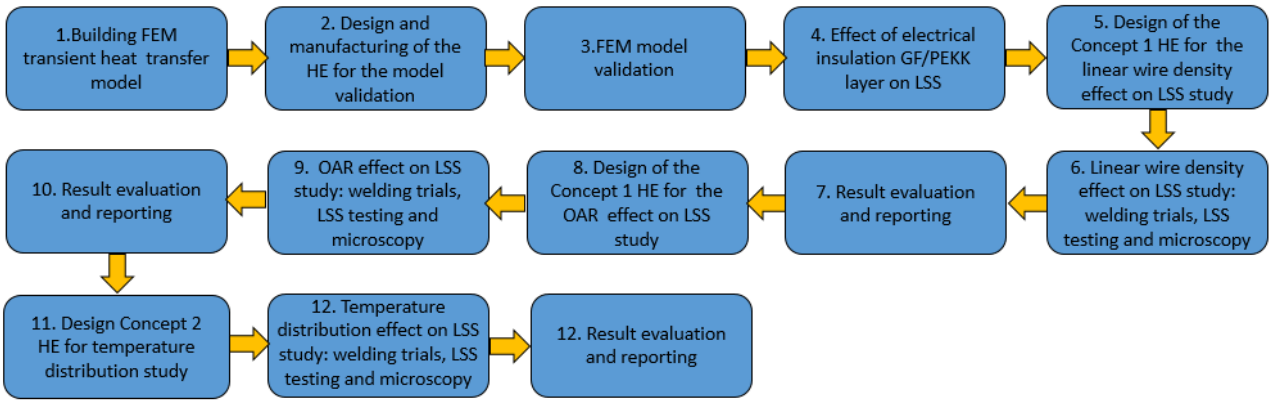

Figure 2.4-3 Planned Workflow

3. EXPERIMENTAL SET-UP MATERIALS AND METHODS

3.1 MATERIALS AND EQUIPMENT

Resistance welding machine

The welding machine used for the welding trials was provided by CTC GmbH. The machine max output is an electrical current with 110 A intensity and 66 V voltage and it is able to deliver constant current intensity only, therefore the current voltage will be adjusted by the machine automatically during the welding process according to the Ohm's law in function of the HE resistance. That means that during the welding process the power generated at the welding interface will not be constant because the power is the product between current voltage and intensity. In the case of steel the resistivity is increasing with the temperature increase. Thus increasing the current voltage, and consequently power generated by the HE will increase as well during the welding process. Because of that, through this thesis the power per surface generated by the HE at RT will be used as a welding parameter, called initial power per surface (IPS).

In order to apply pressure on the welding interface the machine is equipped with four pneumatic cylinders which can be activated independently of each other and can provide maximum force of 1960 N. The machine is equipped with J-type thermocouples (TC) and can record TC measured temperature, delivered current and voltage with 1 s time interval.

The electrical contact is ensured by copper clamps. The clamp consists from two copper plates and the HE is clamped between them. The clamping pressure is provided by a bolt-nut mechanism, thus the exact clamping pressure is unknown.

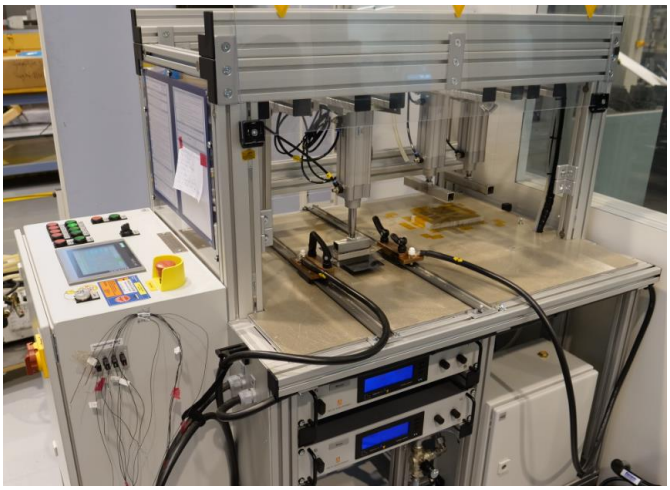

Figure 3.1-1: Welding machine

Welding assembly materials

The welding assembly consists from the laminates to be welded, the thermal insulators and an impregnated heating element sandwiched between two layers of glass fabric and two layers of neat PEKK. The overlap length is 88 mm and the overlap width is 25.4 mm

The specimens to be welded were cut to the size of 101.6 mm by 88 mm from a 450 mm by 300 mm QIL plate built from 12 layers 0.184 mm thick CF/PEKK **Tenax®-E TPUD PEKK-HTS45** prepreg supplied by **Toho TENAX.** The prepreg layup was prepared at CTC GmbH with the following stacking sequence $[0°/45°/135°/90°/45°/135°/135°/45°/90°/135°/45°/0°]$, 0° direction being parallel to the 101.6 mm edge of the specimens to be welded and it is parallel to the loading force during LSS test. Before welding, adherends were dried in an oven for 12 h at 100 °C to ensure that any trapped moisture will be eliminated. Due to the flaws during the laminate consolidation process, one face of the resulted laminates was curved. Because of that cut specimens did not have constant thickness along the overlap; it was varying from 2.05 mm to 2.22 mm.

The thermal insulation blocks consist from two 25.4 mm by 88 mm stacked plates: 15 mm and 4 mm thick forming together a 19 mm thick insulator block. This thickness ensured a full thermal insulation of the adherends from the pressure applicator piston head during the welding process. The 15 mm

plates are positioned on top/ bottom of the laminates to be welded. The thermal insulation plates consist from KTherm® AS600M which is manufactured from Mica paper embedded in silicone resin and were provided by **AGK-Hochleistungswerkstoffe GmbH.**

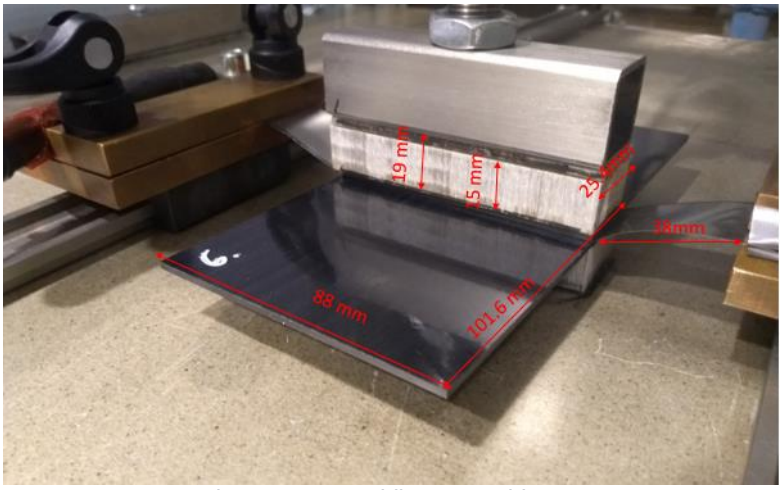

Figure 3.1-2: Welding assembly

The Heating elements used for this study were impregnated between two layers of GF/PEKK fabric and two 0.05 mm thick neat PEKK layers. The PEKK layers are required to fill the HE gaps with resin and the GF/PEKK fabric is required for the HE electrical insulation from the conductive CF contained by the laminates to be welded. For this research three types of glass fabric were studied: **Barrday TF0300-48-G108 PW-50-38.00-2S**, **Toray GK 1080 127 60 120 Cetex TC1322**, **Porcher E-glass/PEKK 4H Satin 157 g/sqm**. The glass fabrics were positioned with the warp bundles perpendicular to the loading force during LSS tests. As it was found in the literature this makes the failure path between glass fabric and adjacent layers more arduous. Also two types of HE were used during this research. The first one is the baseline HE M200 mesh; supplied by **The Mesh Company** manufactured from AISI 304 stainless steel wires. The M200 mesh wire diameter is 0.04 mm and the gap between 2 wires is 0.09 mm. The second HE is the novel heating element and was created by laser cutting of AISI 304 stainless steel plates 0.05 mm and 0.1 mm thick. The stainless steel sheets were provided by **Goodfellow Company**. And the laser cutting operation was performed by **TEPROSA GmbH.**

FEM modelling

The FEM software used to simulate the resistance welding process in this research is Abaqus software version 2016-4.

Microscopy

The microscopy work done through this research was performed using VHX-6000 Digital Microscope.

Mechanical testing

The welded joints have an overlap length of 88 mm and overlap width of 25.4 mm. The specimens with 25.4 mm overlap length were cut from the welded joints according to the ASTM-D5868-01 lap shear testing standard. The mechanical testing was performed using Zwick Z250 testing machine with the loading rate of 2 mm/min. Welded joint geometry and the positions from where the specimens for the mechanical testing were cut are shown in the Figure 3.1-3.

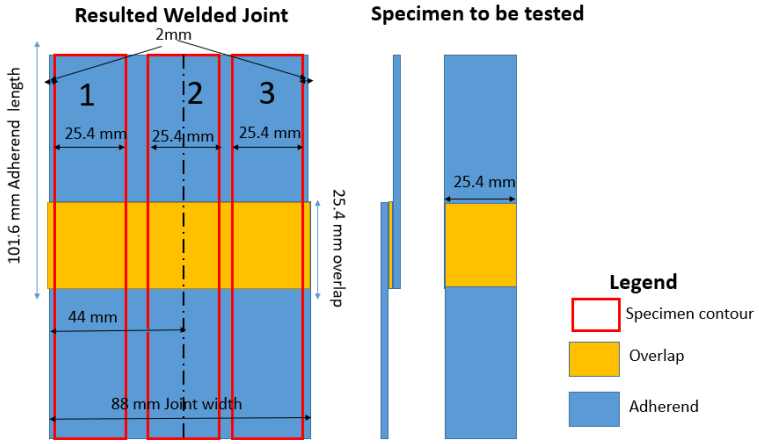

Figure 3.1-3 Resulted welded joint and position from where specimens to be tested were cut (left) Specimen to be tested (right)

3.2 METHODS

3.2.1 Laser Cut HE Design Approach

HE for linear wire density study and FEM validation (Concept_1_0)

Concept_1_0 HE was manufactured to assess the manufacturing process of the laser cut plate heating elements and design limitations imposed by the manufacturing process. The obtained heating elements were used for the FEM model validation and for the linear wire density (LWD) effect on joint lap shear strength study.

The required HE width is given by the joint overlap width. And its required length is given by the overlap length plus the distance between the electric contact clamps and the welding stack. The minimum distance between electric clamps and the overlap should be sufficiently high to ensure that the electrical clamps do not affect the temperature distribution in the welding stack. From the literature it was found that the temperature in the welding stack was not affected by the clamps temperature for distance between the clamps and the welding stack higher than 20 mm. For this research the length of the HE out of the welding stack per side will be 45 mm (38 mm distance between the clamps and the welding stack + 7 mm HE length clamped between the electrical contact clamps).

Another input design parameter of Concept _1_0 HE design is the temperature of the HE region out of the welding stack. It is desired that steady state temperature of the HE out of the welding stack to not be higher than the welding temperature. This is a mandatory requirement to achieve longitudinal temperature distribution uniformity. From the material supplier data sheet the recommended consolidation temperature is 375±10 °C, therefore the desired steady state temperature of the HE out of the welding stack will be set to 383 °C. According to equation (3.2-1) the power per surface generated by the HE in the region out of the welding stack at the moment the HE plate reaches 383 °C will be 22.75 $\frac{kW}{m^2}$.

$$PS_{ows}(T) = 2[h \cdot (T - RT) + \varepsilon \cdot \sigma \cdot (T^4 - RT^4)] \quad (3.2\text{-}1)$$

($\boldsymbol{T}$)*denotes that physical quantity is temperature dependent.

Where: $\boldsymbol{PS_{ows}}$ is power per surface generated by the HE at the area out of the welding stack, $\boldsymbol{T}$ is HE temperature, $\boldsymbol{RT}$ is room temperature (22 °C), $\boldsymbol{h}$ is free convection coefficient $5\ \frac{W}{m^2K}$, $\boldsymbol{\sigma}$ Boltzmann constant, $\boldsymbol{\varepsilon}$ is the emissivity coefficient (0.95).

Furthermore the necessary current input to obtain the power level can be calculated as follows.

$$I = \sqrt{\frac{PS_{ows}(383\ °C) \cdot th \cdot Width^2}{res_{steel}(383\ °C)}} \tag{3.2-2}$$

Where: $\boldsymbol{I}$ is electrical current intensity, $\boldsymbol{PS_{ows}(383\ °C)}$ is power per surface generated by the HE at the region out of the welding stack at T=383 °C, $\boldsymbol{res_{steel}(383\ °C)}$ steel resistivity at $383\ °C$.

By solving the equation (3.2-2) for 0.1 mm and for 0.05 mm thick stainless steel plates will be obtained that the necessary current input to bring the surface of the plate HE element out of the welding stack to T=383 °C is 39 A respectively 27.6 A. The resistivity of steel is decreasing with the temperature decrease that means that the power generated by the HE at RT will be lower. The power per surface (PS) in the region out of welding stack at RT which further in this report will be called initial power per surface (IPS) can be calculated with formula (3.2-3).

$$IPS_{ows} = PS_{ows}(22\ °C) = \frac{I^2 \cdot res_{steel}(22\ °C)}{th \cdot Width^2} = 16.83\ \frac{kW}{m^2} \tag{3.2-3}$$

The last design input parameter for the Concept_1HE design is OAR of the HE region inside the welding stack. Since M200 mesh will be used as a baseline HE, for the first trials it is desired to have a plate HE with square shaped gaps and with the OAR identic to the M200 mesh.

As it was mentioned Concept_1 HE will be used for the FEM model validation. The temperature distribution is heavily affected by the material properties. Therefore it is desired to perform the FEM model validation at low power per surface level first. Because for the low power levels the welding time is longer and more material will be heated, consequently the temperature at the welding interface will be more sensitive to the material thermal properties. From the Literature study it was found that a low power level is considered to be between $50 - 70\ \frac{kW}{m^2}$. For the FEM model validation an initial power per surface level of $51\ \frac{kW}{m^2}$ will be used.
With the current intensity fixed, the only way to tailor the HE power generation at the welding interface is by changing its resistance. IPS is varying linearly with the HE resistance and resistance is linearly dependent on the conductor transversal area. Because the plate thickness is constant, the only way to increase plate resistance is by decreasing its electrical conductive path width (width sum of all longitudinal wires). The required path in the HE region inside the welding stack which will provide necessary resistance resulting in a desired IPS in the tailored region can be calculated with (3.2-4) formula:

$$PW_{iws} = Width \cdot \frac{IPS_{ows}}{IPS_{iws}} \tag{3.2-4}$$

Where: $\boldsymbol{PW_{iws}}$ is the width sum of all the longitudinal wires of the HE region inside the welding stack, $\boldsymbol{IPS_{iws}}$ the initial power per surface generated by the HE inside the welding stack, $\boldsymbol{IPS_{ows}}$ is the initial power per surface generated by the HE outside the welding stack.
Solving (3.2-4) equation for a desired IPS at the HE region inside the welding stack of $51\ \frac{kW}{m^2}$ will give a path width equal to 8.4 mm.
One of the research objectives is to find the effect of the linear wire density on LSS. Thus three types of HE Concept_1 for 0.1 mm and for 0.05 mm thick plates were designed. The designed HE have the same OAR close to M200 mesh (0.45) and the same electrical conductive path width in the region inside the welding stack, but have different LWD. The properties of the designed HE are summarised in Table 3.2-1.

Table 3.2-1 Concept_1_0 plate HE

Series	Type	Thickness [mm]	Longitudinal wires Number	Gap length [mm]	Gap width [mm]	Longitudinal wire width [mm]	Transversal wire width [mm]	LWD	OAR
Concept_1_0	A005	0.05	42	0.408	0.408	0.2	0.2	1.65	0.45
	B005	0.05	35	0.489	0.489	0.24	0.24	1.37	0.45
	C005	0.05	28	0.61	0.61	0.3	0.3	1.1	0.45
	A01	0.1	42	0.408	0.408	0.2	0.2	1.65	0.45
	B01	0.1	35	0.489	0.489	0.24	0.24	1.37	0.45
	C01	0.1	28	0.61	0.61	0.3	0.3	1.1	0.45

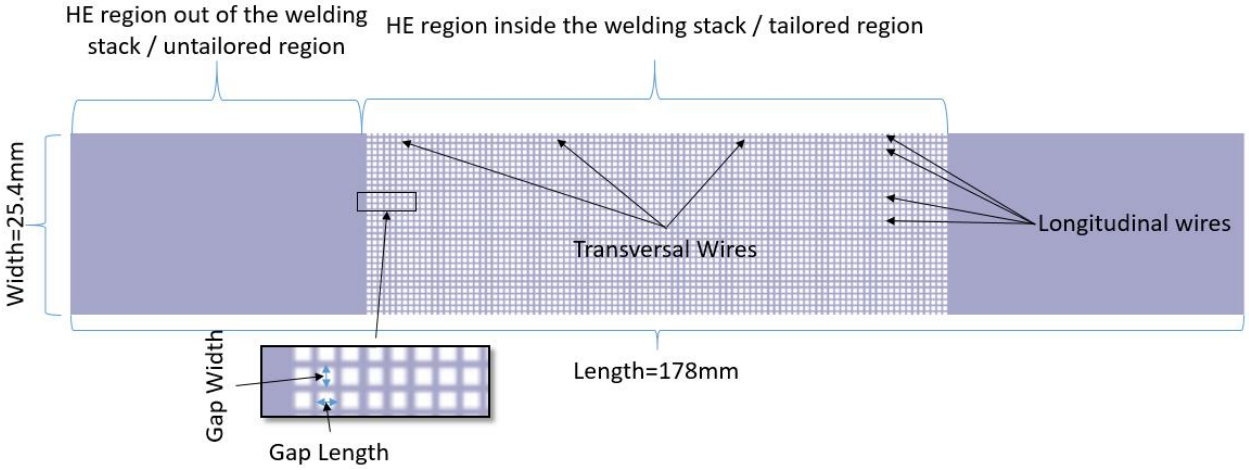

Figure 3.2-1: Concept_1_0 Type C005 HE sketch

HE for OAR study Concept_1_1.

From the welding trials using Concept_1_0 HE uniform longitudinal temperature distribution was achieved. However the welding time was quite long: 140 s, because of low IPS in the tailored region of $51\ \frac{kW}{m^2}$. In order to decrease the welding time, IPS value in the tailored region of the HE should be increased. This can be done either by increasing current input either by decreasing electrical resistance. Increasing input current is not an option, because it will increase the steady state temperature of the HE region out of the welding stack above 383 °C, which is not desired because an increase of the HE temperature out of the welding stack will lead to longitudinal temperature gradients. Thus IPS at the welding interface was changed by increasing electrical resistance of the HE inside the welding stack, keeping current intensity input 39 A for the 0.1 mm thick plates. Electrical resistance was increased by decreasing the total conductive longitudinal path width from 8.4 mm to 6 mm. This resulted in an IPS at the welding interface of 71.4 $\frac{kW}{m^2}$ according to equation (3.2-4), consequently to a decreased welding time from 140 s to 75 s.
The characteristics of the designed Concept_1_1 HE is presented in the Table 3.2-2.

Table 3.2-2 Concept_1_1 plate HE characteristics

Series	Type	Thickness [mm]	Longitudinal wires Number	Gap length [mm]	Gap width [mm]	Longitudinal wire width [mm]	Transversal wire width [mm]	OAR
Concept_1_1	C1	0.1	20	0.55	0.98	0.3	0.3	0.5
	C2	0.1	20	1.02	0.98	0.3	0.3	0.6
	C3	0.1	20	2.55	0.98	0.3	0.3	0.7

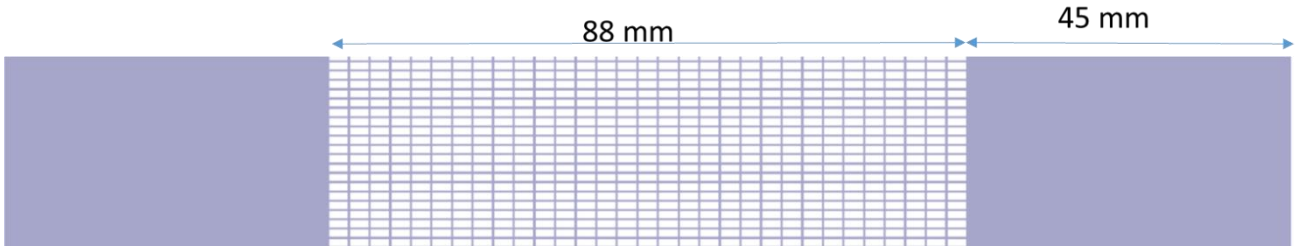

Figure 3.2-2: Concept_1_1 Type C3 HE sketch

Concept_2 HE elements for uniform temperature distribution study.

With Concept_1_0, the longitudinal temperature gradient was eliminated, Concept_1_1 decreased the welding time from 140 s to 75 s. Concept_2 design was focused towards eliminating both temperature gradients; longitudinal and transversal. To eliminate the transversal temperature gradient, the temperature of the longitudinal edges of the welding interface should be increased. This can be achieved by having a higher IPS close to the longitudinal edges than in the middle of the welding interface. Therefore as it was presented in the Figure 3.2-3 the HE region at the welding interface was split in two regions: Region3 close to the longitudinal edges where IPS should be higher and Region4 in the middle of the welding interface.

Ideally the width of Region3 should be as small as possible; because the generated heat by it should overcome the energy loses at the longitudinal edges of the welding interface due to the boundary conditions. But because of the HE manufacturing process tolerances and because of the positioning tolerances of the HE inside the welding stack, it was decided the width of Region3 to be 2 mm. The IPS in Region4 was decided to be 71.4 $\frac{kW}{m^2}$ because in the case of Concept_1_1 HE it led to an acceptable welding time of 75 s. The IPS in Region3 was found using an iterative process with the help of the electrical coupled heat transient FEM model by increasing IPS in Region3 until the temperature transversal gradient was eliminated; this request was fulfilled by an IPS equal to 110.4 $\frac{kW}{m^2}$. In order to keep the temperature of the un-tailored region at 383 °C, the current intensity was fixed as in the case of Concept_1_1 to 39 A.

The IPS in Region3 and Region4 is dependent on the electrical resistance of these regions. The required resistance in order to achieve the desired IPS was calculated by using Kirchhoff's Rules and solving (3.2-5) equation system given by the electrical circuit presented in Figure 2.4-2.

$$\begin{cases} I = I_4 + 2 \cdot I_3 \\ I\dfrac{R_4 \cdot R_3}{2 \cdot R_4 + R_3} = I_4 \mathrm{R}_4 \\ I_4^2 \cdot R_4 = Width_4 \cdot Length_{iws} \cdot IPS_4 \\ I_3^2 \cdot R_3 = Width_3 \cdot Length_{iws} \cdot IPS_3 \end{cases} \tag{3.2-5}$$

Where: $\boldsymbol{R_4}$ and $\boldsymbol{R_3}$ is the required resistance in Region 4 and Region3, $\boldsymbol{I}$, $\boldsymbol{I_3}$ and $\boldsymbol{I_4}$ are the applied current intensity and current intensity in Region 3 and Region4, $\boldsymbol{Width_3}$ and $\boldsymbol{Width_4}$ is the Regions width, $\boldsymbol{IPS_3}$ and $\boldsymbol{IPS_4}$ are the desired IPS in Region 3 and Region 4, $\boldsymbol{Length_{iws}}$ is HE length inside the welding stack.

Solving the upper equation system result in a resistance of the Region3 and Region4 equal to 1.034 Ω. respectively 0.145 Ω.

Furthermore, by using (3.2-6) formula the total width of the longitudinal paths for Region3 and Region4, in order to achieve the desired resistance from the previous step was calculated.

$$PW = \frac{res_{steel} \cdot Length_{iws}}{th \cdot R} \tag{3.2-6}$$

Solving the upper equation for $\boldsymbol{R=R_4}$ and $\boldsymbol{R=R_3}$ will result in a path width of 4.34 mm in Region4 and 0.608 mm in Region3.

The characteristics of a HE fulfilling these requirements are presented in Table 3.2-3.

Table 3.2-3 Concept_2 plate HE characteristics

Region	Longitudinal paths number	Gap length [mm]	Gap width [mm]	Longitudinal path width [mm]	Transversal path width [mm]	OAR
Region 3	18	1.28	0.982	0.24	0.24	0.65
Region 4	3	2.55	0.456	0.205	0.205	0.64

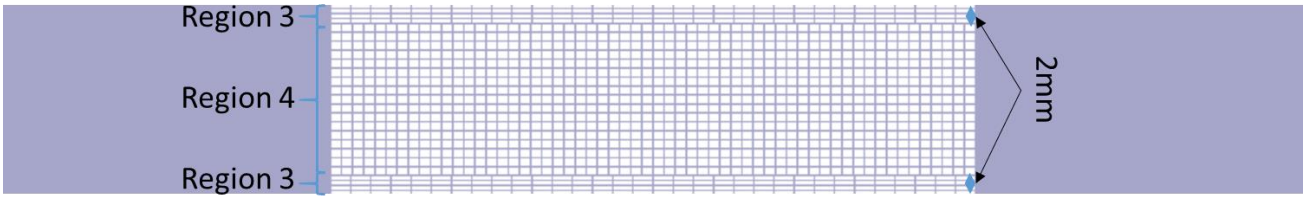

Figure 3.2-3:Concept_2 HE sketch

3.2.2 FEM Model Building

The Development of Concept 1 and especially of Concept 2 heating elements required multiple iterations because the welding set up and material properties have an influence on the temperature at the welding interface, respectively on the required heating time and IPS at the welding interface necessary to melt the resin. Manufacturing of the laser cut plate novel heating element is more expensive than the conventional stainless steel mesh heating element and it is time consuming since the laser cut heating elements are manufactured by a partner company outside of CTC GmbH. Therefore it was decided to use a FEM welding simulation to find the welding parameters and to design the laser cut plate heating elements rather than finding them from expensive experimental trials.

Heat is transferred through three mechanisms: conduction, convection and radiation. The heat transfer equation on which the three dimensional model is based is the following

$$\left(k_{xx}\frac{\partial^2 T}{\partial x^2}+k_{yy}\frac{\partial^2 T}{\partial y^2}k_{zz}\frac{\partial^2 T}{\partial z^2}\right)+\dot{q}=\rho\cdot c_p\frac{\partial T}{\partial t} \tag{3.2-7}$$

Where: $\boldsymbol{k}$ is the thermal conductivity, $\boldsymbol{c_p}$ is the specific heat capacity, $\boldsymbol{\rho}$ is the mass density, $\dot{\boldsymbol{q}}=\frac{\boldsymbol{I^2R}}{\boldsymbol{V}}$ is the volumetric generated heat by the heating element.

3.2.2.1 Modelling Welding Assembly Parts Geometry

The FEM model contains the following components from the welding setup: Heating element (HE), GF/PEKK layer, thermal insulator and laminates to be welded.

Heating element
HE element was built as a continuous plate to decrease the modelling and computational effort. The length and width of the FEM modelled HE is identic to its physical analogue. Thickness of the FEM modelled HE in the case of the metal mesh is given by the mesh wire diameter and it will be

considered to be twice the mesh wire diameter (0.08 mm in the case of M200 mesh HE), in the case of plate heating element the real thickness of the laser cut plate will be modelled.

Laminates and GF/PEKK insulation layers
In order to save computational time, not the entire length of the laminates to be joined was modelled but only 60 mm instead of 101.6 mm. This assumption will be justified in section.3.3.1. Laminates and electrical insulation GF/PEKK layers were modelled on the same part, through this assuming an intimate contact between the glass layer and adherends. Thickness of the modelled part will be given by the laminate thickness plus the glass layer thickness, 2.358 mm in total.

Thermal Insulator
The modelled Insulator geometry is the same as it is in the real welding assembly assuming a tie constraint between the insulator block plates.

The FEM model size could be decreased based on the symmetries w.r.t. XZ and XY planes, however it was decided to model the entire welding assembly as an additional measure to check if all BC and loads were applied correctly. An asymmetry of the temperature distribution w.r.t. to XZ and XY planes would mean that the boundary conditions were wrongly assigned. The welding assembly modelled in Abaqus 2016-4 can be visualized below.

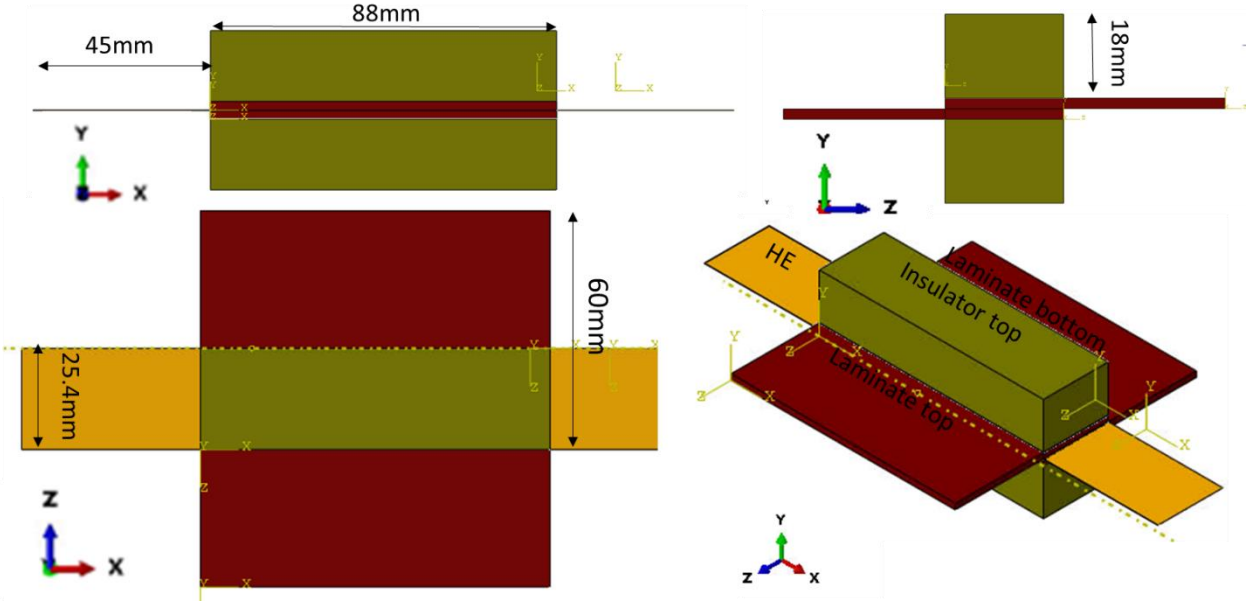

Figure 3.2-4: FEM model welding assembly

3.2.2.2 Boundary Conditions and Loads

A tie constraint between the modelled parts was applied, therefore it was assumed an intimate contact between the heating element and the laminates to be joined, and this assumption will be justified in section 3.3.2.
The thermal boundary conditions applied on all surfaces exposed to the environment are free convection and radiation with 22°C sink temperature. According to the literature free convection coefficient is $h = 5\ \frac{W}{m^2\,K}$ [12, 5, 20, 15, 4, 6] and surface emissivity coefficient is $\varepsilon = 0.95$ [12, 5, 20, 15, 4, 6]. The boundary condition formulation is presented in (3.2-8) equation.

$$-n \cdot (-k\nabla T) = h(RT - T) + \varepsilon\sigma(RT^4 - T^4)\text{[15] [4] [12]} \qquad (3.2\text{-}8)$$

The initial temperature of the whole assembly was set at the room temperature (RT) 22 °C.

The applied load is constant current intensity per surface $\left[\frac{A}{m^2}\right]$ and it is applied on one of the heating element surfaces in the YZ plane, on the opposite face an electrical BC in a form of 0 V potential was applied. It was assumed that the electrical clamps temperature will be constant during the welding process due to their high thermal inertia. Thus the electric contact clamps were not modelled but instead a temperature boundary condition equal to the RT was applied on the same faces where current load and 0V potential BC was applied.

3.2.2.3 Discretization

Global element size used to mesh the laminate parts and the insulator parts is about 1mm. The through-thickness element size used to mesh the heating element part is constraint by the modelled heating element thickness, however the in-plane element size is also about 1 mm. The element used for discretization is DC3D8E, an eight node linear coupled thermal-electrical brick element.
For the transient heat transfer analysis the minimum time increment in order to achieve convergence according to the Abaqus user manual [29] is dependent on the material properties and of the element size according to formula (3.2-9). Therefore the transient minimum step increment was set to 1 s and the maximum step was set to 4 s.

$$\Delta t = \frac{\rho \cdot C_p}{6 \cdot k} \Delta l^2 \text{ [29]} \qquad (3.2\text{-}9)$$

Where: $\boldsymbol{\Delta t}$ is the minimum time increment, $\boldsymbol{C_p}$ is the material heat capacity, $\boldsymbol{k}$ is the material thermal conductivity coefficient, $\boldsymbol{\Delta l}$ is the minimum element size.

3.2.3 FEM Model Material Properties

For the heat transfer part of the FEM model it is required to define the following temperature dependent thermal material properties: specific heat capacity, thermal conductivity, and temperature independent density. The material density will be considered to be temperature independent because the thermal expansion coefficient was not taken into account, therefore the modelled parts volume will be constant during the simulated welding process. Assigning temperature dependent density while keeping the volume of the parts constant will lead to the model mass variation which is inaccurate. For the electrical part of the model the temperature dependent electrical conductivity of the modelled heating element is required.

3.2.3.1 Insulator

The insulator thermal conductivity at 100 °C and 200 °C and mass density at RT was provided by the insulator material supplier **AGK-Hochleistungswerkstoffe GmbH.** The material specific heat capacity used in the model was found from a data sheet of the same material but from a different supplier **THE GUND COMPANY.** In Table 3.2-4 the insulator material properties used for the FEM model are presented.

Table 3.2-4: Insulator material thermal properties

Temperature [°C]	Thermal conductivity [30] [W/(m·K)]	Specific heat capacity [31] [J/(kg·K)]	Mass density [30] [kg/m^3]
22	0.25[1]	822	2200
100	0.26	890[2]	
200	0.28	978[2]	
250	0.29[1]	1081	
300	0.3[1]	1125[2]	

[1] *Interpolated/Extrapolated values based on data from* [30]
[1] *Interpolated/Extrapolated values based on data from* [31]

3.2.3.2 Laminate

The laminate temperature dependent thermal properties used for FEM model are presented in Table 3.2-5. The measurements were performed by EXPERTA Testing in Eindhoven, The Netherlands and the test report is attached to the appendix A.11. The material temperature dependent specific heat was measured through the differential scanning calorimetry (DSC), according to the DIN51007 method. The tests were performed on 18.2 mg samples. The material specific heat capacity measurements were performed twice. For the first measurement the test sample was collected from a UD ply, and for the second set of measurements the samples were collected from a 2.2 mm thick consolidated laminate having the same layup stacking sequence as the specimens used for the welding trials. At RT the specific heat measured on the test sample collected from a UD layer was 32% higher than the specific heat measured on a sample collected from the consolidated laminate. This difference was not expected since the test was performed on identic materials. The explanation of this deviation is that the test samples are not representative for the material they were taken from, because the size of a sample was only 18 mg having the volume of a cube with 2 mm edge length. Consequently the fibre volume content of the samples is different from the fibre volume content of the tested composites. From DSC graph of the UD sample the glass transition temperature (Tg = 160 °C), crystallization temperature (Tc = 210 °C) and melting temperature (Tm = 340 °C) can be clearly identified. While from the DSC graph of the sample taken from QIL only the melting point can be clearly identified. Tg, Tc and Tm are resin characteristics, therefore it can be concluded that Cp values obtained from UD sample are influenced more by PEKK properties than Cp values obtained from QIL sample were absence of Tc and Tg is a clear sign that the Cp values were dominated by the CF properties. During the FEM model validation described in section 3.3.4, by using the reported specific heat capacity for the UD sample from EXPERTA report led to the FEM model temperature predictions to be higher than the experimental measurements. An increase of the reported specific heat capacity by 20% led to a good fitting between FEM model predictions and experimental measurements.
The temperature dependent thermal conductivity was measured using the modified transient plane source (MTPS) method. The thermal conductivity was measured for the UD laminate and for the QIL. For the UD laminate the thermal conductivity was measured in-plane along the fibre and perpendicular to the fibres. For the QIL, the thermal conductivity was measured along one of the in-plane axis and through thickness. The through thickness conductivity of the QIL fits well conductivity of the UD laminate transversal to the fibres, which is a strong indicator that thermal conductivity measurements are reliable. The thermal conductivity measurements were performed on 2 cm edge cube-shaped specimens. The laminates from which the specimens were cut were manufactured at DLR in Stade; one UD and one QIL block with the dimension 2 x 9 x 8 cm the laminates were consolidated in an autoclave by stacking nine 2.2 mm thick consolidated laminates. The obtained blocks contained 108 prepegs layers. Before cutting the specimens to be tested from the manufactured laminates, they were inspected by ultrasonic scanning for the defects detection at the Airbus laboratories in Stade, no defects were found. Based on the fact that the thermal conductivity measurements were performed on a defect-free thick laminate block and that the through thickness conductivity of the QIL specimens matches thermal conductivity perpendicular to the fibres of the UD specimen, it can be concluded that thermal conductivity data provided by EXPERTA is reliable.
Laminate properties used for the FEM model are presented in Table 3.2-5.

Table 3.2-5: Laminate thermal properties

Temperature [°C]	Thermal cond[1] [W/(m·K)]		Specific heat capacity[2] [J/(kg·K)]	Mass density[3] [kg/m^3]
	k_x, k_z	k_y		
20	2.24	0.68	984	1535
40	2.41	0.69	1020	
60	2.57	0.69	1056	
80	2.74	0.70	1092	

100	2.90	0.71	1092	
120	2.95	0.72	1104	
140	3.01	0.73	1128	
160	3.06	0.75	1248	
180	3.11	0.76	1296	
200	3.12	0.77	1116	
220	3.13	0.78	1596	
240	3.14	0.79	1440	
260	3.15	0.80	1536	
280	3.16	0.81	1656	
300	3.16	0.83	1908	
320	3.17	0.84	2244	
340	3.18	0.85	2352	
360	3.19	0.86	2232	
380	3.20	0.87	2364	
400	3.20	0.88	2580	
420	3.21	0.89	2880	
440	3.22	0.91	3360	

[1] Reported by EXPERTA
[2]Cp for UD specimen from EXPERTA report increased by 20%
[3] Reported by EXPERTA

3.2.3.3 Electrical Insulation, Glass Layer

The glass layer properties used for the electrical insulation of HE were approximated using the temperature thermal properties of CETEX® GF/PPS prepreg from TenCate Advanced Composites with 50% fibre volume fraction reported in [15]. The article contains temperature dependent specific heat capacity of PPS and GF/PPS, mass density of GF, PPS and GF/PPS, temperature depended thermal conductivity of GF, PPS and GF/PPS.
Density of the GF/PEKK layer was calculated using the following formula (3.2-10).

$$\rho_{GF/PEKK} = \rho_{PEKK} \cdot (1 - v_{GF}) + \rho_{GF} \cdot v_{GF} \tag{3.2-10}$$

Where: $\boldsymbol{\rho_{PEKK}}$ is given in Table 3.2-8 and it is PEKK mass density, $\boldsymbol{v_{GF}}$ is volumetric fraction of glass fibres, $\boldsymbol{\rho_{GF/PEKK}}$ and $\boldsymbol{\rho_{GF}}$ are density of the glass fabric prepreg and respectively of the glass fibre.
The specific heat of GF was derived using the rule of mixtures, formula (3.2-11).

$$Cp_{GF}(T) = \frac{\rho_{GF/PPS}\left[Cp_{GF/PPS}(T) + \frac{Cp_{PPS}(T)\rho_{PPS}(v_{GF} - 1)}{\rho_{GF/PPS}}\right]}{\rho_{GF} \cdot v_{GF}} \tag{3.2-11}$$

Knowing the GF/PEKK density and Specific heat of GF and of PEKK the specific heat of GF/PEKK was calculated according to (3.2-12) formula.

$$Cp_{GF/PEKK}(T) = \frac{Cp_{GF}(T) \cdot \rho_{GF} \cdot v_{GF} + Cp_{PEKK}(T) \cdot \rho_{PEKK} \cdot (1 - v_{GF})}{\rho_{GF/PEKK}} \tag{3.2-12}$$

The temperature dependent heat conductivity was taken as it was presented in [15], because the conductivity of PEKK is close to the thermal conductivity of PPS and both prepregs have identic

fibre volume fraction. Also it was considered to be independent of temperature since the conductivity presented in [15] does not vary too much with the temperature increase. The resulted thermal properties of the modelled GF/PEKK are summarized in Table 3.2-6.

Table 3.2-6: GF/PEKK thermal properties

Temperature [°C]	Thermal cond [W/(m·K)]		Specific heat capacity [J/(kg·K)]	Mass density [kg/m^3]
	k_x, k_z	k_y		
20	0.6	0.45	1004	1689
40			1034	
60			1070	
80			1114	
100			1150	
120			1186	
140			1217	
160			1273	
180			1332	
200			1373	
220			1415	
240			1433	
260			1451	
280			1474	
300			1506	
320			1616	
340			1926 [a]	
360			1529 [a]	
380			1554 [a]	
400			1572 [a]	
420			1590 [a]	
440			1608[a]	

[a] Extrapolated values

3.2.3.4 Heating Elements

The HE will not be modelled as they are, because it will unnecessarily increase the modelling effort and computational time, especially in the case of M200 meshes HE modelling. Thus M200 mesh HE, Concept_1_0 and Concept_1_1 HE will be modelled as a continuous orthotropic plate which means that equivalent properties should be derived and assigned to the FEM modelled HE in order to make it to behave as the physical model it represents. Concept_2 HE modelling strategy is slightly different, the longitudinal conductive metal paths will be modelled as they are. The space between the longitudinal conductive paths containing transversal wire paths and resin will be modelled as a continuous strip.
The modelled HE element can be roughly divided into two regions: the HE region out of the welding stack and HE region sandwiched between the laminates to be welded. The thermal properties of the heating element out of the welding stack will depend of the stainless steel material properties only. While the thermal properties of the HE region inside the welding stack will depend on the resin thermal properties and on stainless steel thermal properties. Since PEKK is an electrical insulator the electrical conductivity of the modelled HE will depend on stainless steel resistivity only, the geometry of the physical HE element and the geometry of the modelled HE. Thermal properties of AISI 304 steel and of PEKK used to derive the thermal properties of the heating elements modelled are presented in tables Table 3.2-7 and Table 3.2-8.

Table 3.2-7: AISI 304L stainless steel thermal and electrical properties

Temperature[°C]	Thermal cond [W/(m·K)] [32]	Specific heat capacity [J/(kg·K)][1] [33]	Electrical resistivity [Ω*m] [32]	Mass density [kg/m^3] [33]
22	14.76	464.1	$71.3 \cdot 10^{-8}$	7900
27	14.89	465.5	$71.9 \cdot 10^{-8}$	
77	15.79	475.7	$76 \cdot 10^{-8}$	
127	16.61	485.9	$79.8 \cdot 10^{-8}$	
227	18.28	506.3	$86.8 \cdot 10^{-8}$	
327	19.77	506.7	$93.3 \cdot 10^{-8}$	
427	21.21	502.8	$99.2 \cdot 10^{-8}$	
527	22.59	509.9	$104.3 \cdot 10^{-8}$	
627	23.99	546.6	$108.6 \cdot 10^{-8}$	
727	25.33	583.2	$112.5 \cdot 10^{-8}$	
827	26.58	616.8	$115.8 \cdot 10^{-8}$	
927	27.81	641.8	$118.7 \cdot 10^{-8}$	

[1]Data from [33] was interpolated in order to fit the temperature scale from [32]

Table 3.2-8: PEKK thermal properties

Temperature [°C]	Thermal cond [W/(m·K)] [34]	Specific heat capacity [J/(kg·K)] [34]	Mass density [35] [kg/m^3]
20	0.25	1110	1300
60		1110	
80		1160	
100		1210	
120		1260	
140		1310	
160		1460	
180		1540	
200		1610	
220		1660	
240		1720	
260		1760	
280		1760	
300		1850	
320		2100	
340		2870	
360		1800	
380		1830	
400		1840	

For the HE thermal material properties derivation PEKK thermal conductivity is considered to be constant since thermal conductivity of PEKK is two orders of magnitude lower than stainless steel thermal conductivity.

FEM Modelled M200 Mesh Thermal and Electrical Properties Derivation.

M200 mesh heating element will be modelled as a continuous plate. Thus equivalent thermal properties of the HE necessary to be assigned to the modelled HE should be derived. In this section only the properties of the HE inside the welding stack will be derived (green area Figure 3.2-5).

Figure 3.2-5: Continuous plate HE FEM modelling strategy. M200 HE (Top), FEM modelled HE (Bottom)

Equivalent density
Equivalent density of the HE inside the welding stack can be calculated with the following formula (3.2-13).

$$\rho_{mesh\_eq\_iws} = \frac{\rho_{peek} \cdot Vol_{pekk} + \rho_{steel} \cdot Vol_{steel}}{Width \cdot Length_{iws} \cdot th} \quad (3.2\text{-}13)$$

Where: $\boldsymbol{\rho_{mesh\_eq\_iws}}$ is equivalent mesh HE density inside the welding stack, $\boldsymbol{\rho_{peek}}$ is PEKK mass density, $\boldsymbol{Vol_{pekk}}$ is PEKK volume contained by the HE, $\boldsymbol{Vol_{steel}}$ is steel volume of the mesh given by the volume of all wires and its calculation methods is attached to the appendix A.1, $\boldsymbol{Width}$ is the HE width, $\boldsymbol{Length_{iws}}$ is HE length at the welding interface, $\boldsymbol{th}$ is HE thickness.

Modelled HE density out of the welding stack will be resin-less therefore its density will depend only on stainless steel density and on the geometry of the FEM modelled HE according to equation (3.2-14)

$$\rho_{mesh\_eq\_ows} = \frac{\rho_{steel} \cdot Vol_{steel}}{Width \cdot Length_{ows} \cdot th} \quad (3.2\text{-}14)$$

Where: $\boldsymbol{\rho_{mesh\_eq\_ows}}$ is equivalent mesh HE density out of the welding stack, $\boldsymbol{Length_{ows}}$ is HE length out of the welding stack.

Equivalent specific heat capacity
Equivalent specific heat capacity of the HE inside the welding stack can be derived with formula (3.2-15).

$$Cp_{mesh\_eq\_iws}(T) = \frac{\rho_{steel} \cdot \nu_{steel\_mesh\_eq} \cdot Cp_{steel}(T) + \rho_{pekk} \cdot \left(1 - \nu_{steel\_mesh\_eq}\right) \cdot Cp_{pekk}}{\rho_{mesh\_eq\_ws}} \quad (3.2\text{-}15)$$

Where: $\boldsymbol{Cp_{mesh\_eq\_iws}(T)}$ is temperature dependent specific heat capacity of the mesh HE inside the welding stack, $\boldsymbol{\nu_{steel\_mesh\_eq}}$ is steel volumetric fraction contained by the modelled HE and it can simply be found, from the total volume of the modelled HE and the calculated volume of steel contained by the modelled HE according to (3.2-17) formulation.

Equivalent specific heat of the HE out of the welding stack is resulting from (3.2-16) formulation:

$$Cp_{mesh\_eq\_ows}(T) = \frac{\rho_{steel} \cdot \nu_{steel\_mesh\_eq} \cdot Cp_{steel}(T)}{\rho_{mesh\_eq\_ows}} \quad (3.2\text{-}16)$$

Where: $\boldsymbol{Cp_{mesh\_eq\_ows}(T)}$ is the temperature dependent specific heat capacity of the mesh HE out of the welding stack.

$$\nu_{steel\_mesh\_eq} = \frac{Vol_{steel}}{Width \cdot Length \cdot th} \tag{3.2-17}$$

Equivalent thermal conductivity

Temperature dependent thermal conductivity of the HE element in the tailored region is calculated using the rule of mixtures as it is explained below:

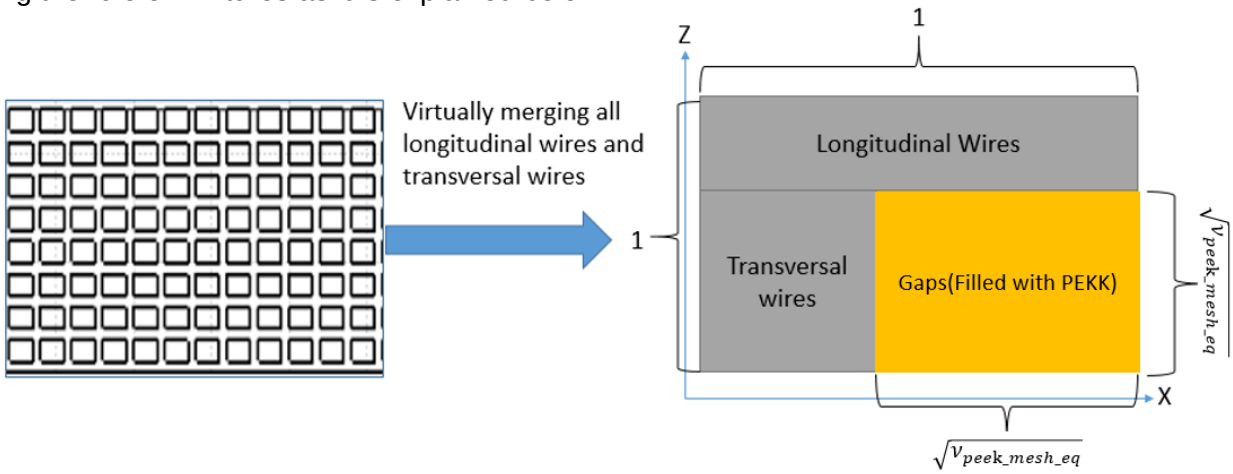

Figure 3.2-6: HE thermal conductivity calculation

From the picture above it can be seen that after virtually merging the wires contained by the HE three distinct regions will be obtained: Longitudinal wires, Transversal wires and Gaps. The conductivity in Z direction (in-plane) can be calculated as following: first the conductivity given by the transversal wires and gaps will be calculated (rule of mixtures in parallel), second the conductivity obtained from the previous step will be added to the conductivity of the longitudinal wires (rule of mixtures in series.)

The in-plane thermal conductivity can be calculated with the following formulation:

$$\begin{aligned} k_{z1}(T) &= \sqrt{\nu_{peek\_mesh\_eq}} \cdot k_{pekk} + \left(1 - \sqrt{\nu_{peek\_mesh\_eq}}\right) \\ &\quad \cdot k_{steel}(T)\ (rule\ of\ mixtures\ parallel) \\ k_z(T) &= \left[\frac{\sqrt{\nu_{peek\_mesh\_eq}}}{k_{z1}(T)} + \frac{1 - \sqrt{\nu_{peek\_mesh\_eq}}}{k_{steel}(T)}\right]^{-1} \quad (rule\ of\ mixtures\ series) \end{aligned} \tag{3.2-18}$$

**(T) Denotes that property is temperature dependent*

Where: $\boldsymbol{k_z(T)}$ is the temperature dependent thermal conductivity coefficient in the Z direction.

The modelled HE through thickness thermal conductivity can be calculated using the rule of mixtures in parallel:

$$k_y(T) = \nu_{peek\_mesh\_eq} \cdot k_{pekk} + \nu_{steel\_mesh\_eq} \cdot k_{steel}(T)\ \ (rule\ of\ mixtures\ paralel) \tag{3.2-19}$$

**(T) Denotes that the property is temperature dependent*

Where: $\boldsymbol{k_{pekk}}$ is PEKK the thermal conductivity, $\boldsymbol{k_{steel}(T)}$ is the temperature dependent steel thermal conductivity, $\boldsymbol{\nu_{peek\_mesh\_eq}}$ is the volumetric ratio of PEKK contained by the modelled HE, $\boldsymbol{\nu_{steel\_mesh\_eq}}$ is the volumetric ratio of steel contained by the modelled heating element.

Equivalent electrical conductivity

The equivalent electrical conductivity of the modelled HE element plate can be calculated with the following formula:

$$cond_{eq}(T) = \frac{Length_{iws}}{R_{iws}(T) \cdot Width \cdot th}$$ [15] (3.2-20)

**(T) Denotes that the property is temperature dependent*

Where: $\boldsymbol{Length_{iws}}$ is the HE length inside the welding stack, $\boldsymbol{Width}$ is the width of the HE, $\boldsymbol{th}$ is the thickness of the modelled HE, $\boldsymbol{R_{iws}(T)}$ is the HE temperature dependent resistance inside the welding stack calculated with formula (3.2-21)

It is assumed that the current will flow only along the longitudinal "wires". Based on this assumption the resistance of a stainless steel mesh can be calculated

$$R_{iws}(T) = res_{steel}(T) \frac{Length_{iws}}{\pi \left(\frac{d}{2}\right)^2 \cdot N\_long} = res_{steel}(T) \frac{Length_{iws}}{\pi \left(\frac{d}{2}\right)^2 \cdot \frac{Width}{d+g}} \quad (3.2\text{-}21)$$

Where: $\boldsymbol{res_{steel}(T)}$ is the electrical resistivity of stainless steel, $\boldsymbol{N\_long}$ is the number of longitudinal wires, $\boldsymbol{d}$ is the mesh HE wire diameter, $\boldsymbol{g}$ is mesh HE gap size, $\boldsymbol{Width}$ is the HE width.

The length of the mesh wire is higher than the length of the mesh itself, because the wires contained by the mesh are curved. However in the formula above the Length of the wire will be assumed to be the length of the mesh, because the current flow path is shorter than the longitudinal wires length, due to the fact that at the intersection points between transversal wires and longitudinal wires the current will flow through the transversal wires.
By inserting (3.2-21) into (3.2-20) will be obtained the equivalent conductivity of the modelled HE in function of the mesh diameter, mesh gap and thickness of the M200 mesh FEM modelled equation (3.2-22)

$$cond_{eq\_mesh}(T) = \frac{\pi \left(\frac{d}{2}\right)^2 \cdot \frac{1}{d+g}}{res_{steel}(T) \cdot th} \quad (3.2\text{-}22)$$

Where: $\boldsymbol{cond_{eq}(T)}$ is the HE electrical conductivity.
The derived thermal properties of FEM modelled M200 mesh are attached to the appendix A.2

FEM modelled Concept 1 thermal and electrical properties derivation.
In the case of laser cut plate HE the properties of the HE inside the welding stack must be calculated (grey area Figure 3.2-7). The HE properties out of the welding (blue area Figure 3.2-7) stack will be equal to stainless steel properties.

Figure 3.2-7: Continuous plate HE FEM modelling strategy. Laser cut plate HE (Top), FEM modelled HE (Bottom)

Density
Plate equivalent density in the tailored region can be calculated with formula (3.2-23).

$$\rho_{plate\_eq\_iws} = \rho_{peek} \cdot OAR + \rho_{steel}(1 - OAR) \tag{3.2-23}$$

Where: $\boldsymbol{\rho_{plate\_eq\_iws}}$ is the HE equivalent density in the tailored region, $\boldsymbol{OAR}$ is the HE open area ratio and it can be calculated with formula (3.2-24).

$$OAR = \frac{g\_l \cdot N\_trans + g\_w \cdot (N\_trans)}{Width \cdot Length_{iws} \cdot} \tag{3.2-24}$$

Where:$\boldsymbol{g\_l}$ and $\boldsymbol{g\_w}$ are the gap dimensions along the length of the heating elements respectively along the width, $\boldsymbol{N\_trans}$ is the HE transversal wires number.

Specific heat capacity
The specific heat capacity $\boldsymbol{Cp_{plate\_eq}(T)}$ is calculated with the formula below:

$$Cp_{plate\_eq}(T) = \frac{\rho_{steel} \cdot (1 - OAR) \cdot Cp_{steel}(T) + \rho_{pekk} \cdot (OAR) \cdot Cp_{pekk}}{\rho_{plate\_eq\_iws}} \tag{3.2-25}$$

Thermal conductivity: In-plane
The in-plane thermal conductivity is calculated by based on the approach presented in Figure 3.2-6 and equation (3.2-18). The resulted formulation can be seen below:

$$\begin{gathered} k_{z1}(T) = \sqrt{OAR} \cdot k_{pekk} + \left(1 - \sqrt{OAR}\right) \cdot k_{steel}(T)\ (rule\ of\ mixtures\ parallel) \\ k_z(T) = \left[\frac{\sqrt{OAR}}{k_{z1}(T)} + \frac{1 - \sqrt{OAR}}{k_{steel}(T)}\right]^{-1}\ (rule\ of\ mixtures\ series) \end{gathered} \tag{3.2-26}$$

Thermal conductivity: through-thickness

$$k_y(T) = OAR \cdot k_{pekk} + (1 - OAR) \cdot k_{steel}(T)\ \ (rule\ of\ mixtures\ paralel) \tag{3.2-27}$$

Equivalent electrical conductivity.

$$cond_{eq\_plate\_iws}(T) = \frac{th \cdot w\_l \cdot N\_long}{res_{steel}(T) \cdot Width \cdot th} \tag{3.2-28}$$

Where: $\boldsymbol{w\_l}$ is the longitudinal wire width, $cond_{eq\_plate\_iws}(T)$ is resulted equivalent conductivity of the plate HE inside the welding stack.

The derived properties of modelled Concept_1_0 and Concept_1_1 based on the formulas presented in this section are attached to the appendix.A.3.

FEM modelled Concept 2 thermal and electrical properties derivation.
The properties of the material out of the welding stack and of the conductive paths is stainless steel properties (blue area Figure 3.2-8).The material properties of the strip between two longitudinal path should be derived (red lines Figure 3.2-8).

Figure 3.2-8: Longitudinal wires model HE FEM modelling strategy. Laser cut plate HE (Top), FEM modelled HE (Bottom)

Strip Density

$$\rho_{str\_eq} = \rho_{peek} \cdot OAR_{str} + \rho_{steel}(1 - OAR_{str}) \tag{3.2-29}$$

OAR_{str} can be calculated with equation (3.2-30)

$$OAR_{str} = \frac{g\_l \cdot N\_trans \cdot g\_w}{g\_w \cdot Length_{iws}\cdot} \tag{3.2-30}$$

Strip Specific heat capacity

$$Cp_{str\_eq}(T) = \frac{\rho_{steel} \cdot (1 - OAR_{str}) \cdot Cp_{steel}(T) + \rho_{pekk} \cdot (OAR_{str}) \cdot Cp_{pekk}}{\rho_{str\_eq}} \tag{3.2-31}$$

Thermal conductivity of the strips in x direction

$$k_x(T) = \left[\frac{OAR_{str}}{k_{pekk}} + \frac{1 - OAR_{str}}{k_{steel}(T)}\right]^{-1} \ (rule\ of\ mixtures\ series) \tag{3.2-32}$$

Thermal conductivity of the strips in y and z direction

$$k_{y,z}(T) = OAR_{str} \cdot k_{pekk} + (1 - OAR_{str}) \cdot k_{steel}(T) \ \ (rule\ of\ mixtures\ paralel) \tag{3.2-33}$$

Electrical conductivity
Strips are electrical conductive in Z and Y direction due to the transversal paths.
Equivalent electrical conductivity between Z and Y direction can be calculated with formula *(3.2-34)*

$$\sigma_{str\_eq\_z\_y}(T) = \frac{t\_w \cdot N\_trans}{res_{steel}(T) \cdot Length_{iws}\cdot} \tag{3.2-34}$$

The derived properties based on Formulas above for the Concept_2 HE are attached to the appendix A.4

3.3 FEM MODEL VALIDATION

3.3.1 Modelled Insulator and Laminate Size Assumption Justification

The minimum thickness of the thermal insulation blocks required to be modelled is the maximum thickness value of the thermal insulation block affected by generated heat by the HE during the welding process. Similar statement is valid regarding the minimum adherends length required to be

modelled. The heat affected zone (HAZ) size is dependent of IPS and welding time. The lower the IPS, the longer the welding time, consequently energy loss will be higher.
The temperature measurements were taken between the thermal insulation plates TCa position pictured in Figure 3.3-1(15mm from the laminate to be joined) and on the laminate surface TCb position pictured in Figure 3.3-1 (2.5 cm from the welding interface) by using TC during a welding trial using Concept_1 HE under the following welding parameters: Initial power per surface at the welding interface $51\ \frac{kW}{m^2}$ and 140 s welding time. These welding parameters led to an increase of the welding interface temperature to 380 °C, while the temperature shown by the thermocouple between the insulator plates and on the laminate did not change. That means that the temperature distribution is independent of the laminate material properties above 2.5 cm from the welding interface for the initial power levels higher than $51\frac{kW}{m^2}$ and welding time lower than 140 s. A similar conclusion can be deducted regarding the insulator block thickness, for initial power levels higher than $51\frac{kW}{m^2}$ and welding time lower than 140 s the temperature distribution will be independent of the insulator block properties above 15 mm from the laminate. As a margin of safety in the case the FEM modelled laminate length will be assumed to be 60 mm (14.6 mm longer than required). The insulator thickness will be 19 mm as it is in the welding assembly (4 mm longer than it is required)

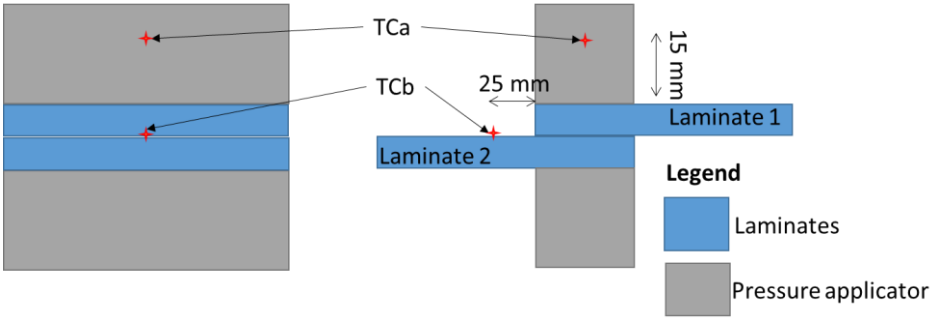

Figure 3.3-1: Thermocouple positions during experimental measurements for the modelled size of the insulator and of the laminate assumption validation

3.3.2 Tie Constraint/Intimate Contact Assumption Justification

To justify the intimate contact assumption the following experiment was performed: a thermocouple was placed in the middle of the welding interface between the impregnated HE and the laminate to be welded (position T1 in Figure: 4.1-2). The assembly was welded under the following parameters: IPS of $51\ \frac{kW}{m^2}$ and 140 s welding time. After the welded assembly cooled down to the RT, the obtained joint was reheated under identic parameters. If the intimate contact assumption is valid, negligible temperature differences should be expected between the welding and reheating processes. The experiment was performed using five different types of heating elements. One joint was welded using M200 mesh HE and other four were welded using Concept_1_0 HE Type: C005, A01, C01, and B005. To achieve desired IPS of $51\frac{kW}{m^2}$ at the welding interface the current input applied to weld joint using Concept_1_0 Type A01 and C01 was 39 A and for Type B005 and C005 was 27.6 A, In the case of M200 mesh the necessary input current intensity to provide a IPS of $51\frac{kW}{m^2}$ at the welding interface was calculated with formula (3.3-1).

$$I = \frac{Length_{iws} \cdot Width \cdot \sqrt{\frac{IPS \cdot R_{iws}(22\ °C)}{Length_{iws} \cdot Width}}}{R_{iws}(22\ °C)} \tag{3.3-1}$$

Where: $\boldsymbol{I}$ is the current intensity, $\boldsymbol{Length_{iws}}$ is the overlap length, $\boldsymbol{Width}$ is the overlap width, $\boldsymbol{IPS}$ is the desired initial power per surface, $\boldsymbol{R_{iws}(22\ °C)}$ is the resistance given by the mesh HE in the region inside the welding stack at RT and can be calculated with formula(3.2-21).

Based on equation (3.3-1) the necessary current input to ensure an IPS of $51\ \frac{kW}{m^2}$ at the welding interface is 21.1 A.The temperatures measured by TC during the welding and reheating processes are shown in Figure 3.3-2.

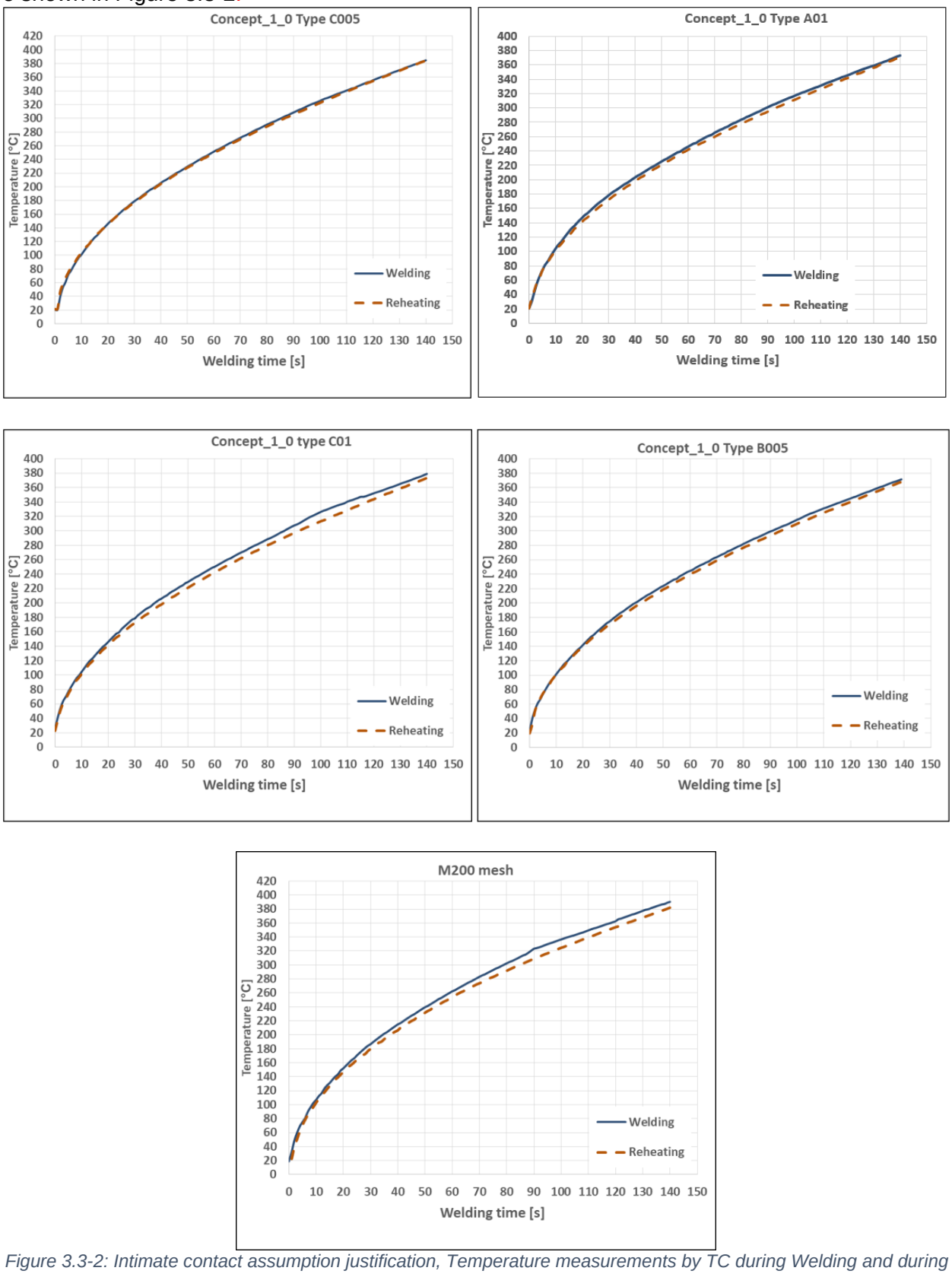

Figure 3.3-2: Intimate contact assumption justification, Temperature measurements by TC during Welding and during Reheating for 5 joints welded with different heating elements

From the graphs presented in Figure 3.3-2 it can be seen that generally the temperature in the case of joint reheating is lower than the temperature during the welding. The explanation is that during welding until the melting temperature is reached a small layer of air exists between the consolidated HE and the laminates, thus the air layer will impede the heat transfer between the laminates to be joined and the HE, which is leading to a temperature increase at the welding interface.
The average value of the temperature difference between the temperature at the end of the welding process and at the end of the reheating process is 4.22°C with the standard deviation of 2.6°C. These results fits well Ageorges [11] conclusion that the intimate contact can be assumed from the beginning of the welding process.

3.3.3 FEM Electrical Part Validation

The temperature at the welding interface is dependent on the amount of generated heat at the welding interface and on the welding assembly thermal material properties. Therefore the validation of HE was necessary to ensure that the generated heat by the FEM modelled HE matches the generated heat through the Joule effect by the plate HE during the welding process.
For that, Concept_1_0 TypeC01 HE was heated out of the welding stack, by applying a current of 17.3 A. The applied current resulted in an initial power per surface of $10\ \frac{kW}{m^2}$ in the region inside the welding stack and of $3.3\ \frac{kW}{m^2}$ in the region out of the welding stack. The temperature was measured on both regions using J-type TC built in the welding machine and with an IR camera. Kapton tape was used for the TC electrical insulation and fixation. Therefore two layers of Kapton tape per TC were used with the dimensions of 15 x 25.4 x 0.05 mm. The temperature of the Kapton layer covering the TC was measured with IR camera to check the TC measurements. The experimental setup is presented below:

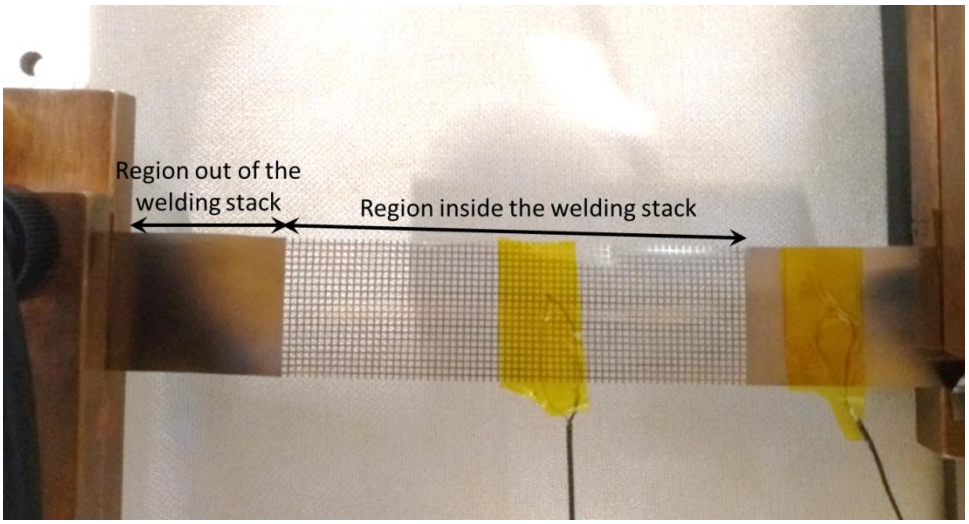

Figure 3.3-3: HE energy generation validation assembly

The derived heating element thermal and electrical properties used for the simulation are attached to the appendix A.5. Kapton tape thermal properties at RT are presented in Table 3.3-1.

Table 3.3-1: Kapton tape properties at RT

Thermal conductivity [W/(m·K)]	Specific heat capacity [J/(kg·K)]	Mass density [kg/m^3]
0.12	1090	1420

The predicted temperature by the simulation versus experimental temperature measurements are presented in Figure 3.3-4, for both: region inside the welding stack of the HE and region out of the welding stack.

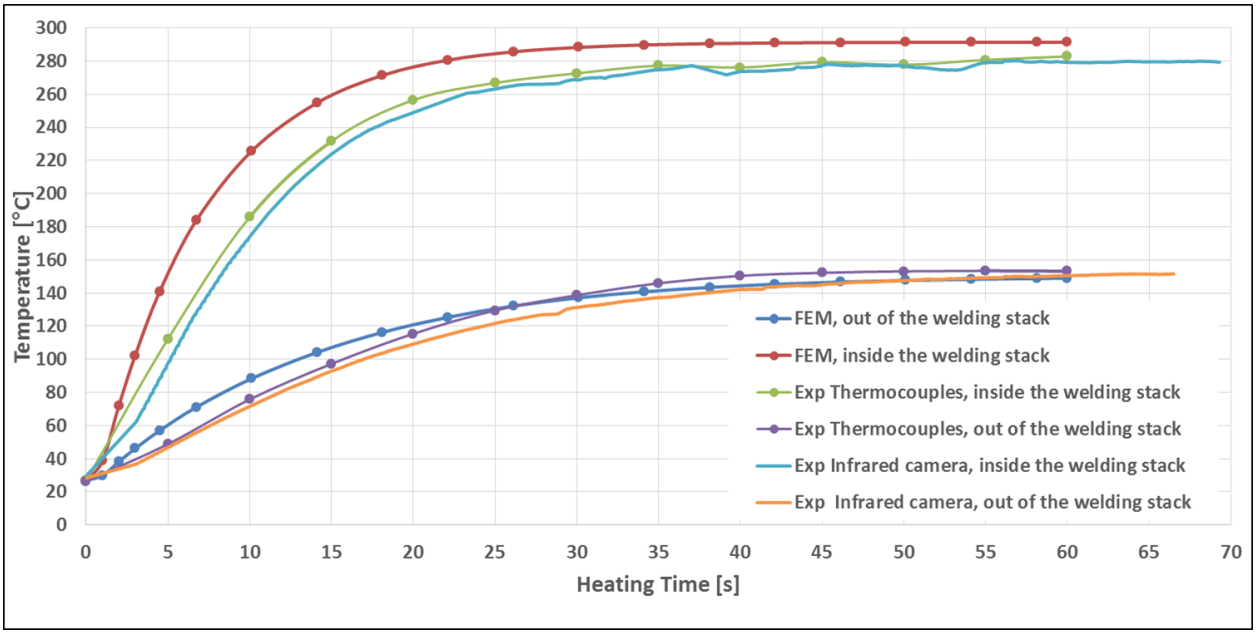

Figure 3.3-4: Concept 1 HE Temperature measured by TC and IR camera versus FEM ehen HE is heated out of the welding stack.

Figure 3.3-4 shows a good agreement between data measured by TC and data measured by IR camera. It can be seen that the temperatures showed by the TC in the transient state are slightly higher than the temperature measured by the IR camera, the explanation is that TCs are measuring the temperature between two Kapton layers while the IR camera is measuring the temperature on top of the second Kapton layer which covers the TC. In the transient step the temperature of the second layer is lower than the temperature of the first layer glued to the HE.
Another inconsistency is that in the transient state the temperature predicted by the FEM model is higher than the experimental measurements (by 12.5 °C of the region out of the welding stack at 10 s heating time), while at steady state the temperature difference tends to decrease (5.4 °C of the region out of the welding stack at 55s heating time). This is explained by the fact that in the transient state the temperature is heavily dependent on the material specific heat capacity, while the steady state temperature is independent of the specific heat capacity. Kapton tape specific heat capacity used in FEM model was considered to be temperature independent, however in reality it is heavily temperature dependent, for example for PEKK according to Table 3.2-8 specific heat capacity is increasing by 38% from RT to 180°C.Thus the source of the error between the FEM predictions and experimental measurements might be explained by a poor specific heat value estimation of Kapton tape. The difference between experimental measurements and FEM predictions are even higher in the case of the region inside the welding stack, FEM predicted temperatures being higher than experimental measurements. The explanation is that in the FEM model the HE was modelled as a continuous plate, while in reality it is discontinuous since the HE has holes in that region. Thus it seems that the HE holes in the region out of the welding stack aids HE cooling in that region.

3.3.4 FEM Heat Transfer Part Validation

The validation of the model was performed using Concept_1_0 heating elements for two initial power levels on the welding interface 51 $\frac{kW}{m^2}$ and 71.4 $\frac{kW}{m^2}$, the current input used was 39 A and respectively 45.7 A. Two IPS were used for validation to ensure that the created FEM simulation is valid for a IPS range rather than just for one value. The HE IPS out of the welding stack was 16.8 $\frac{kW}{m^2}$ for 39 A and 23.1 $\frac{kW}{m^2}$ for 45.7 A. The steady state temperatures of the HE element surface out of the welding stack are 445 °C for the 45.7 A current input and 383 °C for the 39 A current input. The temperatures were measured in the middle of the welding interface (T1), 3 mm from the centre of the transversal edge (T2, T4) 3 mm from the centre of the longitudinal edge (T3) and at

the centre of the contact surface between Laminate/Insulator (T5) a schematic picture of the thermocouples position is shown in Figure: 4.1-2.
FEM temperature predictions versus experimental measurements are shown in: Figure 3.3-5 to Figure 3.3-8.

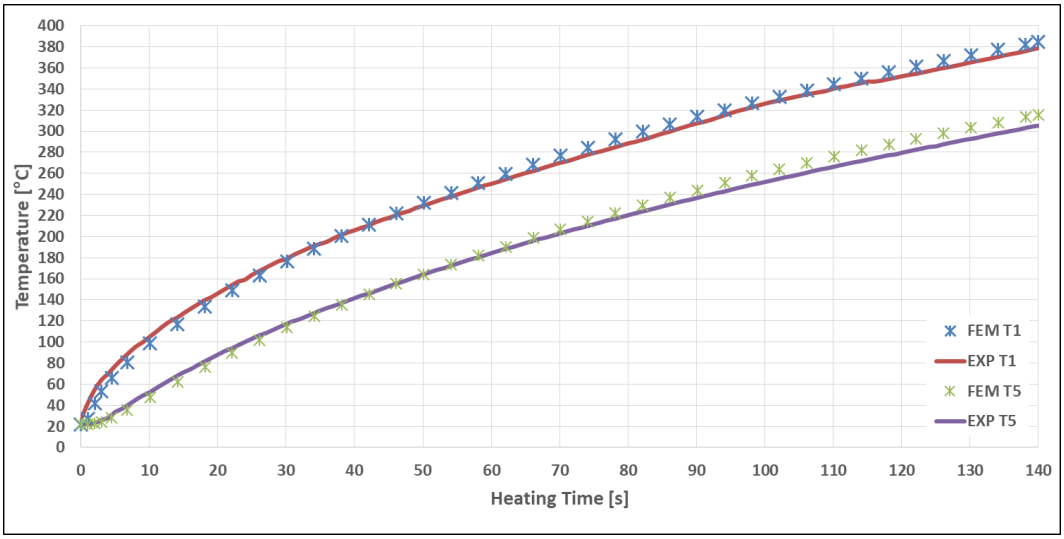

Figure 3.3-5: FEM predictions vs Experimental measured temperature in the middle of the welding interface (T1) and in the middle of the Insulator/Laminate contact interface (T5) for an initial power input of 51 kW/m^2

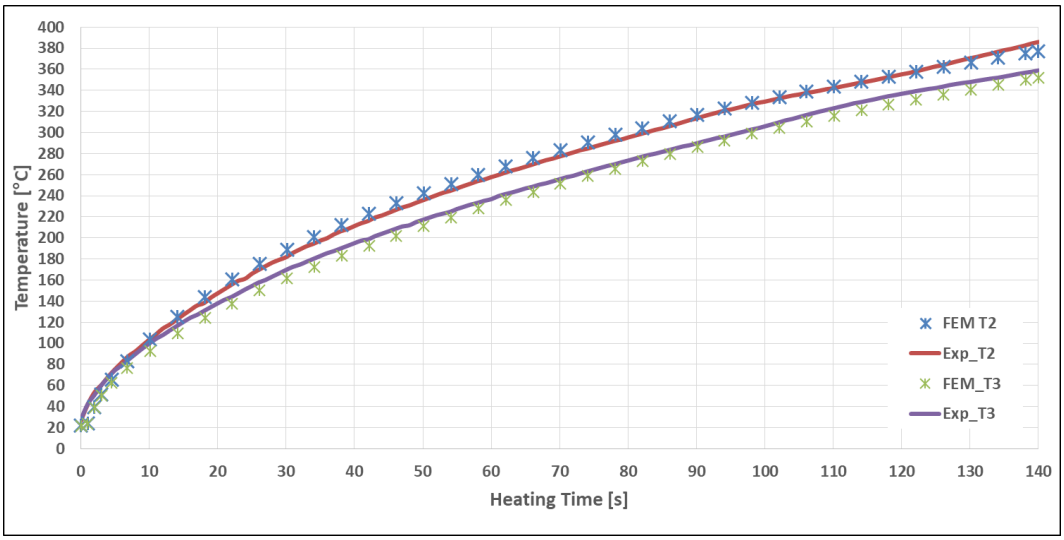

Figure 3.3-6: FEM predictions vs Experimental measured temperature 3 mm from the longitudinal edge (T3) and 3 mm from the transversal edge (T2) for an initial power input of 51 kW/m^2

From the pictures above can be seen that a welding time of 140 s for an initial power input of $51\ \frac{kW}{m^2}$ sufficed to bring the welding interface to 380 °C. It can be noticed from the graphs that at the end of welding process the temperature measured at T2 and T1 are the same. Therefore it can be concluded that longitudinal temperature uniformity can be achieved for these welding parameters.

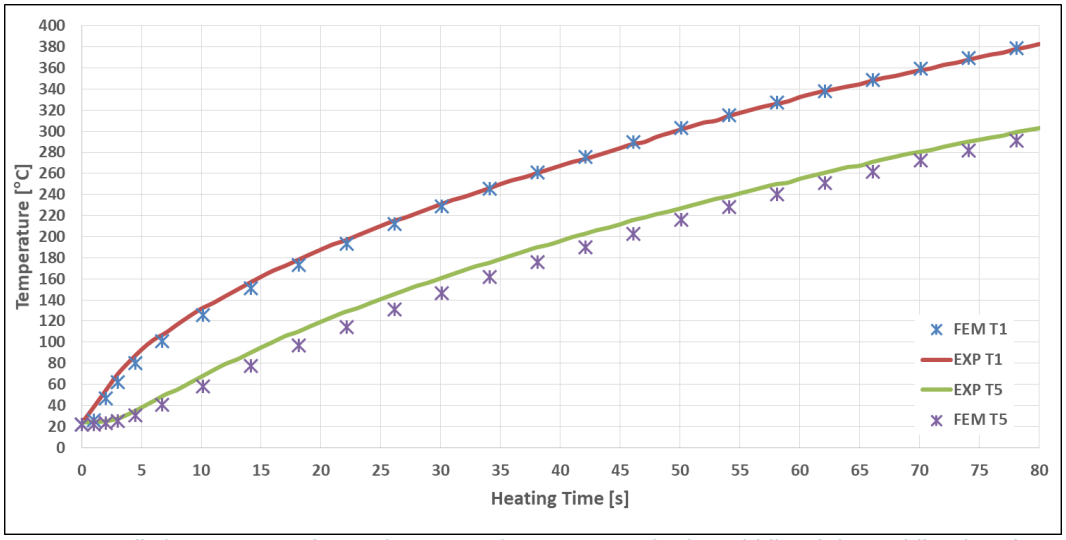

Figure 3.3-7: FEM predictions vs Experimental measured temperature in the middle of the welding interface (T1) and in the middle of the Insulator/Laminate contact interface (T5) for an initial power input of 71.4 kW/m^2

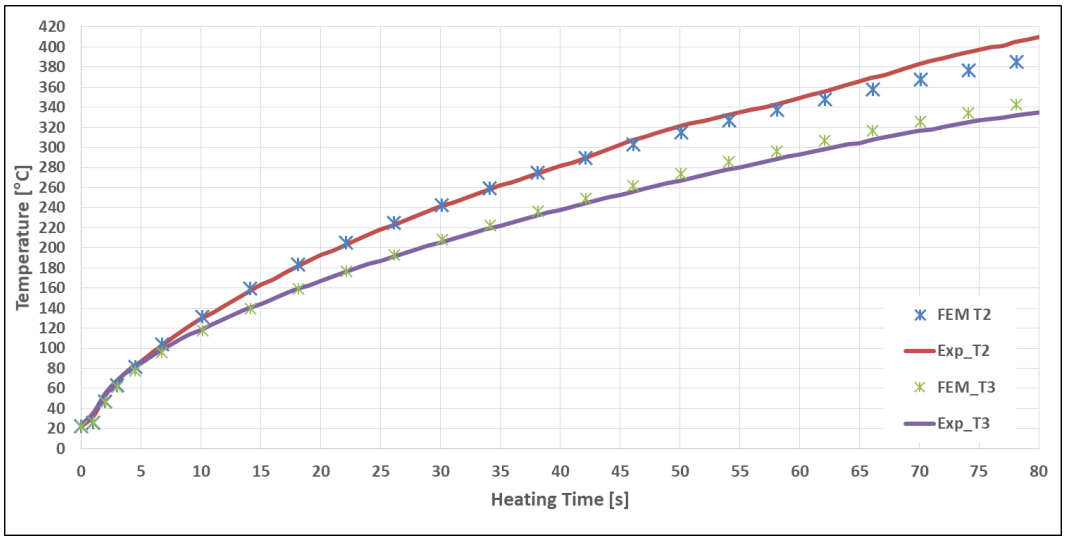

Figure 3.3-8: FEM predictions vs Experimental measured temperature 3 mm from the longitudinal edge (T3) and 3 mm from the transversal edge (T2) for an initial power input of 71.4 kW/m^2

From all four listed pictures a good fitting between Experimental data and FEM predictions can be seen. In the case of 71.4 $\frac{kW}{m^2}$ IPS a good agreement between the FEM simulation predicted temperature and measured temperature at T2 can be observed from RT up to 340 °C. However above this temperature a mismatch between the measured temperature and FEM predicted temperature can be spotted, measured temperature being higher. The explanation of this mismatch is that at 340 °C the resin starts to melt, consequently under the applied pressure, resin squeeze out and fibre movement occur, these made the TC move together with the resin towards the hotter transversal edge of the welding interface. The temperature of the transversal edge of the welding interface is higher in the case of 71.4 $\frac{kW}{m^2}$ IPS, because the steady state temperature of the HE out of the welding stack is 445 °C, while the temperature inside the welding interface inside the welding stack will not achieve this value during the welding process. The explanation was proved by the final position of the T2 TC, it moved by 2 mm towards the transversal edge during the welding process.

3.3.5 FEM Model Prediction Check with Experimental Measurements in the Case of Concept_1_1 HE and Concept_2 HE

Although the FEM model was validated in the previous section it was considered to check if the experimental temperature measurements of the joints welded with Concept_1_1 and Concept_2 match FEM predicted temperatures. The temperature measurements together with FEM predicted temperatures for Concept_1_1 and Concept_2 HE are shown in Figure 3.3-9, Figure 3.3-10. Joints welded with Concept_1_1 HE have the following welding parameters: 39 A current intensity, 71.4 $\frac{kW}{m^2}$ IPS in the region inside the welding stack, 16.83 $\frac{kW}{m^2}$ IPS in the region out of the welding stack, 75 s welding time. Joints welded with Concept_2 HE had the following welding parameters: 39 A current intensity, 71.4 $\frac{kW}{m^2}$ IPS in the Region3 inside the welding stack, 110.4 $\frac{kW}{m^2}$.IPS in the Region4 inside the welding stack, 16.83 $\frac{kW}{m^2}$ IPS in the region out of the welding stack, 75 s welding time. Region4 and Region3 of the HE inside the welding stack are marked in Figure 3.2-3.

Concept_1_1 HE led to an acceptable welding time of 75 s. In the case of Concept_2 the IPS in Region3 was found using an iterative process with the help of the coupled electrical heat transient FEM model by increasing IPS in Region3 until temperature transversal gradient was achieved; this request was fulfilled by an IPS equal to 110.4 $\frac{kW}{m^2}$. In order to keep the temperature of the un-tailored region at 383 °C the current intensity was fixed as in the case of Concept_1_1 to 39 A.

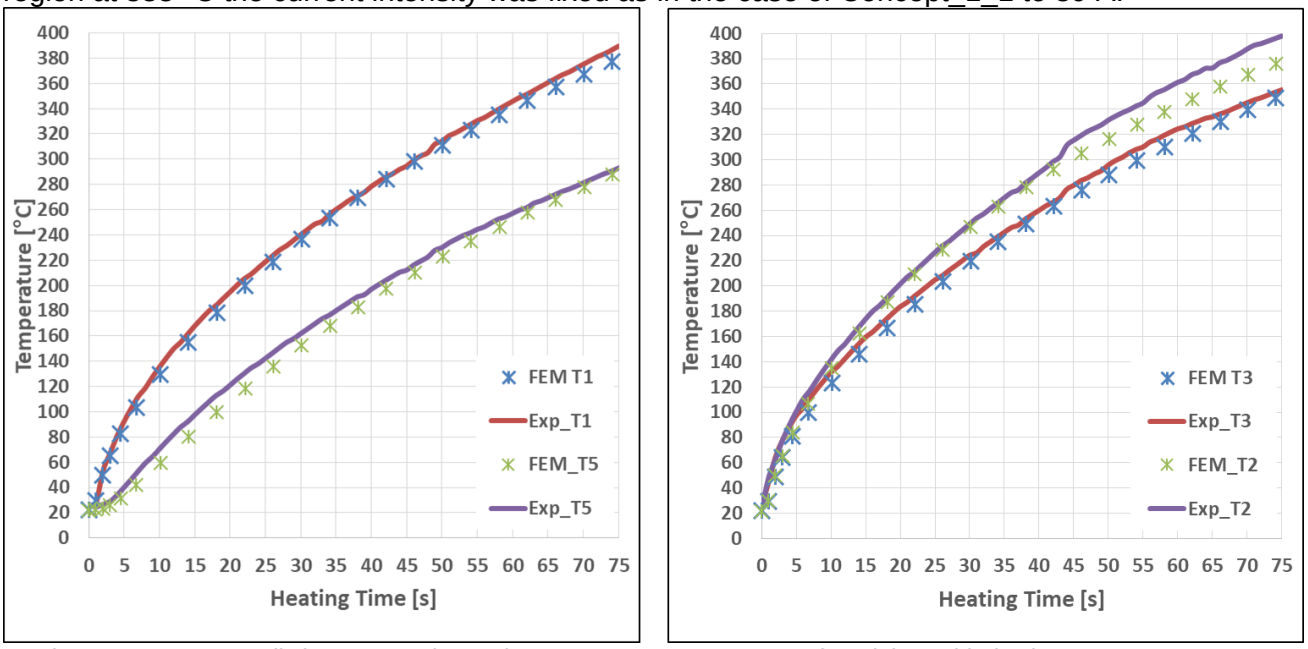

Figure 3.3-9 FEM prediction vs experimental temperature measurements for a joint welded using a Concept_1_1 HE

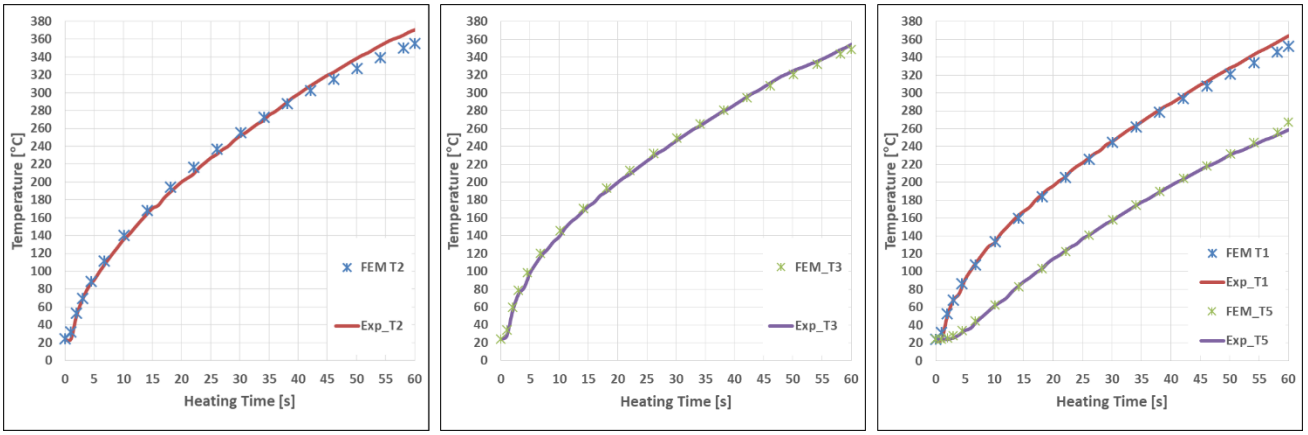

Figure 3.3-10: FEM predictions vs experimental temperature measurements for a joint welded using a Concept_2 HE

From the graphs presented above it can be seen that the FEM predictions fits well the experimental temperature measurements for Concept_2 and Concept_1_1 HE at T1 (center of the welding interface), T3 (3 mm from the overlap longitudinal edge), T5 (center of the adherend/thermal insulator interface). However the temperature measured at T2 (3 mm from the overlap transversal edge) is higher than the FEM predicted temperature for a joint welded with Concept_2 HE and for a joint welded with Concept_1_1 HE. The explanation given to the graph presented in Figure 3.3-8 that TC moved towards the transversal edge of the overlap is not valid for this case anymore. Because even if they did the temperature should not exceed the temperature of the HE untailored region out of the welding stack which was predicted to be 383 °C. But in the case of Concept_1_1, the thermocouple at T2 position showed 400 °C, 20 °C higher than the predicted temperature. The explanation of this mismatch is that the temperature at T2 position is highly sensitive to the relative distance between HE region inside the welding stack and adherend edges, in the FEM model it was consider to be 0 mm, thus the length of the overlap is considered to be equal to the length of the HE designed region to be inside the welding stack. In reality a mismatch will always exist between these two. This mismatch might come from the manufacturing tolerances of the HE, during the laser cutting process, from the tolerances of the cutting tool used to cut the adherends and the biggest mismatch source is the manual positioning of the HE inside the welding stack.
In Figure 3.3-11, temperature experimental measurements of a joint welded with Concept 2 HE when HE designed region to be inside the welding stack is 1mm out of the welding stack (case B Figure 3.3-12), together with the FEM predictions for an ideal case (case A Figure 3.3-12) when overlap length coincides with the HE tailored region length are shown.

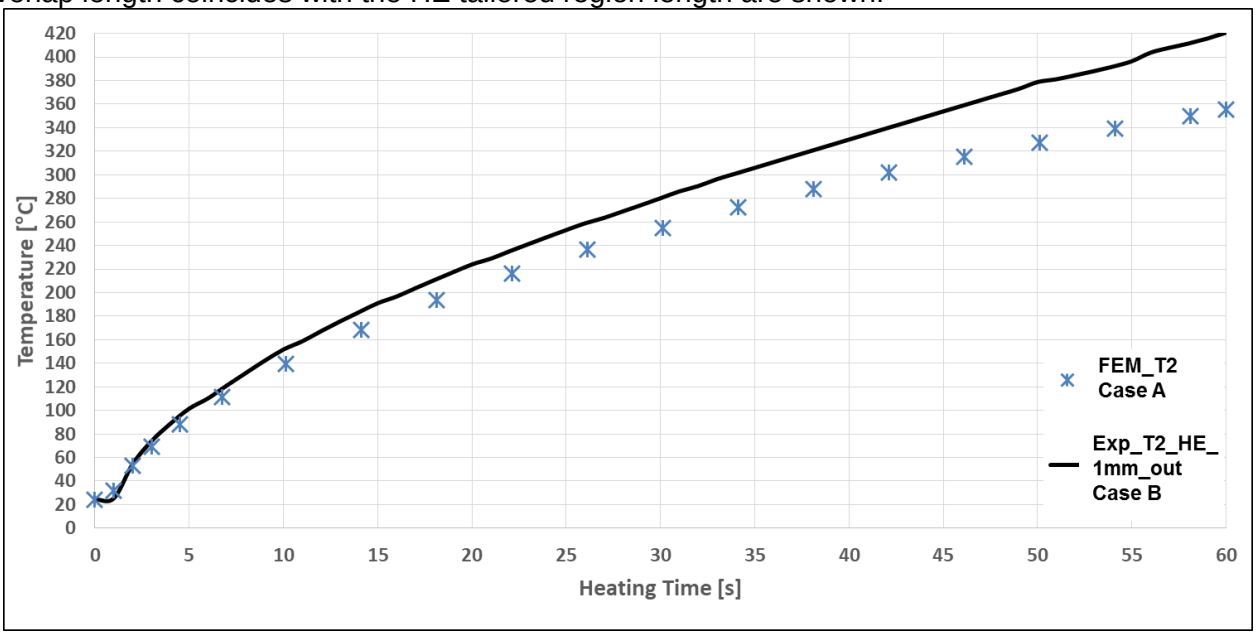

Figure 3.3-11: Effect of relative position between HE tailored region and adherend edge on the transversal edge temperature in the case of Concept_2 HE.

It can be seen that the measured temperatures are much higher than 420 °C instead of expected 360 °C. The explanation is that the steady state temperature of the region designed to be inside the welding stack is higher when it is exposed to the air than the temperature of the region out of the welding stack. Consequently it will heat-up the transversal edge of the welding interface.
It is important to mention that sensitivity of the transversal edge temperature as a function of the HE positioning within the welding stack is increasing with the IPS increase of the region inside the welding stack. Because this issue was noticed only in the case of welding with Concept_1_1 and Concept_2 HE where IPS of the heating element region inside the welding stack is high: $71.4\ \frac{kW}{m^2}$, compared to $51.4\ \frac{kW}{m^2}$ in the case of Concept_1_0 HE.

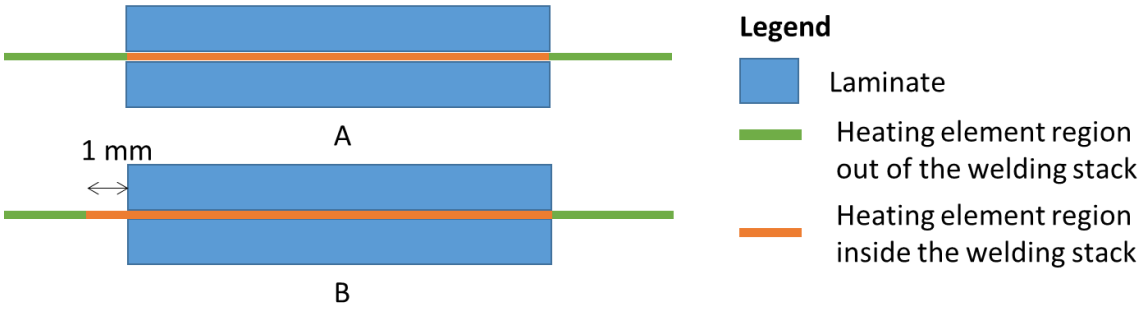

Figure 3.3-12: Schematic view of the relative position between the HE region designed to be inside the welding stack and adherend edges. Ideal case (A) 0mm mismatch, non-ideal case (B) designed region to be inside the welding stack is longer by 1mm at one edge of the welding stack

4. RESULTS AND DISCUSSION

4.1 HEATING ELEMENTS MANUFACTURING ISSUES AND MANUFACTURING DEVIATION EFFECT ON THE WELDING INTERFACE TEMPERATURE

The first trials to manufacture the HE were done by cutting them to the right width dimension of 25.4 mm. This method was unsuccessful since the HE element paths in the region inside the welding stack along the longitudinal edges were distorted due to the high temperature generated by the laser during the cutting process and low stiffness of the part along the longitudinal edge (Figure 4.1-1 left). This effect led to a situation when longitudinal paths were missing or were too wide or their width was not constant along the HE length. To solve this problem the HE were designed with a wide strip along the longitudinal edge to increase their stiffness in order to avoid distortion during the cutting process (Figure 4.1-1right). The drawback of this solution is that it involves manual cutting of the HE to the required width size of 25.4 mm.

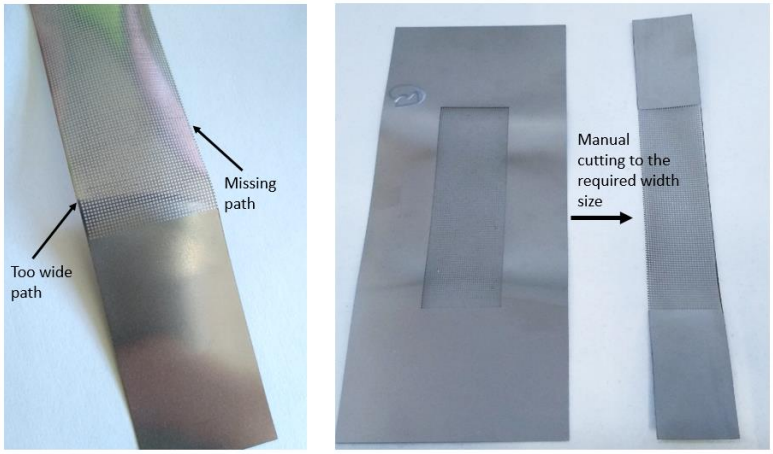

Figure 4.1-1 Concept_1 manufacture issues first trial vs second trial

Another limitation of the manufacturing process is the minimum width of the path. Paths with the width smaller than 0.2 mm could not be cut.
The measurements of the HE paths width using the digital microscope showed deviation of ±5% from the value specified in the HE design drawing. To check if these deviations have an impact on the temperature at the welding interface six joints were welded using different HE types Concept_1_0: Type A01, B01, C01, A005, B005, and C005. All joints were welded under identic conditions: IPS input of $51\,\frac{kW}{m^2}$ and welding time of 140 s, for that a current input of 39 A was applied for 0.1 mm thick plates and 27.6 A for 0.05 mm thick plates. The temperatures were measured at the welding interface in the centre (T1), 3 mm from the transversal edge (T2,T4), and 3 mm from the longitudinal edge (T3). The TC position is showed in Figure: 4.1-2. TC were fixed to the laminates and insulated from the HE using the Kapton tape. The experimental measurements are presented in the following pictures: Figure 4.1-3, Figure 4.1-4, Figure 4.1-5.

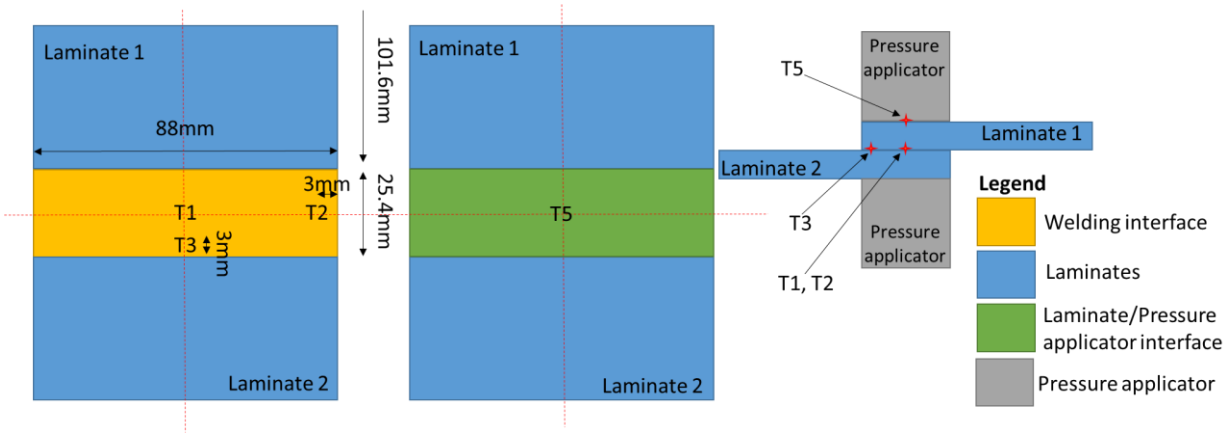

Figure: 4.1-2:TC position during experimental measurements

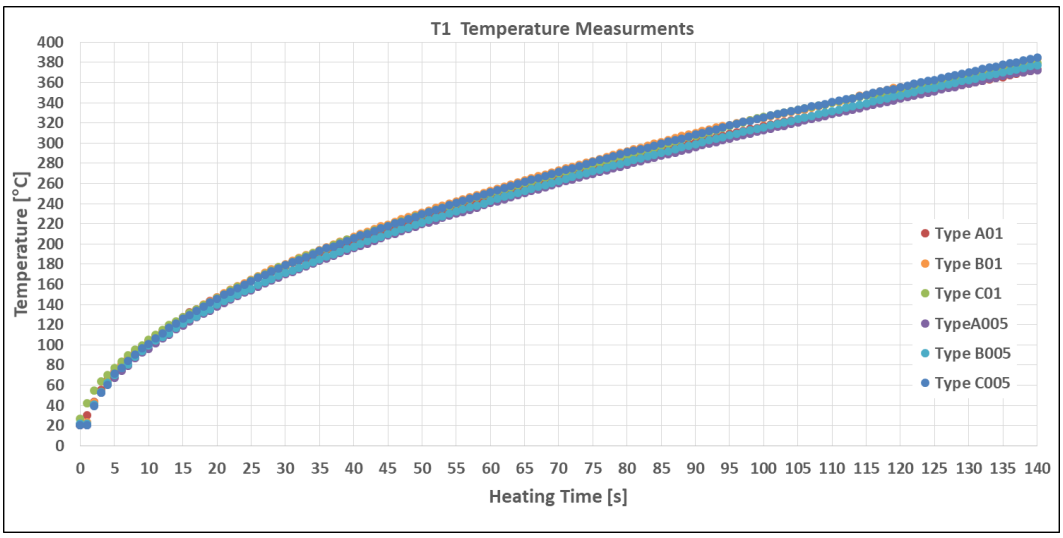

Figure 4.1-3: Measured temperature at T1 position for joints welded with Concept_1_0 heating elements

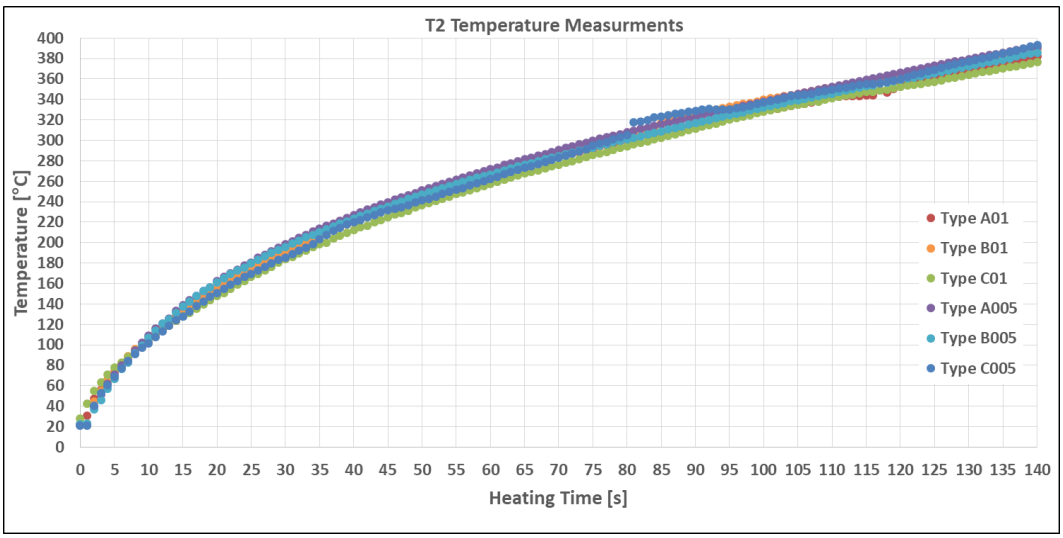

Figure 4.1-4: Measured temperature at T2 position for joints welded with Concept_1_0 heating elements

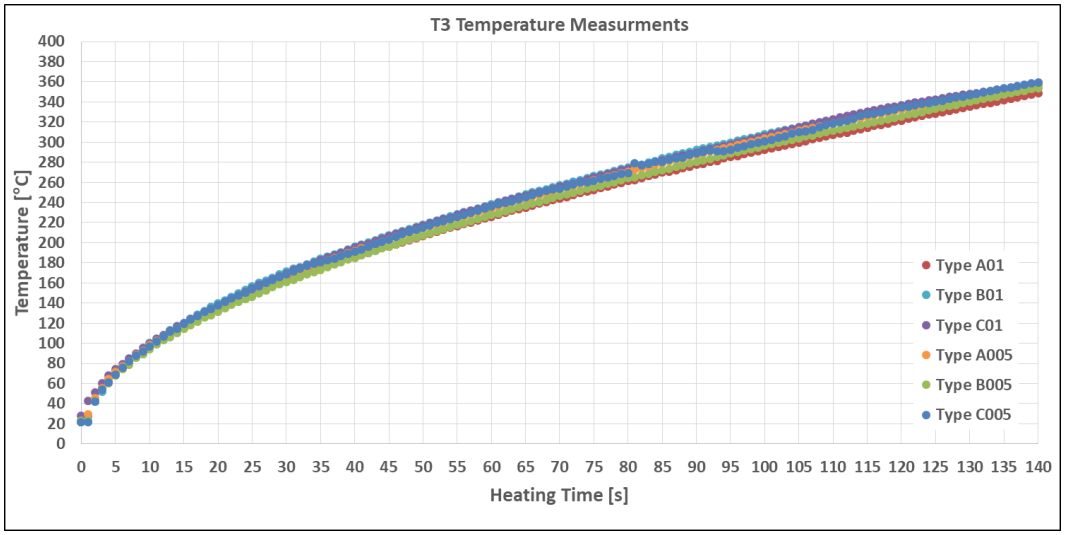

Figure 4.1-5: Measured temperature at T3 position for joints welded with Concept_1_0 heating elements

The average values of tested HE at the welding process end are: 378.4 °C at T1 position, 386.5 °C at T2 position and 355 °C at T3 position, with the sample standard deviation of 5.3°C, 6.3°C and 4°C, for T1, T2 and respectively T3 position. These standard deviation values prove that deviations from the nominal design during manufacturing process do not have a big impact on the temperature distribution. Moreover the error does not come only from the HE manufacturing tolerances but also from others sources such as: the adhered thickness tolerances, positioning tolerances, etc.

4.2 EFFECT OF THE GLASS INSULATION MATERIAL ON LAP SHEAR STRENGTH

As it was discussed in the literature study, the electrical insulation of the HE in the case of carbon fibre reinforced laminates welding is essential in order to avoid current leakage. From all solutions found in the literature study, electrical insulation of the HE by sandwiching it between two layers of glass fabric was chosen, because this method is cheap and efficient against current leakage. The drawback of this method is insertion of an additional material at the welding interface; this definitely will have an impact on LSS because the bond line thickness will be increased leading to a higher peel stress. Furthermore the bonding strength between glass fibres and thermoplastic resins is weak. Consequently a new weak interface (glass layer/ resin) will be added on top of an already existing one (metal/resin).
At CTC GmbH three types of PEKK prepregs fabrics were available.

1. **Barrday TF0300-48-G108 PW-50-38.00-2S**
2. **Toray GK 1080 127 60 120 Cetex TC1322.**
3. **Porcher E glass/PEKK 4H Satin 157g/sqm**

Table 4.2-1 Glass fabrics characteristics

Glass prepreg type	Thickness [mm]	Weave Type	GF Sizing	Gap size [mm]	Fibre bundle width [mm]	OAR
Barrday	0.20mm	Plain	NO	0.28	0.22	0.4
Toray	0.21mm	Plain	YES	0.28	0.24	0.32
Porcher	0.21mm	4HS	YES	0.1	0.27	0.12

According to the glass fabric manufacturers, the glass fabrics provided by Toray and Porcher received a treatment towards increasing the bonding strength between the fibres and PEKK resin. Unfortunately, the manufacturers did not specify the exact treatment type. The glass fabric from Barrday did not receive any treatment.
For this project it was decided to use the one which provides the highest LSS. For this, joints were welded testing each type of fabric using M200 mesh and Concept_1_0 HE under identic welding

parameters: 140 s welding time and 51 $\frac{kW}{m^2}$ IPS. Since the effect of the glass fabric layer on the welded joint LSS is not the main aim of this thesis and because HE manufacturing and the LSS tests are expensive it was decided to weld only one joint for each combination glass fabric/HE (6 joints in total). To eliminate the longitudinal temperature gradient effect on LSS especially in the case of the joint welded with M200 mesh, the test specimens were cut from the middle of the welded joints (position 2 in Figure 3.1-3). The LSS results are presented in Figure 4.2-1.

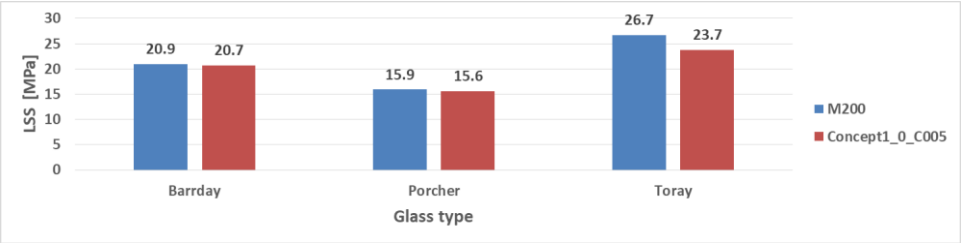

Figure 4.2-1: Joints LSS in function of the glass fabric type used as electrical insulator.

It can be seen that specimens welded with Toray glass fabric provided the higher LSS than specimens welded using Barrday glass fabric (27.7% higher for M200 mesh HE, 14.5% higher for Concept_1_0_C005 HE). From Table 4.2-1**Error! Reference source not found.** it can be seen that both fabrics are similar, the major difference is that Toray glass fabric was treated for a better glass/matrix adhesion. Therefore the glass fibre treatment has a beneficial effect on joint LSS, this is in agreement with Shi [25] observations. Despite the fact that Porcher glass fabric was treated as well, it provided lower LSS than the untreated Barrday glass fabric; 23.9% for M200 mesh and 24.6% for Concept_1_0_C005 HE. The reason is that the OAR of the Porcher glass fabric is very low, thus it seems that the glass fabric acts as a separation wall between the resin bonded to the HE and the resin bonded to the adherend. The bonding strength between PEKK and glass fibres is lower than the bonding strength between two layers of neat resin, were bonding strength relies on molecular entanglement. From the data presented in Figure 4.2-1 it seems that the OAR of the glass fabric has a higher impact on LSS than the glass fibre treatment. However this is not a general valid conclusion, because the fibre treatment type and its effect on LSS are unknown.
In the figures below the failure surface of the tested joints are presented.

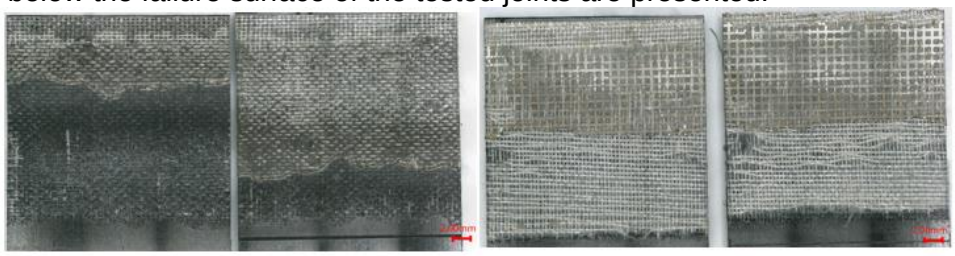

Figure 4.2-2: Failure surface of a joint welded with Barrday glass fabric used as a HE electrical insulator. M200 mesh HE(left), Concept_1_0_C005 HE (right).

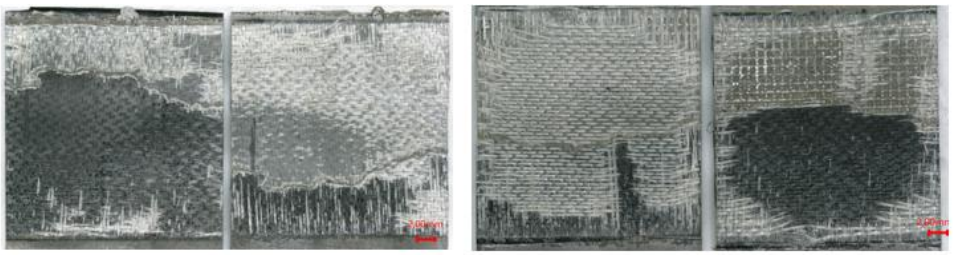

Figure 4.2-3: Failure surface of a joint welded with Porsher glass fabric used as a HE electrical insulator. M200 mesh HE(left), Concept_1_0_C005 HE (right).

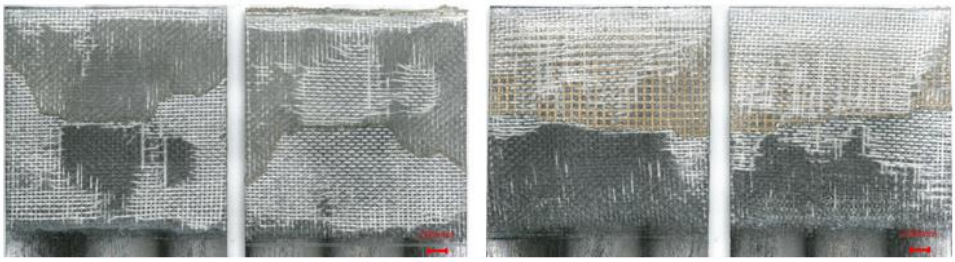

Figure 4.2-4: Failure surface of a joint welded with Toray glass fabric used as a HE electrical insulator. M200 mesh HE(left), Concept_1_0_C005 HE (right).

In all cases poor adhesion of resin to the glass was noticed. The glass fibres seem to be dry, even in the case of treated glass fabrics like the products from Porcher and Toray. Another general remark is that all joints failed with the rupture of the glass fabric layer and with the rupture of the HE in the middle of the overlap, that coincides with the rotational centre during the LSS test due to the joint eccentricity. The joint welded using the Barrday glass fabric with M200 HE showed a better boding between the HE and the glass fabric than between glass fabric and the adherend. As it can be seen from the Figure 4.2-2(left), the glass layer is attached only to the HE while the adherend surface is free from glass fabric. While in the case of laser cut HE Figure 4.2-2(right) a better bonding is noticed between the adherend and the glass fabric since the glass layer is mainly attached to the adherend. A better bonding between glass layer and HE in the case of M200 mesh is explained by the fact that a better mechanical interlocking was achieved between the glass fabric layer and M200 mesh than between the Concept_1_0_C005 HE and the glass layer. The evidence is presented in Figure 4.2-5 where it can be seen that glass fibres penetrate into the M200 HE, while in the case of Concept_1_0_C005 HE it is a clear interface between the glass fabric layer and the HE. The fibres penetrate into the M200 mesh because its surface is wavy and the glass fabric follows the mesh surface. While in the case of Concept_1_0_C005 the HE surface is completely flat.

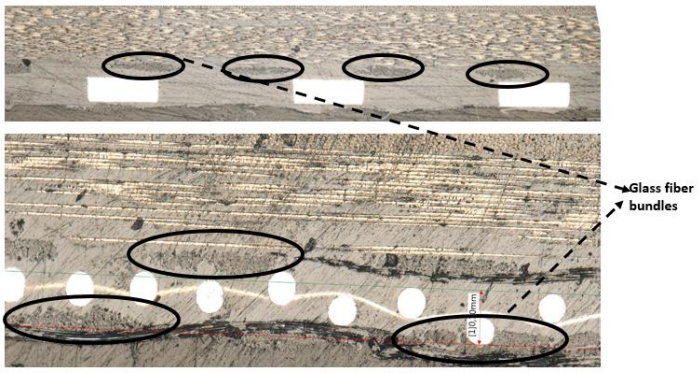

Figure 4.2-5: Barrday Glass fibres on Concept_1_0_C005 HE (Top), : Barrday Glass fibres on M200 HE(Bottom)

However for Toray glass in the case of the joint welded with M200 HE judging by the amount of glass fabric attached to the HE and to the adherend presented in Figure 4.2-4, it seems that the bonding strength between the glass fabric and the adherend is equal or even higher than the bonding strength between the glass fabric and the HE. The explanation is presented in Figure 4.2-6, the glass fabric layer did not penetrate into the M200 mesh HE as it happened in the case of the Barrday glass fabric. The reason is that in the case of Barrday glass fabric the M200 mesh HE was consolidated together with the glass fabric by using a hot press while in the case of Toray glass the HE was consolidated using the welding machine pressure applicator pistons.

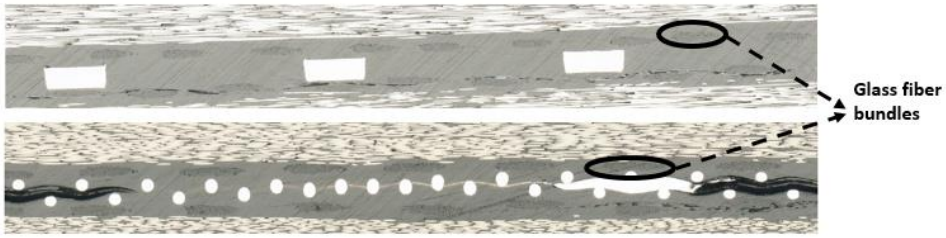

Figure 4.2-6: Toray Glass fibers on Concept_1_0_C005 HE (Top), : Barrday Glass fibers on M200 HE(Bottom)

Based on the LSS results reported in this section, Toray glass fabric will be used for further investigations in this thesis.

4.3 EFFECT OF THE LINEAR WIRE DENSITY ON LAP SHEAR STRENGTH

The effect of linear wire density effect on LSS was studied by welding joints with three different types of Concept_1_0 heating elements: A005, B005, C005. All HE have identic electrical resistance pattern, thus under an identic current input and BC should provide the same temperature distribution at the welding interface. The main difference between them as it can be seen from Table 3.2-1 is the linear wire density value. Therefore the LSS will depend only on the linear wire density of the mesh, while thickness and OAR is identic for all three HE. Five joints were welded for each tested HE type and from each joint three specimens were cut: two from the edges and one from the centre as it is shown in Figure 3.1-3.

4.3.1 Temperature Distribution

Used welding parameters were: IPS of $51\ \frac{kW}{m^2}$ with a current input of 27.6 A and 140 s welding time. The temperature distribution achieved at the welding interface under these parameters predicted by the validated FEM model is presented in Figure 4.3-1 and Figure 4.3-2. As it can be seen from the Figure 4.3-1 the temperature in the centre of the welding interface is 380 °C, 40 °C higher than the PEKK melting temperature, this decision was made in order to bring the welding interface region close to the longitudinal edges above PEKK melting temperature.

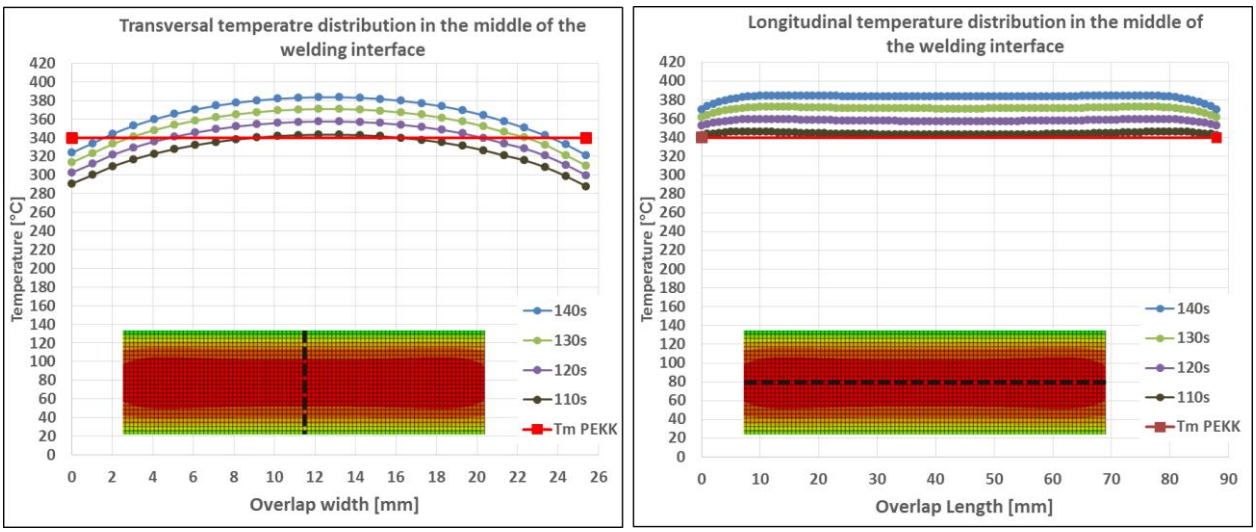

Figure 4.3-1. FEM predicted longitudinal temperature distribution (right) and transversal temperature distribution (left) for a joint welded with Concept_1_0 HE with IPS of $51\ \frac{kW}{m^2}$ *and welding time of 110 s. 120 s, 130 s. 140 s.*

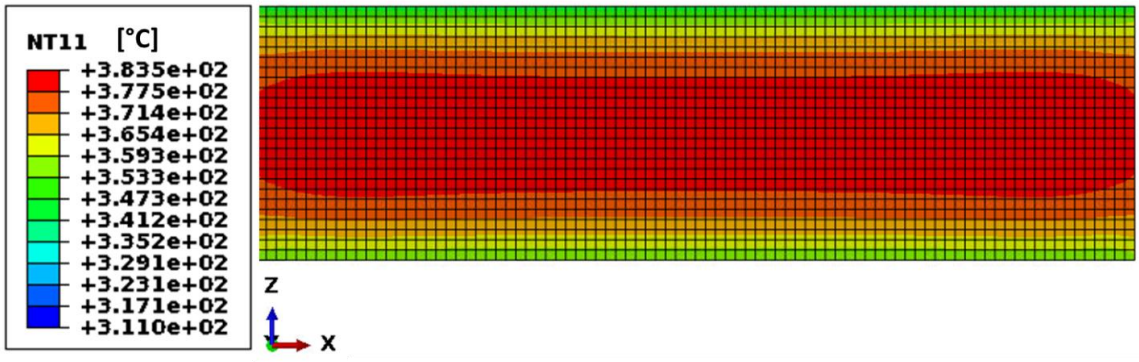

Figure 4.3-2 FEM predicted temperature at the welding interface for a joint welded with Concept_1_0 HE with IPS of $51\,\frac{kW}{m^2}$ *and 140 s welding time*

4.3.2 LSS Results of Linear Wire density Study.

In Figure 4.3-3 the LSS results are provided. At the first glance it looks that LSS tends to increase with the decrease of LWD, in the case of specimen cut from the Position 2 and Position 3 of the joint (Figure 3.1-3). However the difference in LSS increase due to lower LWD is in the range of one standard deviation, therefore a clear conclusion regarding the effect of LWD on joint LSS cannot be drawn. Perhaps the LWD range chosen for this to study was too narrow.

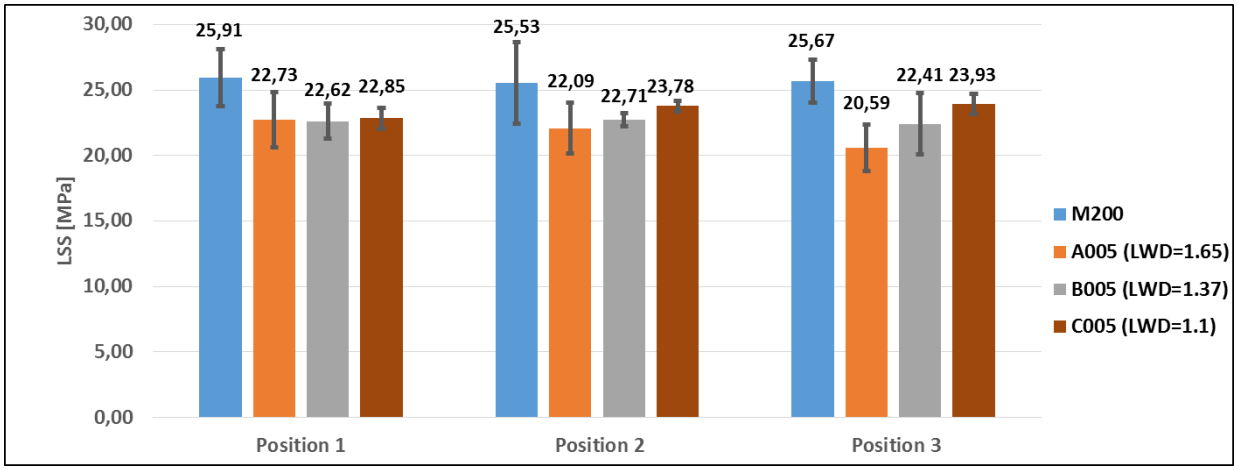

Figure 4.3-3: LWD study LSS results

4.3.3 Fractography, Macroscopic Failure Features

A common fracture surface characteristic of all tested specimens is that approximately 50% of the HE was attached to each side of the fracture surfaces. This proves that failure initiated at both overlap ends simultaneously and propagated towards the centre of the overlap ending wth the HE tear. Another common feature is that it seems that GF are mostly dry and that is a sign that PEKK/GF adhesion is weak. Further the failure mode can be divided into two modes: **Type I** mode with entire glass fabric layer attached to the HE and **Type II** mode where between 30%-70% of glass fabric was attached to the adherend. The macroscopic views of the tested joints failure surface are shown below.

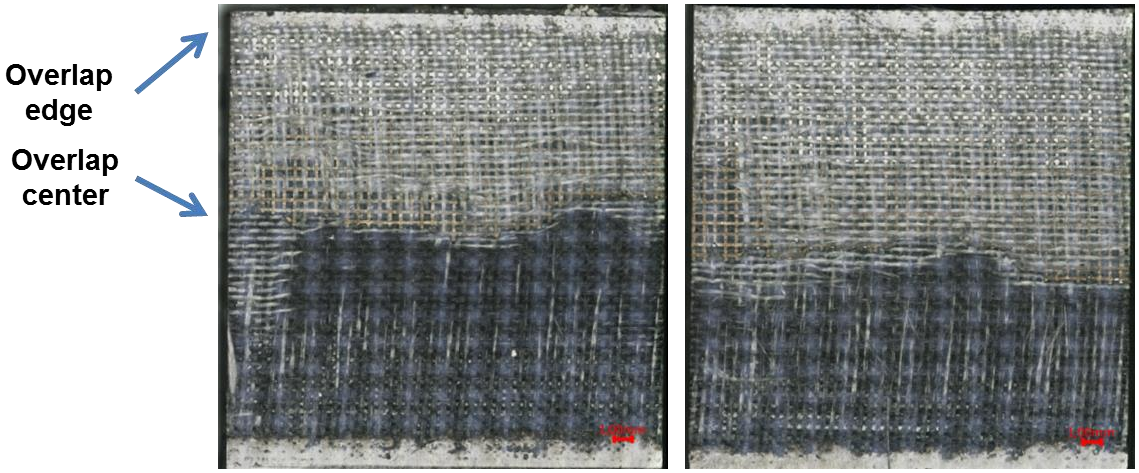

Figure: A005 HE two mating failure surface of the same joint macroscopic view

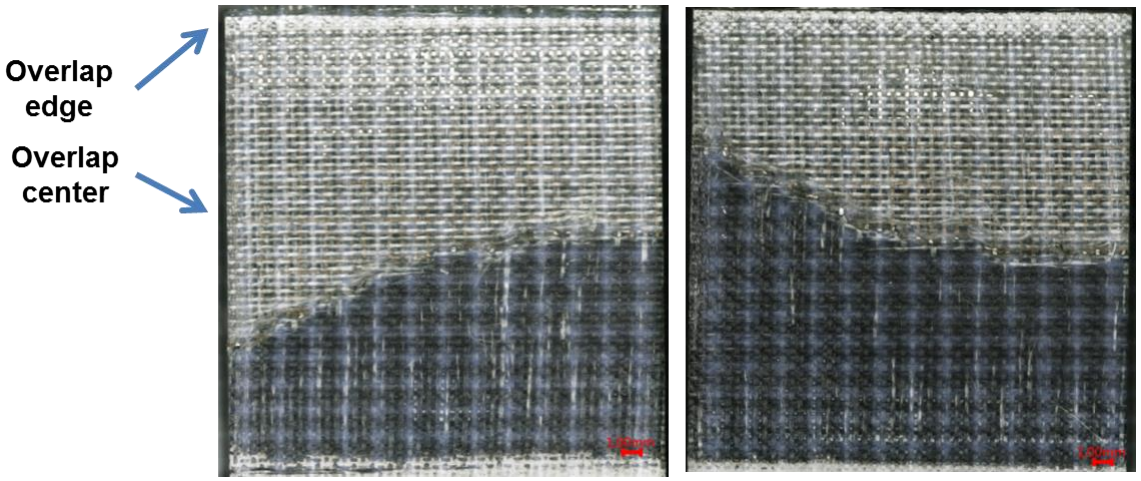

Figure 4.3-4: B005 HE two mating failure surface of the same joint macroscopic view

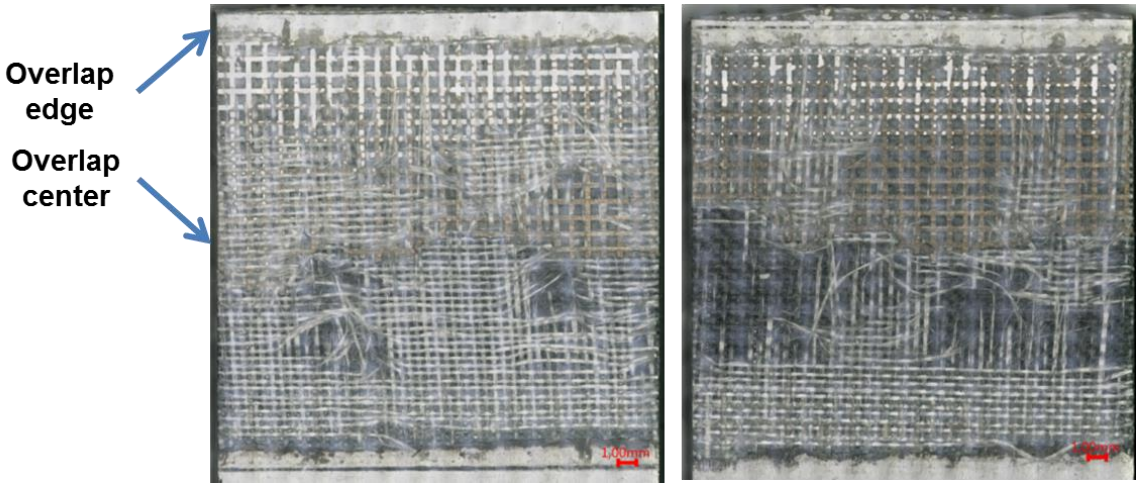

Figure 4.3-5: C005 HE two mating failure surface of the same joint macroscopic view

A common feature between Type I and Type II failure mode is that it seems no resin was attached to the HE at the overlap edge, while towards to the overlap centre the resin was bonded to the HE. This observation is depicted in Figure 4.3-6, where HE wires close to the overlap edge are shiny, a sign that they are resin free. A possible explanation could be high peel stresses at the overlap end as it is presented in Figure 2.3-1. The bonding between metal surface and resin is weak, thus under high peel stresses normal to the HE surface the resin will detach. While towards the centre of the overlap the failure mode is dominated by the shear stress and failure path will change from HE/glass fabric interface to the glass fabric/adherend interface. In the case of adhesive bonded

joints the shear stress across the bondline thickness is highest at the interface between bondline and adherend [36]. Thus it seems that the most loaded interface in shear is the glass fabric/adherenend interface. It looks like half of the failure surface close to the adhered end is dominated by the peel stresses while the second half is dominated by the shear stresses.

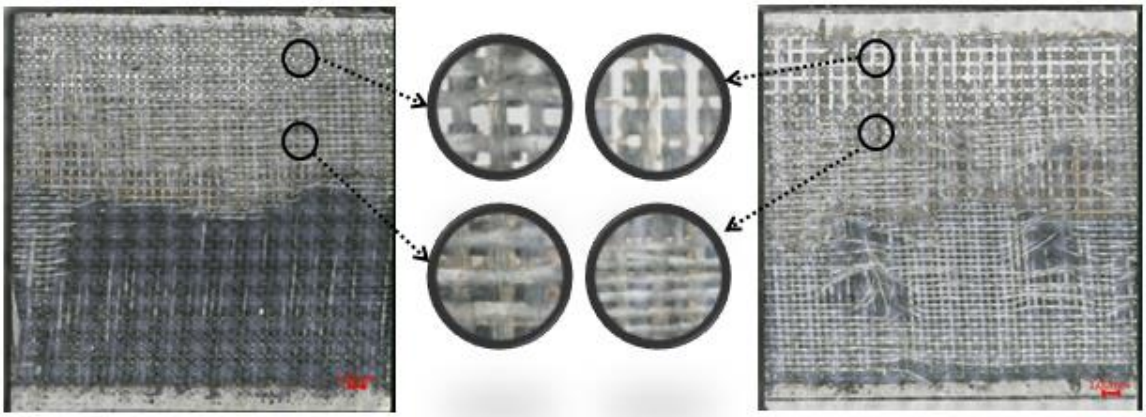

Figure 4.3-6: Type I failure surface (left),Type II failure surface (right)

It is interesting to notice that all joints welded using A005 and B005 HE failed under Type I mode and joints welded with C005 HE failed under Type II mode. The explanation of the different failure modes between A005 HE and C005 HE might be the relative size between HE wire width and glass fabric gap size. The mechanism is the following: in the case of C005 HE the wire width is higher than the gap size of the glass fabric (0.3mm vs 0.28mm). Thus the resin contained by the glass fabric gap will be bonded to the HE wire only. In the case of A005 HE the wire width is lower than the glass fabric gap(0.2mm vs 0.28mm), consequently a part of the resin contained by the glass fabric gap will bonded to the HE wire while the rest of the resin will fusion with the resin from the opposite side of the HE creating a stronger bonding between glass fabric layer and HE against high peel stresses at the overlap edge.(In Figure 4.3-7 the relative size between HE wire width and glass fabric gap size or A005 and C005 HE is presented). Thus in the case of A005 HE where the bonding between glass layer and HE is stronger due to a smaller relative size between HE wire and glass fabric gap size. The failure will initiate between the glass fabric layer and adherend. While in the case of C005 HE where bonding between glass fabric layer and HE is weaker the failure will start between glass fabric and the HE. Close to the overlap centre the failure mode will be dominated by the shear stresses and the failure path will continue between glass fabric layer and adherend.

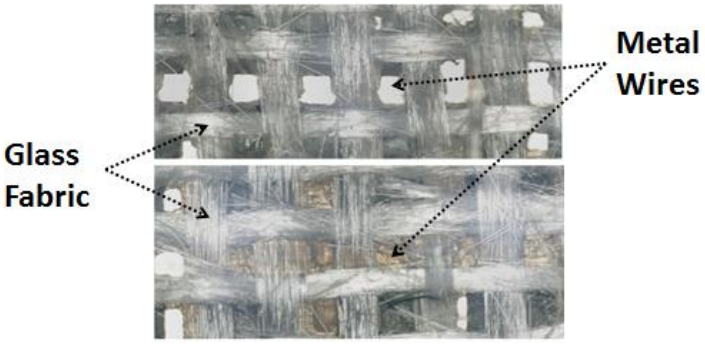

Figure 4.3-7: A005 wire size compared to glass fabric gap size (Top), C005 wire size compared to glass fabric gap size (Bottom)

But different failure modes did not change the LSS of the joints. Nevertheless a stronger bonding between HE and glass fabric should have a beneficial effect on the joint strength. With this it seems that an important HE design criterion is dependent on the glass fabric gap size and namely: the HE wire width should be smaller than the gap size of the glass fabric used as an electrical insulation.

4.4 EFFECT OF THE OPEN AREA RATIO ON LAP SHEAR STRENGTH

The effect of HE OAR on LSS was studied by testing joints welded using three different types of Concept_1_1 HE type: C1, C2 and C3. The properties of the HE are presented in Table 3.2-2 and the main difference between them is the OAR value: 0.5, 0.6 and respectively 0.7. All tested HE have identic electrical resistance pattern thus under equal current input and BC they will provide the same temperature distribution at the welding interface. Five joints were welded by using each HE type. From each joint there specimens were cut as it is specified in Figure 3.1-3.

4.4.1 Temperature Distribution

Welding parameters applied were: IPS of 71.4 $\frac{kW}{m^2}$ generated by a 39 A current intensity, 75 s welding time. The welding parameters are different compared to the welding parameters used in the previous study, because the resistance pattern of the HE used in this study is different than the electrical resistance pattern of the HE used in the LWD study. However as it can be seen from Figure 4.4-1 and Figure 4.4-2, even if the welding parameters are different the same temperature distribution was achieved at the end of the welding process as in the case of LWD study discussed in the previous section.

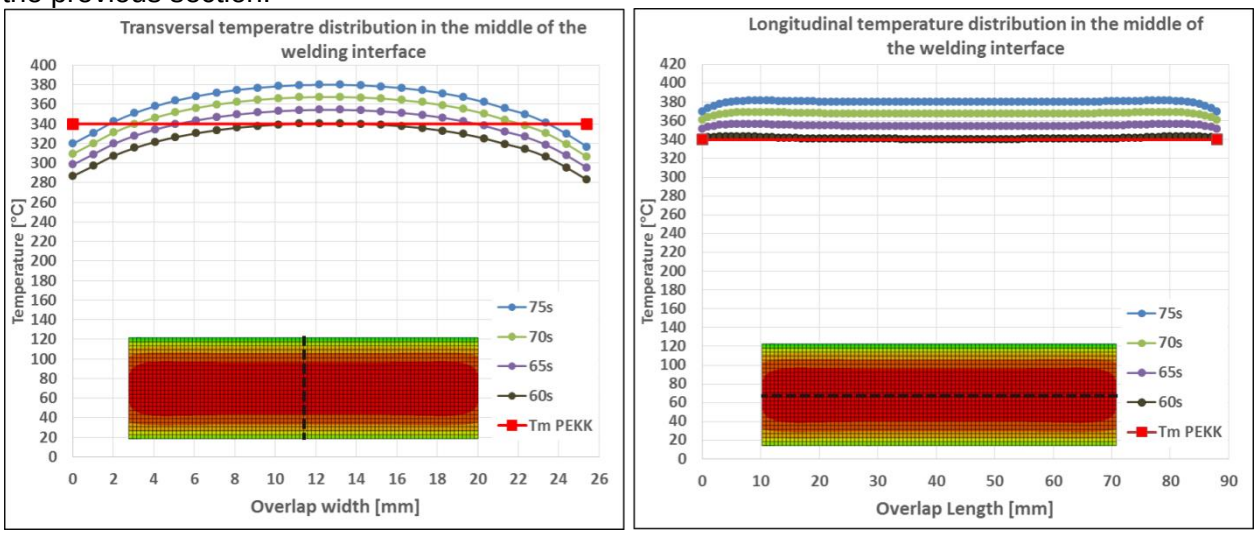

Figure 4.4-1 FEM predicted longitudinal temperature distribution (right) and transversal temperature distribution (left) for a joint welded with Concept_1_1 HE with IPS of 71.4 $\frac{kW}{m^2}$ and welding time of 75 s. 70 s, 65 s. 60 s.

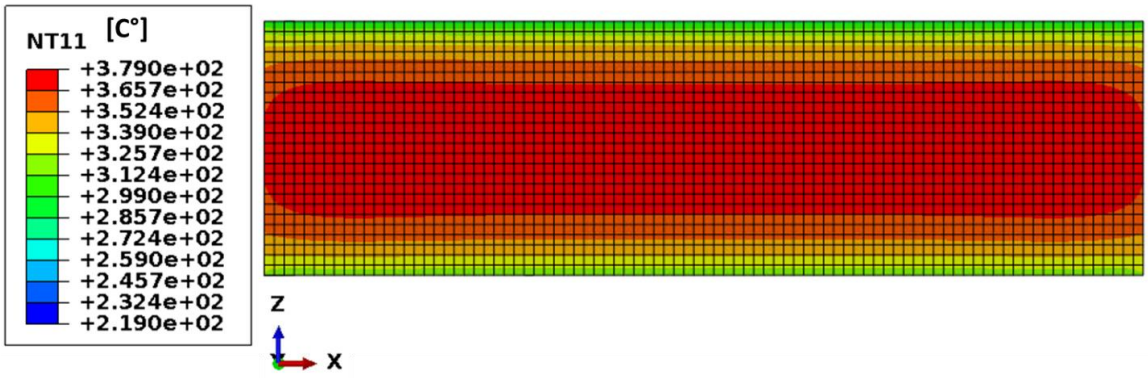

Figure 4.4-2: FEM predicted temperature at the welding interface for a joint welded with Concept_1_1 HE with IPS of 71.4 $\frac{kW}{m^2}$ and 75 s welding time

4.4.2 LSS results

The LSS results for this study are shown in Figure 4.4-3. As it was expected the LSS is increasing with increase of the OAR. The most obvious explanation is that by increasing the OAR, the area of the weak metal/resin interface is reduced, thus more resin from the adherends will have a direct contact without having metal as an intermediary interface. The LSS difference between the specimens welded with type C3 and type C1 HE is out of one standard deviation range, and this trend is independent of the position from where specimens were cut. Therefore it can be concluded that OAR increase has a beneficial effect on joint LSS.

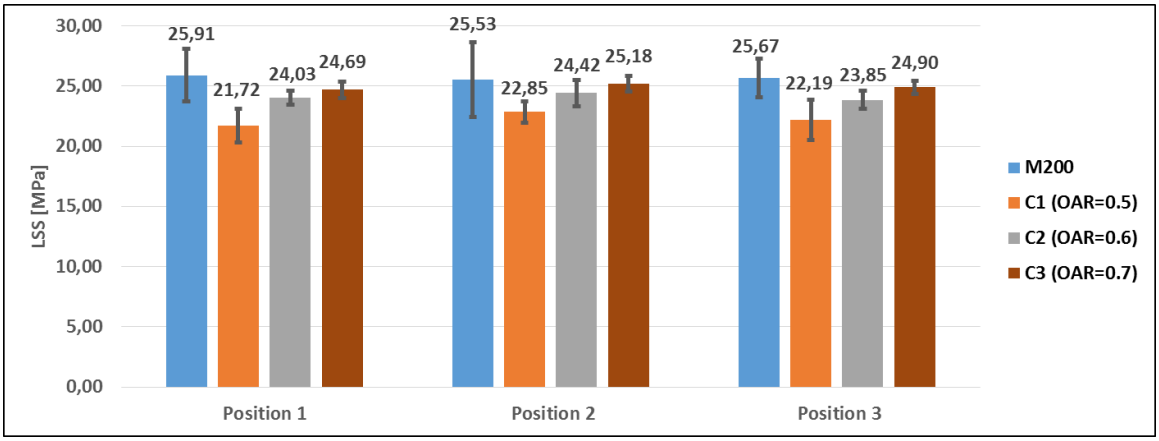

Figure 4.4-3: OAR study LSS results

4.4.3 Fractography, Macroscopic Failure Features

The failure surfaces of the joints welded with Concept_1_1 type C1, C3 and C3 are shown in the Figure 4.4-4 and Figure 4.4-5. It can be noticed that the failure surfaces show the same patterns as in the case of Concept_1_0 type C005 HE (Type II failure). The common feature between Concept_1_0 Type C005 HE and Concept_1_1 HE is that in all cases the wire width is 0.3 mm. Thus the explanation given in the previous section that relative size between glass fabric gap and HE wire width may trigger different failure modes is reinforced.

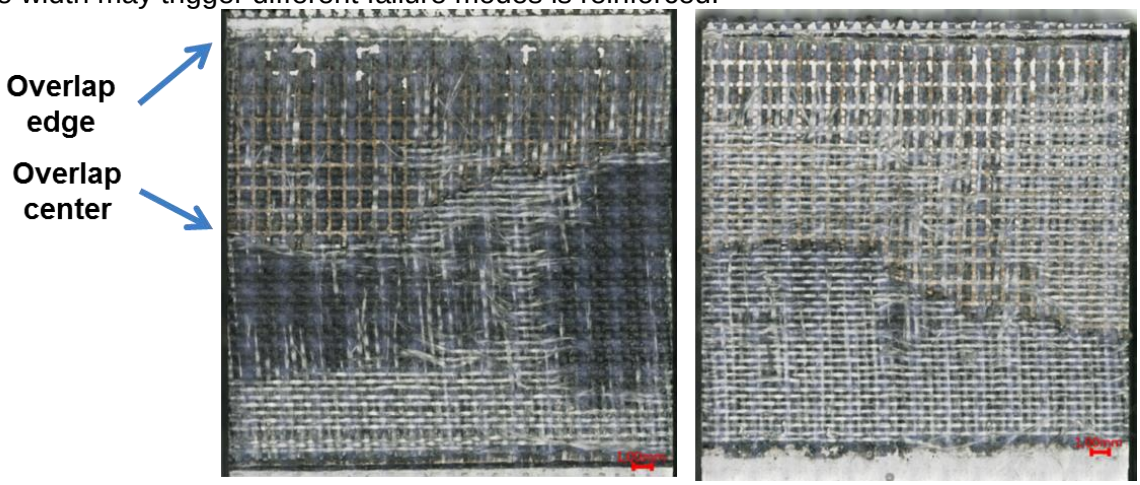

Figure 4.4-4 C1 HE two mating failure surface of the same joint macroscopic view

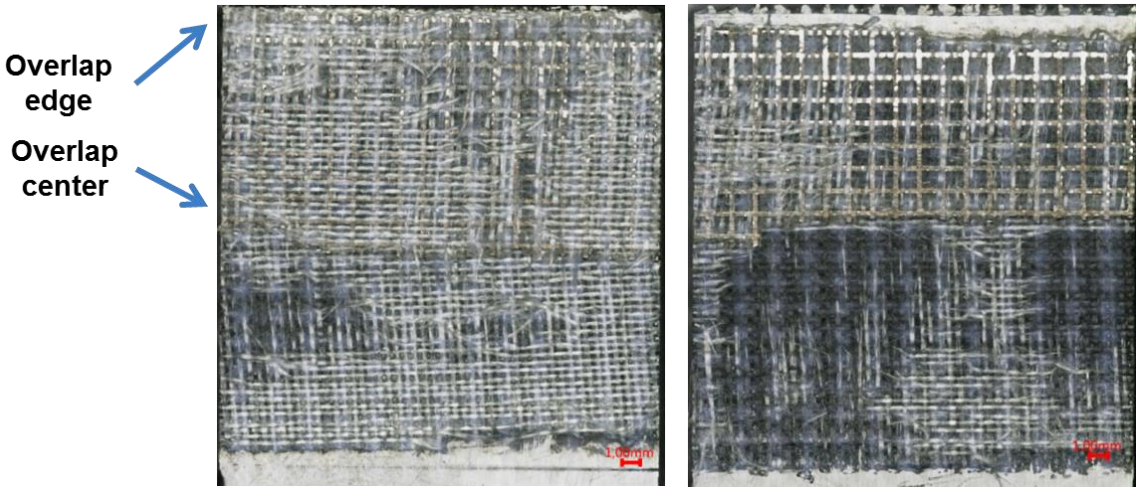

Figure 4.4-5: C2 HE two mating failure surface of the same joint macroscopic view

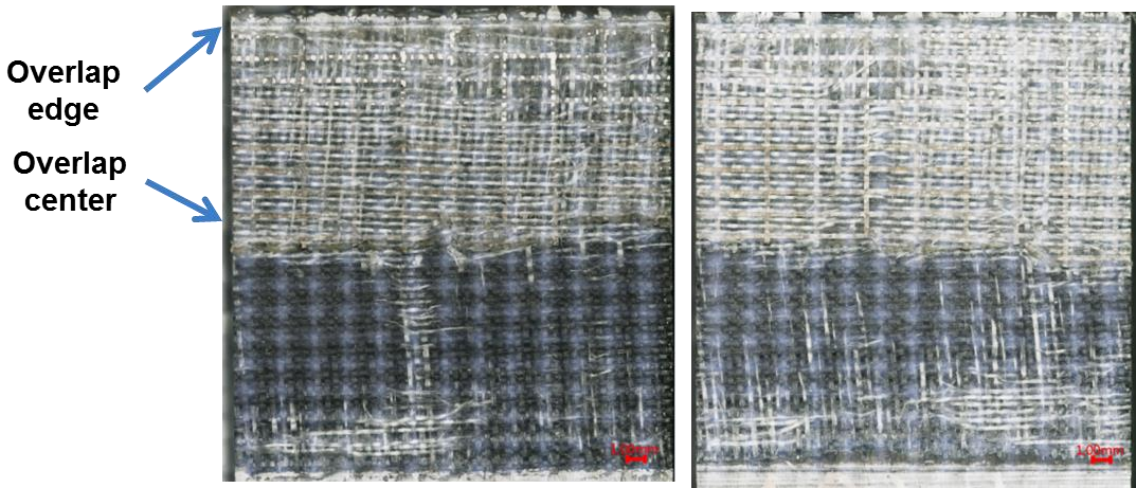

Figure 4.4-6 C3 HE two mating failure surface of the same joint macroscopic view

An interesting trend which can be depicted from Figure 4.4-4 and Figure 4.4-5 is that with the increase of OAR the amount of glass fabric attached to the HE is increasing as well. This is a clear indicator that increasing OAR leads to a better bonding between HE and glass fabric through two mechanisms. First, by increasing OAR the surface of weak metal/resin interface will be decreased. Second, because with the increase of OAR the HE gap size was also increased, in the case of type C3 the gap size of HE is considerable bigger than the width of the glass fabric bundles. Thus some glass fabric threads penetrated into the HE gap, boosting mechanical interlocking between these two. From Figure 4.4-7 it is visible that in the case of C3 HE some of the glass bundles sink into the HE gap, while in the case of A005 HE the size of the HE gap is too small to allow that, and the glass fibres bundles just lay on the HE surface.

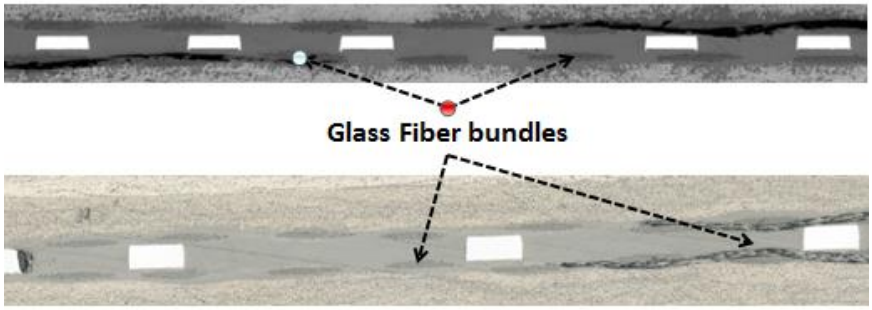

Figure 4.4-7 Bond line transversal microscopic cut view of a joint welded with A005 HE (top) and C3 (bottom)

4.5 EFFECT OF THE UNIFORM TEMPERATURE DISTRIBUTION ON LAP SHEAR STRENGTH

The uniform temperature distribution was achieved by using Cocept_2 HE. To assess its effects on LSS five joints were welded using this HE type. The geometrical properties of the Concept_2 HE are presented in Table 3.2-3

4.5.1 Temperature Distribution

Welding parameters applied were: IPS of 71.4 $\frac{kW}{m^2}$ in the centre of the overlap and 110.4 $\frac{\mathrm{kW}}{\mathrm{m}^2}$ 2 mm in the proximity of the longitudinal edges generated by a 39 A current intensity, 60 s welding time. As it can be seen from the pictures below compared to the Concept_1 HE element in this case uniform temperature distribution was achieved over the whole surface of the welding interface Figure 4.5-1 and Figure 4.5-2. Because the transversal temperature gradients were eliminated, the process temperature at the welding interface centre decreased to 360 °C. This led to the welding time decrease to 60 s instead of 75 s as it is in the case of Concept_1_1.

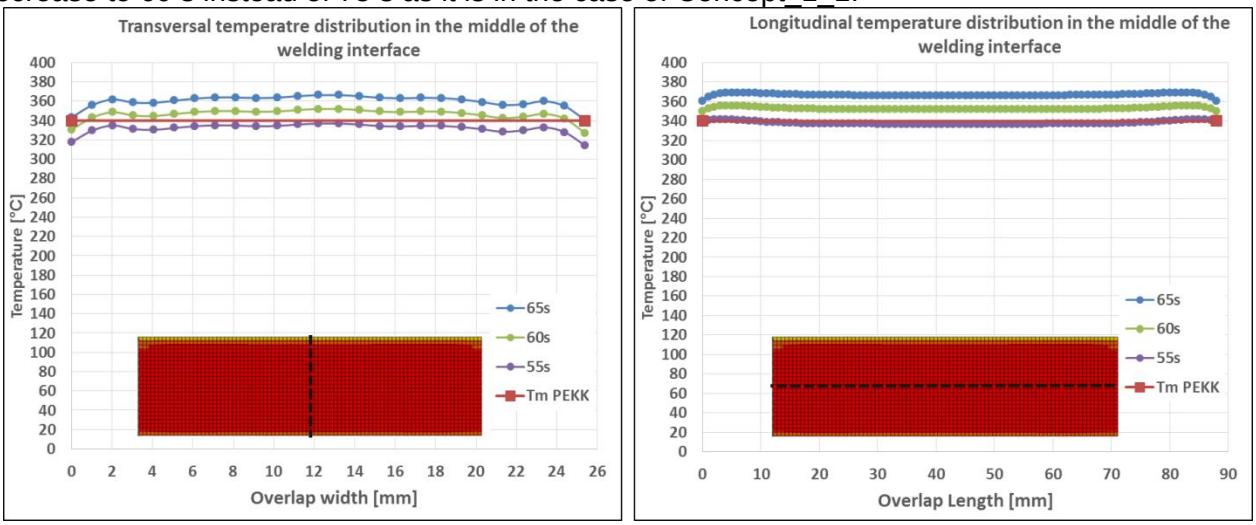

Figure 4.5-1 FEM predicted longitudinal temperature distribution (right) and transversal temperature distribution (left) for a joint welded with Concept_2 HE with IPS in the middle of welding interface of 71.4 $\frac{kW}{m^2}$ *and* 110.4 $\frac{kW}{m^2}$ *in the region 2 mm from the longitudinal for a welding time of 75 s. 70 s, 65 s. 60 s.*

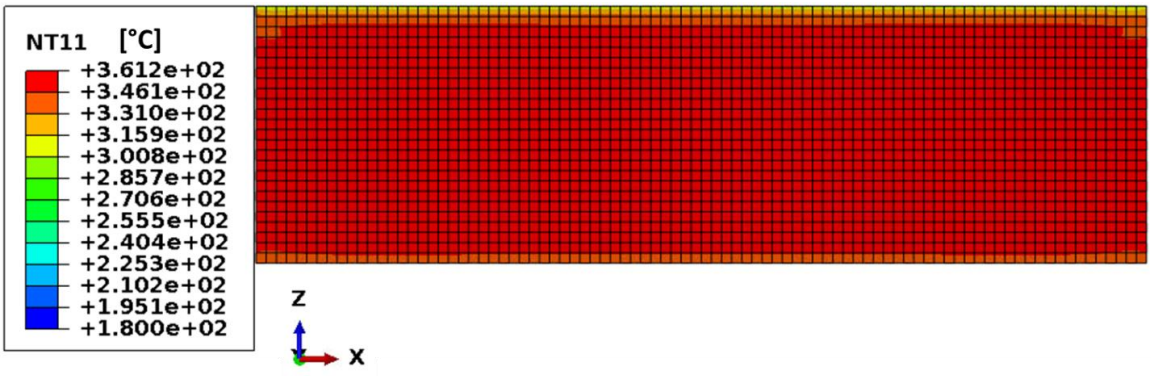

Figure 4.5-2 FEM predicted temperature at the welding interface for a joint welded with Concept_2 HE IPS in the middle of welding interface of 71.4 $\frac{kW}{m^2}$ *and* 110.4 $\frac{kW}{m^2}$ *in the region 2 mm from the longitudinal edge for a welding time of 62 s*

The predicted temperature uniformity by the FEM model depicted in Figure 4.5-2 was confirmed by the deep marks left by the glass fabric threads on the surface of the welded adherend Figure 4.5-3. Deep marks on the welded adherend surface shows that the surface was above the resin melting

temperature. The fact that overlap width coincides with the marks left by glass fabric proves that the entire overlap surface of the adherend was above resin melting temperature. Finally low degree of fibre movement at the adherend transversal edge proves that the adherend surface was exposed to the temperatures higher than PEKK resin melting point for a short amount of time (5s according to the data from Figure 4.5-1).

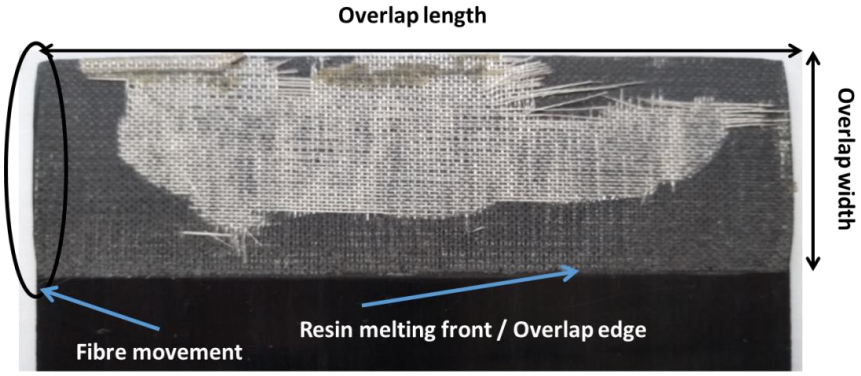

Figure 4.5-3: Marks left by the glass fabric on the welded surface of one adherend welding interface.

4.5.2 LSS results

The LSS results provided by the specimens welded with Concept_2 HE along with the LSS results provided by the specimens welded with M200 mesh and Concept_1_1 type C2 and type C3 HE are presented inFigure 4.5-4: Concept_2 LSS results along with C2, C3 and M200 mesh LSS resultsIt was expected that Concept_2 HE will provide the highest LSS due to the uniform temperature distribution which should lead to the uniform pressure distribution at the welding interface. Despite the fact that uniform temperature distribution was achieved, uniform pressure distribution was not obtained. The reason is that the adherend surface was curved, and its thickness was not constant along the overlap. That also might be the reason of the high scatter level within LSS results.

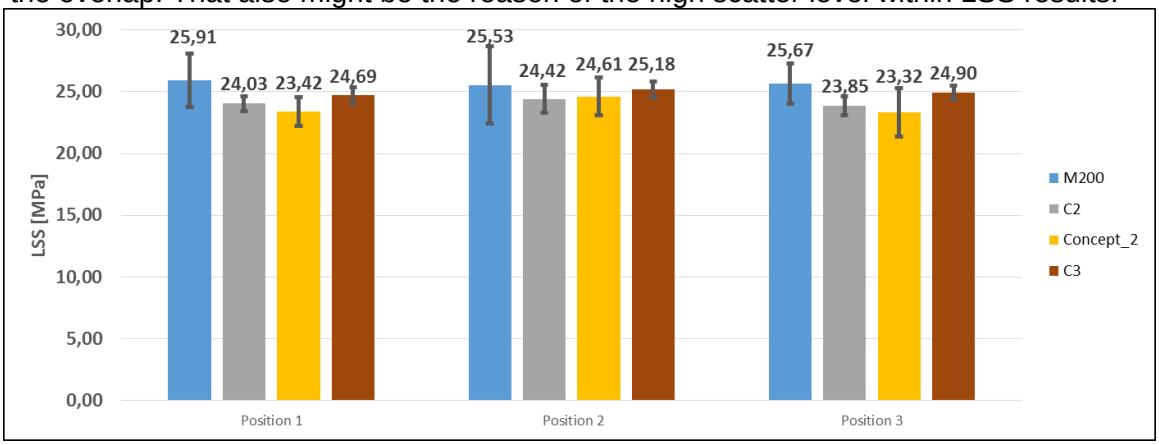

Figure 4.5-4: Concept_2 LSS results along with C2, C3 and M200 mesh LSS results

4.5.3 Fractography, Macroscopic Failure Features

The failure surface of a joint welded with Concept_2 HE is provided in Figure 4.5-5. It is interesting to see that all specimens welded with Concept_2 HE failed under Type I failure mode similarly to the Concept_1_0 type A005 and type B005. This happened because in the case of Concept_2 HE the wires width in the region close to the overlap edge where peel stresses are high is 0.205mm, comparable with 0.2mm in the case of Type A005 HE. Thus the failure path begins at the overlap end between adherend and glass fabric layer and propagates towards the middle of the overlap as it was explained in the case of failure surfaces of type A005 and B005 HE. That might be the second reason of why the LSS result of Concept_2 HE is lower than Concept_1_1 type C2 and C3 HE, because Type II failure mode involves damage to the glass fabric. This statement is reinforced

by the M200 joints LSS results. In the case of M200 mesh 80% of the joints failed under Type I mode and only 20% failed under Type II mode Figure 4.5-6. The ones which failed under Type II provided higher LSS, this is explained by the fact the failure mode involved rupture of the glass fabric.

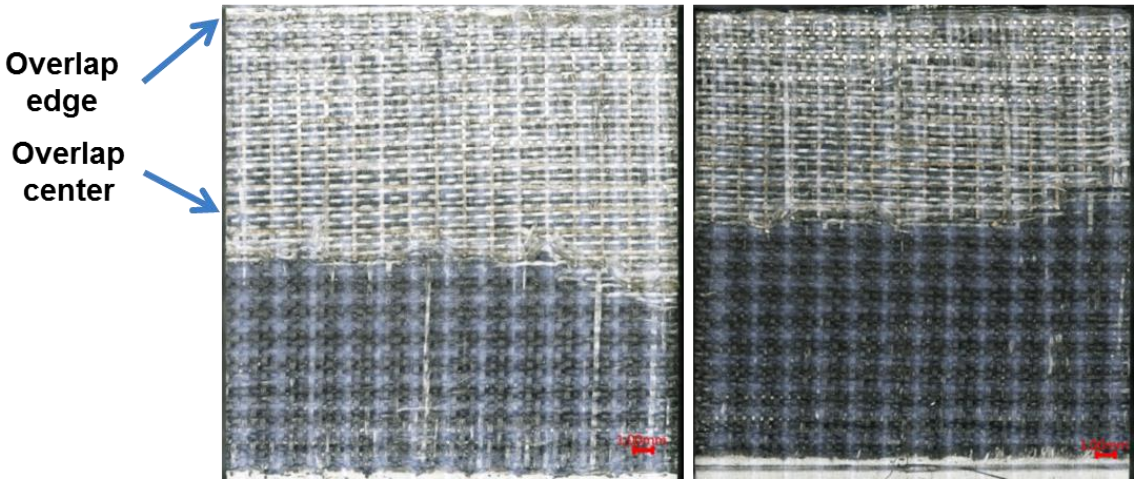

Figure 4.5-5: Concept_2 HE two mating failure surfaces of the same joint macroscopic view

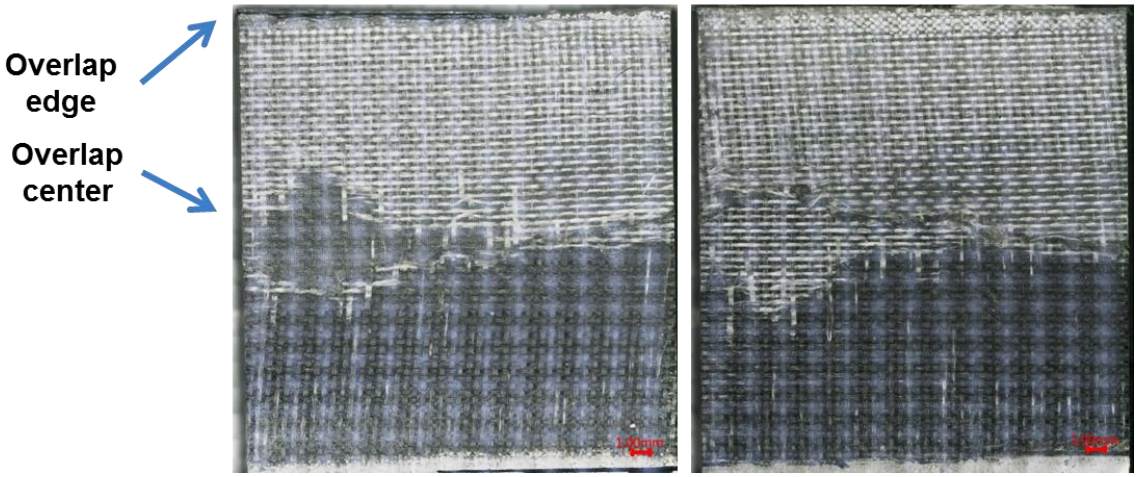

Figure 4.5-6: M200 HE Type I failure two mating failure surfaces of the same joint macroscopic

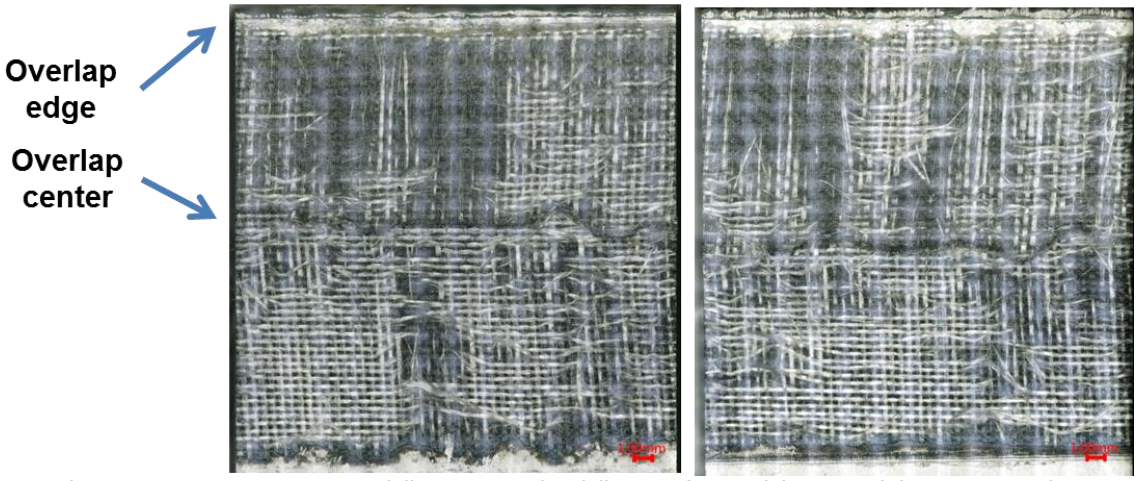

Figure 4.5-7: M200 HE Type II failure two mating failure surfaces of the same joint macroscopic

4.6 MICROSCOPY

Microscopy was used to assess the quality of the welded joints in terms of void presence in the joined laminates and at the welding interface. The micrographs were taken for the joints welded with Concept_1_0 type A005 HE, Concept_1_1 type C1 HE, M200 HE and Concept_2 HE. For each joint two cross-section micrographs were taken along the length and along the width of the overlap as it is shown in Figure 4.6-1.Transversal cut micrographs are attached to the appendix A.7, while the longitudinal micrographs will be discussed further in this chapter.

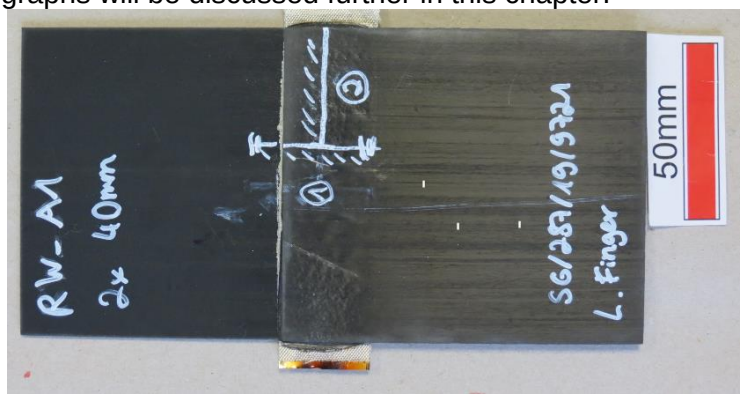

Figure 4.6-1: Joint location from where specimens for microscopy were taken.

Two main common features were found among the inspected joints. First, along the overlap width (path 1 Figure 4.6-1) the joined laminates and the welding interface were void-free independent of the HE type. From this can be deducted that the temperature gradient along the overlap width present at the welding interface in the case of welding using M200 mesh, Concept_1_0 and Concept_1_1 HE, did not lead to any voids formation. Second feature is that all joints presented voids in the adherends and at the welding interface in the area where HE enters into the welding stack (beginning of path 2 Figure 4.6-1). Because the joined adherends and impregnated HE were dried prior to the welding process, voids formation cannot be attributed to the moisture. The main cause of voids is the fibre movement at the edge where HE penetrates into the welding stack. And the mechanism is the following: The pressure on the overlap is applied by a stiff pressure applicator. Because of the fibre movement close to the transversal edges region the thickness of the adherend will decrease, thus the applied compressive load will be taken by the thicker regions of the overlap leading to a pressure drop close to the overlap transversal edges.The loss of pressure in that region will lead to the formation of voids due to the residual stresses present in the adherends.
Joints welded with Concept_2 HE showed less fibre movement Figure 4.6-5 than joints welded with other HE Figure 4.6-2 to Figure 4.6-4 and the void content seems to be lower than in the case of other HE. The reason of less fibre movement in the case of Concept_2 HE is that welding temperature was lower 360 °C (20 °C above PEKK melting temperature) compared to other HE where welding temperature was higher due to the transversal temperature gradients: 380 °C (40 °C higher than PEKK melting temperature) also because the welding time was shorter. According to Figure 4.5-1, in the case of Concept_2 HE the welding interface at position T1 and T2 (Figure 3.1-3) was kept at temperature above PEKK melting temperature 5-7 s only, while in the case of Concept_1_0 and M200 mesh it was 30 s Figure 4.3-1 and 20 s for Concept_1_1 Figure 4.4-1. Thus in the case of Concept 2 HE fibres had less time to move. The micrographs of the longitudinal cuts where fibre movement can be observed are shown in Figure 4.6-2 to Figure 4.6-4. The origin of the black curves marks which can be spotted in the micrographs at the bond line, is the glass fibre tear or HE tear during the sanding process and they should be disregarded.

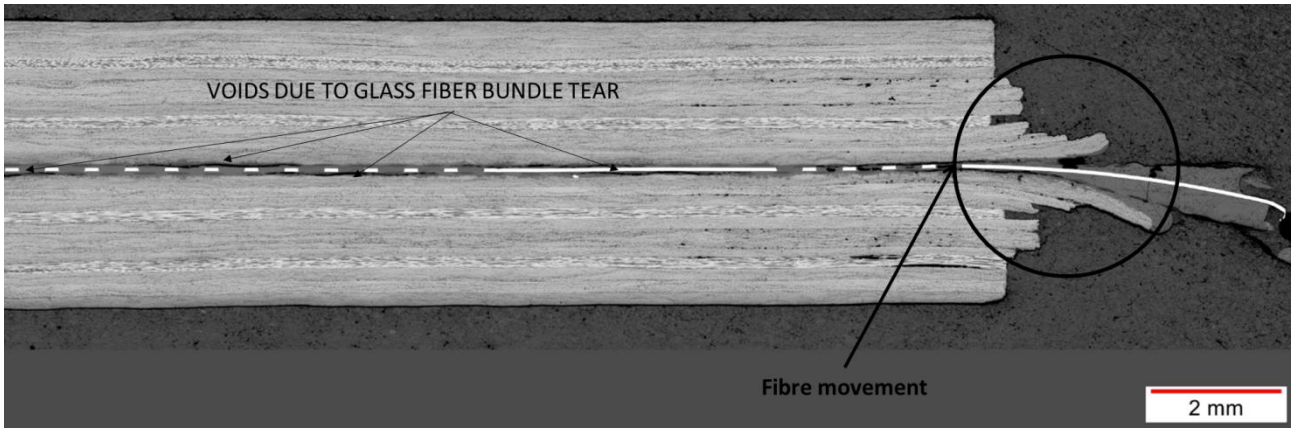

Figure 4.6-2: Joint cross section microscopic view in the longitudinal direction of a joint welded with A005 HE

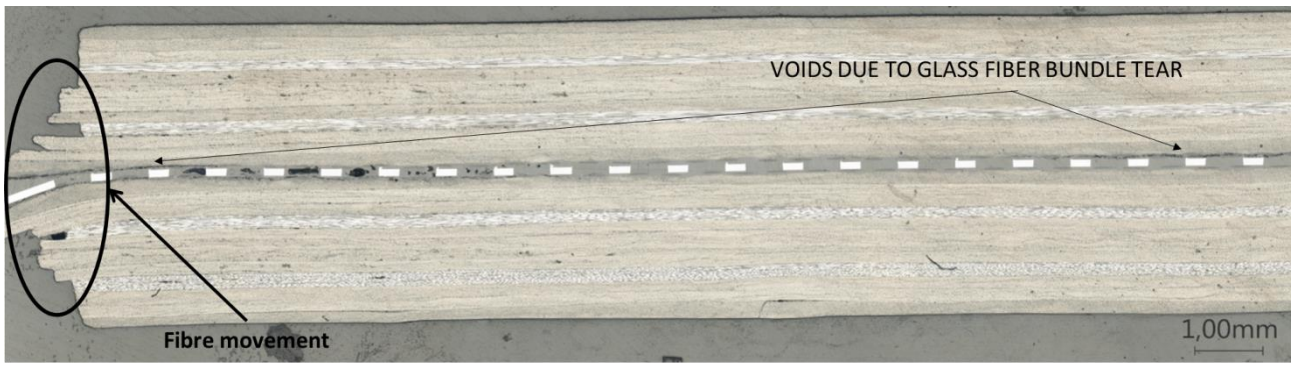

Figure 4.6-3: Joint cross section microscopic view in the longitudinal direction of a joint welded with C1 HE

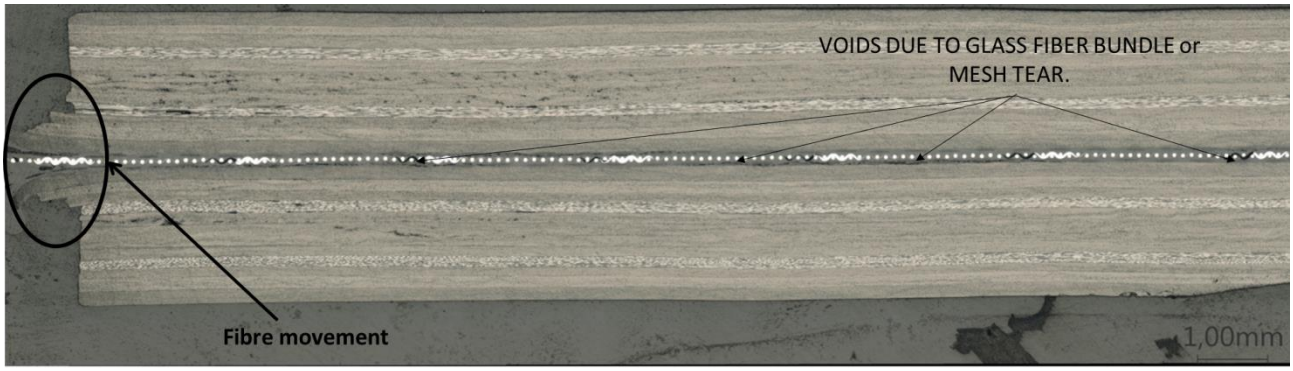

Figure 4.6-4: Joint cross section microscopic view in the longitudinal direction of a joint welded with M200HE

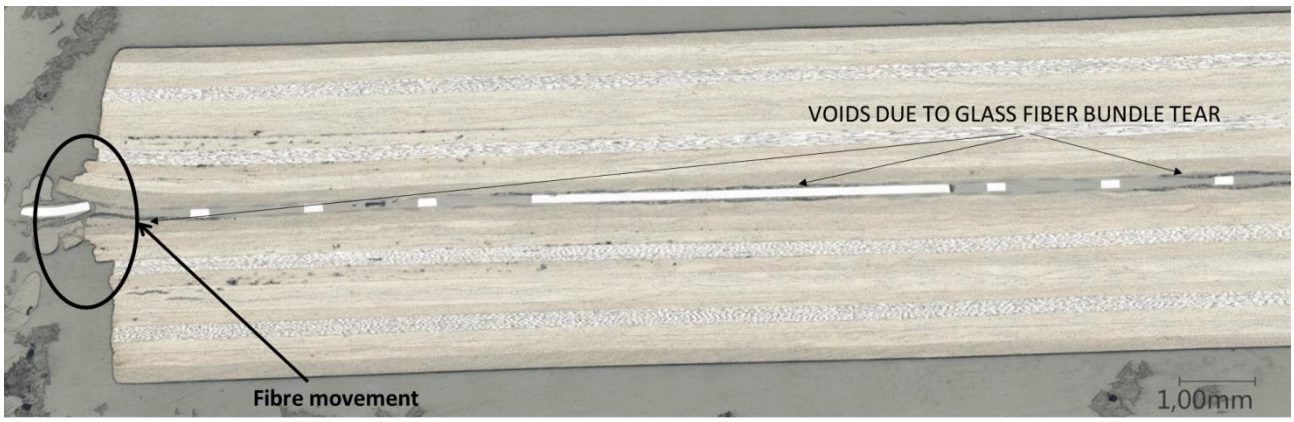

Figure 4.6-5: Joint cross section microscopic view in the longitudinal direction of a joint welded with Concept_2 HE

From the picture above it can be seen that in the case of Concept_2 HE only first 5-6 layers are affected by voids while in the case of A005 and C1 HE the first 7-8 layers were affected. The explanation is that in the case of Concept_2 the HAZ depth is smaller due to the lower process temperature at the welding interface. Thus fewer layers had their temperature above the resin melting point in the case of Concept_2 HE than in the case of other HE. Consequently voids formed under the residual stresses in the laminates only in the layers with temperature above the resin melting point.

5. CONCLUSION

The main objective of this study was to increase the lap shear strength of PEKK/CF laminates welded joints by achieving uniform temperature distribution at the welding interface, using a resistance tailored heating element(HE) able to provide different power levels over the heating element surface instead of conventional stainless steel mesh heating element. The desired electrical resistance was achieved by selectively removing material from the plate by a laser cutting process. In addition to the temperature distribution the geometry of the resulted plate heating element has also an effect on LSS. The effects on LSS of two main geometric parameters of the laser cut plate were investigated: open area ratio (OAR) and linear wire density (LWD). The effect of LWD on the LSS was studied by performing single lap shear tests of the joints welded with three heating elements with different LWD values (1.1, 1.37, 1.65), while other parameter where kept constant. In the case of OAR study a similar approach was utilized: three heating elements with different OAR were tested (0.5, 0.6, 0.7). The mechanical testing was followed by a fractographic analysis to understand the failure mechanisms involved.

During this research a FEM model was built and validated able to predict temperature distribution at the welding interface. Using the FEM model temperature output two HE concepts were created. The first concept (Concept_1) provided uniform distribution along the overlap (parallel to the heating element). The second concept (Concept_2) provided uniform temperature distribution over the entire welding interface. It was found that for Concept_1 HE uniform temperature distribution along the overlap length can be achieved for the following welding parameters sets: initial power per surface (IPS) at the welding interface of $51\ \frac{\mathrm{kW}}{\mathrm{m}^2}$ and $16.8\ \frac{\mathrm{kW}}{\mathrm{m}^2}$ in the region of the HE out of the welding interface for a welding time of 140 s. The second parameter set is: initial power per surface (IPS) of $71.4\ \frac{\mathrm{kW}}{\mathrm{m}^2}$ at the welding interface and $16.8\ \frac{\mathrm{kW}}{\mathrm{m}^2}$ in the region of the HE out of the welding interface for a welding time of 75 s. Both welding parameter sets brought the overlap centre to 380 °C. In the case of Concept_2, the uniform temperature distribution was achieved for the following welding parameters: IPS in the HE region out of the welding interface of $16.8\ \frac{\mathrm{kW}}{\mathrm{m}^2}$, IPS of a 2 mm wide strip along the welding interface longitudinal edges of $110.4\ \frac{\mathrm{kW}}{\mathrm{m}^2}$, IPS in the middle of the welding interface of $71.4\ \frac{\mathrm{kW}}{\mathrm{m}^2}$ and 60 s welding time. These parameters ensured a temperature of 360 °C all over the welding interface.

The LWD did not show any significant effect on LSS values for the tested configurations. However a change of the failure path was noticed. This change of the failure path was attributed to the relative size between the glass fabric gap used as electrical insulation and HE wire width. In the case when HE wire width is equal or bigger than the glass fabric gap size, the failure path initiates between HE and glass fabric layer, while in the cases when the HE wire width was smaller than glass insulation fabric gap size, the failure occurred between the glass fabric layer and the adherend. The explanation is that peel stresses are not evenly distributed over the overlap, being considerably higher at the overlap ends where the failure path begins. In the case when HE wire is wider than the glass fabric gap, the chance that the resin contained by one glass fabric gap at the overlap edge will bond to the HE wire only is higher than in the case when wire width is smaller than glass fabric gap. In the case when wire width is smaller than glass fabric gap a part of the resin contained by the glass fabric gap will bond to the HE wire while the rest will fusion with the resin from the opposite side of the heating element creating a stronger bonding between these two. Thus in the case when the HE wire width is higher than the glass fabric gap, the glass fabric/HE interface will be weaker and the failure will start from there.

Increase of OAR showed an increase of LSS. Joints welded with 0.7 OAR HE showed a 12% LSS increase compared to the joints welded with 0.5 OAR HE. The increase was attributed to a better bonding between HE and glass fabric, through the following mechanisms: Firstly, by increasing OAR the surface of weak interface resin/metal is decreased. Secondly, by increasing OAR the HE

gap size is also increasing, and some of the fibre glass bundles sink into the HE gap, by that creating a better interlocking between HE and glass fabric.

The uniform temperature distribution did not lead to a higher LSS as it was expected. However it led to other significant advantages: Lower process temperature due to absence of temperature gradients along the welding interface. Lower process temperature also led to shorter welding time and to a smaller HAZ (Heat Affected Zone). Due to the fact that the process was stopped soon after the welding interface reached resin's melting temperature, the fibre movement phenomenon was considerably decreased.

The fractographic analysis in this research showed that the failure mechanism is dominated by the peel stress at the overlap end and by the shear stress closer to the overlap centre. Under the peel stresses the weakest link was found to be the bonding between heating element and resin, while under the shear stresses the weakest link was found to be glass fibre/resin adhesion.

6. RECOMMENDATIONS

In this chapter several recommendations will be given for the future research and improvements based on conclusions drawn from the research and from observations during the welding trials.

Improvements to the welding machine

- The main difficulty encountered during the welding trials was alignment of the HE together with the adherends. Thus it will be useful to have a mechanism for an easier fixation and alignment.
- The thermal insulation material block used tended to delayer once it was heated up to 280°C. Thus in the future a thermal insulator material which can keep its integrity at higher temperature should be used, to ensure that the surface of the thermal insulation block will stay flat after multiple welding cycles.
- The surface of the welded laminates was not perfectly flat, their thickness varied from 2.05 mm to 2.22 mm within the same specimen. Because of that uniform pressure distribution was impossible to achieve. To increase the uniformity of the pressure distribution at the welding interface even for curved adherends, it is suggested to use a tube like pressure applicator. At least this can ensure that the pressure at the adherend/pressure applicator interface is uniformly distributed.
- The welding machine can deliver constant current intensity only. During the process, current intensity and voltage can be monitored. The monitored voltage between welding trials under the same constant current intensity using the same HE showed differences up to 1 V. According to Ohm's law the reason of this mismatch is the difference in the overall resistance between heating elements used. The resistance difference was attributed to the different contact resistance value between the electric contact clamps and HE, since other parameters were unchanged. Thus it is suggested to improve the electrical clamping mechanism to ensure the same value of contact resistance if it is desire to monitor the welding process accurately.

Further recommended research

The research results showed an increase of the LSS with the HE OAR increase. The main limitation for the OAR increase is the HE gap size; higher OAR involves bigger HE gap size. If the gap size will be too high, there is a risk that during the welding process high temperature gradients can occur within a single gap, which may lead to unwelded regions at the gap centre. The gap size between the longitudinal HE wires is more important than the gap size between transversal gap wires, because the heat is generated by the longitudinal wires and transversal wires only aid heat distribution. Thus it will be interesting to find the maximum gap size which can still provide acceptable low temperature gradients within one gap by using the developed FEM model.

Longitudinal temperature distribution was found to be sensitive to the relative position of the HE region designed to be at the welding interface and the adherends. A small misalignment between these two led to longitudinal temperature gradients. The sensitivity is increasing with the increase of initial power per surface at the HE region designed to be at the welding interface, since this problem was not noticed in the case of joints welded under IPS equal to $51\ \frac{\mathrm{kW}}{\mathrm{m}^2}$, compared to the joints welded under high IPS values of $71.4\ \frac{\mathrm{kW}}{\mathrm{m}^2}$. Thus to decrease this undesired effect and to allow coarser positioning tolerances it is recommended to design a small strip along the transversal edge of the welding interface with lower IPS, $50\ \frac{\mathrm{kW}}{\mathrm{m}^2}$ for instance, while in the centre of the overlap to have high IPS of $71.4\ \frac{\mathrm{kW}}{\mathrm{m}^2}$ as in the case of Concept_1_1 HE.

The glass fabric is a cheap and easy to implement solution against current leakage, but it provided low LSS of the welded joints. To improve LSS: future work should be oriented towards finding a better electrical insulation solution for the heating element. Coating it with TiO_2 seems to be a good

solution, albeit an expensive one. The heating element will not be only electrically insulated but also the bonding between resin and coated metal can be increased. In this research bonding between metal and resin was found to be the weakest link against peel stresses occurring at the overlap end where the failure path originates. Thus by increasing bonding strength between resin and metal, the failure path initiation can be delayed, leading to the LSS increase.

The effect of glass fabric on LSS was out of this project research scope. However the influence of glass fabric on joint LSS is important. It is suggested for the following research to focus on understanding the impact of glass fabric layer has on LSS. From the observations made during this research is suggested to use glass fabric with high OAR in order to decrease the surface of weak interface between glass fibres and resin. To increase the bonding strength between glass fabrics and resin it is recommended to use sized glass fabrics. The gap size of the glass fabric should be bigger than the HE wire size, through that it is ensured that the resin contained by the fabric gap fuses with the resin from the opposite side of the HE.

Concept_2 HE showed uniform temperature distribution at the welding interface not only at the end of the welding process but during the transient state as well. Thus the in-situ temperature monitoring might be possible to implement. The temperature can be calculated in function of the resistance change due to the temperature increase at the welding interface. In order to implement this, contact resistance between electrical clamps and heating element ends should be known and the clamping condition should be identic from experiment to experiment.

BIBLIOGRAPHY

[1] [Online]. Available: https://www.airbus.com/aircraft/passenger-aircraft/a350xwb-family.html#smartchoice. [Accessed 08. 05. 2019].

[2] M. Dubé, A. Chazerain, P. Hubert, A. Yousefpour and H. E. Bersee, “Characterization of resistance-welded thermoplastic composite double lap joints under static and fatigue loading,” *Journal of Thermoplastic Composite Materials,* vol. 28, no. 6, pp. 762-776, 2015.

[3] S. H. Mcknight, S. T. Holmes, J. W. Gilespie, C. L. Lambing and J. M. Marinelli, “Scaling Issues in Resistance Welded Thermoplastic Composite Joints,” *Advances in Polymer Technology,* vol. 16, no. 4, pp. 279-295, 1997.

[4] É. Talbot, P. Hubert, M. Dubé and A. Yousefpour, “Optimization of thermoplastic composites resitance welding parameters based on transient heat transfer finite element modeling,” *Journal of Thermoplastic Composite Materials,* vol. 26, no. 5, pp. 699-7017, 2013.

[5] H. Shi, I. Fernandes-Villegas and H. E. N. Bersee, “Modelling of Heat Transfer and Consolidation for Thermoplastic Composites Resistance Welding,” in *18th International Conferince on Composite Materials*, 2011.

[6] H. Shi, I. F. Villegas and H. E. Bersee, “Analysis of void formation in thermoolastic composites during the resitance welding,” *Journal of Thermoplastic Composite materials,* vol. 30, no. 12, pp. 1654-1674, 2017.

[7] S. Holmes and J. Gillespie, “Thermal Analysis for Resistance Welding of Large-Scale Thermoplastic Composite Joints,” *Journal of Reinforced Plastics and Composites,* vol. 12, no. 6, pp. 723-736, 1993.

[8] X. R. Xiao, S. V. Hoa and K. N. Street, “Processing and Modelling of Resistance Welding of APC-2 Composite,” *Journal of Composite Materials,* vol. 26, no. 7, pp. 1031-1049, 1992.

[9] M. Dubé, “Static and Fatigue Behaviour of Thermoplastic Composite Laminates Joined by Resistance Welding,” PhD Thesis,McGILL University, Montreal, 2007.

[10] M. Dubé, P. Hubert, J. N. Gallet, D. Stavrov, H. E. Bersee and A. Yousefpour, “Metal mesh heating element size effect in resistance welding of thermoplastic composites,” *Journal of Composite Materials,* vol. 46, no. 8, pp. 911-919, 2012.

[11] M. Dubé, P. Hubert, J. N. Gallet, D. Stavrov, H. E. Bersee and A. Yousefpour, “Fatigue performances characterization of resistance-welded thermoplastic composites,” *Composites Scinece and Technology,* vol. 68, no. 7-8, pp. 1759-1765, 2008.

[12] C. Ageorges, L. Ye, Y.-W. Mai and M. Hou, “Characteristics of resistance welding of lap shear coupons. Part I: Heat Transfer,” *Composites Part A: Applied Science and Manufacturing,* vol. 29, no. 8, pp. 911-919, 1998.

[13] C. Ageorges, L. Ye and M. Hou, “Experimental investigation of the reistance welding for thermoplastic-matrix composites. Part I: heating element and heat transfer,” *Composites Science and technology,* vol. 60, no. 7, pp. 1027-1039, 2000.

[14] C. Ageorges, L. Yen and M. Hou, “Experimental invetsigation of the resistance welding of thermoplastic-matrix compopsites. Part II Optimum processing window and mechanical performance,” *Composite Science and Technology,* vol. 60, no. 8, pp. 1191-1202, 2000.

[15] H. Shi, I. Fernandez Villegas, M. A. Octeau, E. N. B. Harald and A. Yousefpour, “Continuous resistance welding of thermoplastic composites: Modeling of heat generation and heat transfer,” *Composite Part A: Applied Science and Manufacturing,* vol. 70, pp. 16-26, 2015.

[16] M. Hou, M. Yang, A. Beehag, Y. W. Mai and L. Ye, “Resistance welding of carbon fibre reinforced thermoplastic composite using alternative heating element,” *Composite Strutures,* vol. 47, no. 1-4, pp. 667-672, 1999.

[17] H. Shi, “Resistance welding of thermoplastic composites. Process and Perfromance,” Phd Thesis, Delft University of Tehchnology, 2014.

[18] M. Dubé, P. Hubert, A. Yousefpour and J. Denault, “Current leakage prevention in resistance welding of carbon fibre reinforced thermoplastics,” *Composites Science and Technology,* vol. 68, no. 6, pp. 1679-1587, 2008.

[19] I. G. Requena, A. S. Lobera and L. M. V. Fernandez, “Characterizing of meshes for resistance welding of high temperature reinforced laminate thermoplastic (RLT),” *Procedia Engineering,* vol. 63, pp. 556-563, 2013.

[20] I. F. Villegas and H. E. N. Bersee, “Characterisation of a metal mesh heating element fro closed-loop resistance welding of thermoplastic composites,” *Journal of Thermoplastic Composite Materials,* vol. 28, no. 1, pp. 46-65, 2015.

[21] D. Stavrov and H. E. N. Bersee, “Resistance welding of thermoplastic compoistes_an overview,” *Composites Part A: Applied Science and Manufacturing,* vol. 36, no. 1, pp. 39-54, 2005.

[22] M. Dubé, P. Hubert, Y. A. and J. Denault, “Resistance welding of thermoplastic composites skin/stringer joints,” *Composites Part A: Applied Science and Manufacturing,* vol. 38, no. 12, pp. 2541-2552, 2007.

[23] A. Smiley, M. Chao and J. Gillespie, “Influence and control of bondline thickness in fusion bonded joints of thermoplastic composites,” *Composite Manufacturing,* vol. 2, no. 3/4, pp. 223-232, 1991.

[24] V. Rohart, L. L. Lebel and M. Dubé, “Improvement of the lap shear strength of resistance-welded,” in *The Fourth International Symposium on Automated Composites Manufacturing*, Montréal, 2019.

[25] H. Shi, I. F. Villegas and B. H.E.N, “Effect of Fibre-Matrix Adhesion and Fibre Orientation on Thermoplastic Composite Welded Joints,” in *SAMPE*, Long Beach, CA, The USA, 2013.

[26] S. D. B. de Souza, A. B. R. M. Abrahão, M. L. Costa, J. M. F. Marlet, L. R. O. Hein and E. C. Botelho, “Experimental Investigation of Processing Welding Parameters For PPS/Carbon Fiber Laminates fo Aeronautical Applications,” *Advanced Materials Research,* vol. 1135, pp. 62-74, 2016.

[27] N. Koutras, I. F. Villegas and R. Benedictus, “Influence of temperature on the strength of resistance welded glass fibre reinforced PPS joints,” *Composites Part A: Applied Science and Manufacturing,* vol. 105, pp. 57-67, 2018.

[28] O. C. Putman and V. U. K, “Interfacial Shear Strength in a Metal-Thermoplastic Composite,” *Polymers and Polymer Composites,* vol. 18, no. 7, pp. 369-380, 2009.

[29] *Abaqus user manual..*

[30] AGK Hochleistungswerkstoffe GmbH, [Online]. Available: https://www.agk.de/international/en/html/html_produkte/AS500MAS600MAS800M.htm. [Accessed 07 06 2019].

[31] THE GUND COMPANY, [Online]. Available: http://thegundcompany.com/wp-content/uploads/2016/11/Mica-M-from-The-Gund-Co.pdf. [Accessed 01 07 2019].

[32] C. Y. Ho and T. K. Chu, “Electrical Resistivity and Thermal Conductivity of Nine Selected AISI Stainless Steels,” American Iron and Steel Institute, Washington, 1977.

[33] P. Li, C. Zhang, Z. Zhu, W. Tian and A.Liu, “Research on Heat Source Model and Weld Profile for Fiber Laser Welding of A 304 Stainless Steel Thin Sheet,” *Hindawi,* vol. 2018, p. 12, 2018.

[34] *Airbus Materials & Processes Department.*

[35] “PDS_Tenax-E_TPUD_PEKK-HTS45_194_v00_en”.

[36] D. M. Gleich, M. V. Tooren and A. Beukers, “Analysis and evaluation of bondline thickness effects on failure load in adhesively bonded structures,” *Journal of Adhesion Science and Technology,* vol. 15, no. 9, pp. 1091-1101, 2001.

APPPENDIX

A.1 STEEL MESH VOLUME CALCULATION

Steel mesh volume calculation

Steel Volume contained by the FEM modelled mesh heating element is calculated by summing the volume of all wires contained by the mesh. To calculate the volume of one wire it is necessary to know wire cross section area and its length. Wire cross section area can be easily calculated by using the circle area formula. However the Length of a longitudinal wire contained by the mesh will be higher than the length of the mesh itself due to the waviness of the mesh. The effective length of a mesh wire can be calculated by multiplying the longitudinal wire length between two transversal wires by the overlaps number in the longitudinal direction. The length of the longitudinal wire between two transversal wires will be equal to the wire neutral axis length. The neutral axis length between two wires will be given by the tangent length to the circles described by the neutral axis curvature due to the overlap between two transversal wires. The tangent and circle arc which needs to be found are pictured in the Figure A.1-1.

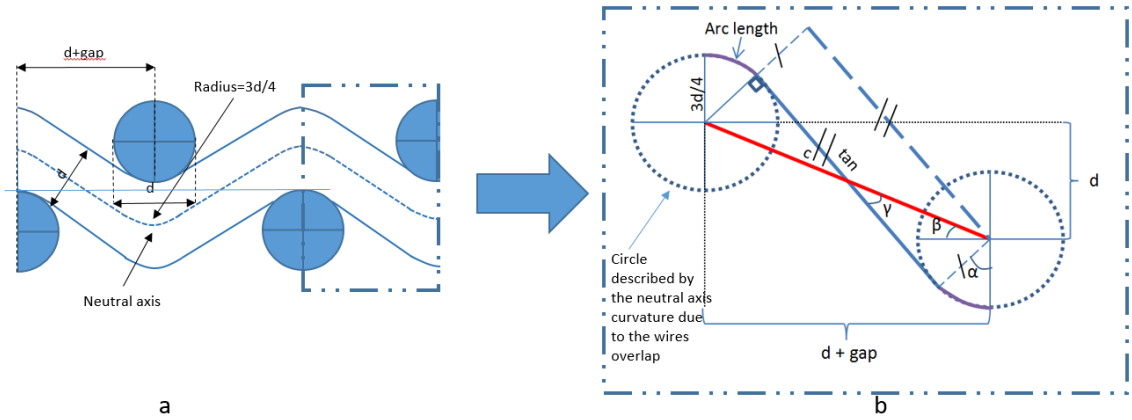

Figure A.1-1: Transversal view of a stainless steel mesh with "d" diameter and "gap" distance between two wires(a), neutral axis length of a longitudinal wire between two transversal wires and vice versa (b)

The neutral axis length between two consequent overlaps is given by the formula:

$$l = 2l_{arc} + tan \tag{A.1-1}$$

The tangent to the circle described by the neutral axis curvature can be calculated with the formula:

$$tan = \sqrt{c^2 - \left(2\frac{3d}{4}\right)^2} \tag{A.1-2}$$

Where $\boldsymbol{c}$ is the segment which connects the centres of two consequent circles described by neutral axis due to the two the overlaps.

$$c = \sqrt{(g+d)^2 + d^2} \tag{A.1-3}$$

The circle arc length is dependent on the angle $\boldsymbol{\alpha}$ angle between vertical line and perpendicular to the tangent from the centre of the circle.

$$l_{arc} = 2\pi\frac{3d}{4}\frac{\alpha}{2\pi} \tag{A.1-4}$$

And $\boldsymbol{\alpha}$ is given by:

$$\alpha = \gamma + \beta = \sin^{-1}\left(\frac{3d}{4}\frac{2}{c}\right) + \tan^{-1}\left(\frac{d}{g+d}\right) \quad \text{(A.1-5)}$$

As it was stated before the length of one longitudinal wire will be obtained by multiplying $\boldsymbol{l}$ with the number of overlaps which is equal to the number of vertical wires which can be calculated by **dividing** $\boldsymbol{Length}$ of the mesh by $(\boldsymbol{g}+\boldsymbol{d})$, vice versa for the transversal wire Length

$$\begin{aligned} L_{long} &= N_{trans} \cdot l; \quad L_{trans} = N_{long} \cdot l \\ N_{long} &= \frac{Width}{g+d}; \quad N_{trans} = \frac{Length}{g+d} \end{aligned} \quad \text{(A.1-6)}$$

Thus steel volume can be calculated:

$$Vol_{steel} = \pi\frac{d}{4}\left(L_{long} \cdot N_{long} + L_{trans} \cdot N_{trans}\right) \quad \text{(A.1-7)}$$

By writing the formula of the mesh volume in function of the **mesh diameter**, **gap length** and **Width,** the next formula will be obtained:

$$Vol_{steel} = \frac{\pi \cdot Length \cdot Width \cdot d^2\left[\frac{3d}{2}\tan^{-1}\left(\frac{d}{d+g}\right) + \frac{3d}{2}\sin^{-1}\left(\frac{\frac{3d}{2}}{\sqrt{2d^2+2dg+g^2}}\right) + \frac{\sqrt{-d^2+8dg+4g^2}}{2}\right]}{2(d+g)^2} \quad \text{(A.1-8)}$$

Where: $\boldsymbol{d}$ is the mesh diameter, $\boldsymbol{g}$ is the mesh gap (gap between two wires)

PEKK volume $\boldsymbol{Vol_{pekk}}$ can be simply calculated by deducting the stainless steel volume from the volume of the modelled HE.

A.2 M200 HE MATERIAL THERMAL PROPERTIES FOR FEM MODEL

Table A.2-1 FEM thermal properties of M200 HE at the welding interface

Temperature [°C]	Thermal cond [W/(m·K)]		Specific heat capacity [J/(kg·K)]	Electrical conductivity x[(Ω*m)$^{-1}$]	Mass density [kg/m^3]
	K_x, k_z	K_y			
20	3.16	4.78	635	$1.700 \cdot 10^5$	3360
40	3.24	4.89	638	$1.661 \cdot 10^5$	
60	3.31	5.01	642	$1.625 \cdot 10^5$	
80	3.38	5.12	658	$1.590 \cdot 10^5$	
100	3.44	5.21	674	$1.559 \cdot 10^5$	
120	3.51	5.32	690	$1.529 \cdot 10^5$	
140	3.58	5.42	707	$1.502 \cdot 10^5$	
160	3.64	5.52	740	$1.476 \cdot 10^5$	
180	3.71	5.63	774	$1.451 \cdot 10^5$	
200	3.78	5.74	793	$1.428 \cdot 10^5$	
220	3.84	5.84	812	$1.404 \cdot 10^5$	
240	3.91	5.94	828	$1.383 \cdot 10^5$	
260	3.96	6.03	843	$1.363 \cdot 10^5$	
280	4.02	6.13	853	$1.343 \cdot 10^5$	
300	4.08	6.22	864	$1.324 \cdot 10^5$	
320	4.14	6.31	930	$1.306 \cdot 10^5$	
340	4.2	6.40	1135	$1.289 \cdot 10^5$	
360	4.25	6.49	849	$1.273 \cdot 10^5$	
380	4.31	6.58	857	$1.257 \cdot 10^5$	
400	4.37	6.67	859	$1.242 \cdot 10^5$	
420	4.43	6.76	860	$1.227 \cdot 10^5$	

Table A.2-2 FEM thermal properties of M200 HE out of the welding stack

Temperature [°C]	Thermal cond [W/(m·K)]		Specific heat capacity [J/(kg·K)]	Electrical conductivity x[(Ω*m)$^{-1}$]	Mass density [kg/m^3]
	k_x, k_z	k_y			
20	3.16	4.78	464	$1.700 \cdot 10^5$	3360
40	3.24	4.89	468	$1.661 \cdot 10^5$	
60	3.31	5.01	472	$1.625 \cdot 10^5$	
80	3.38	5.12	476	$1.590 \cdot 10^5$	
100	3.44	5.21	480	$1.559 \cdot 10^5$	
120	3.51	5.32	484	$1.529 \cdot 10^5$	
140	3.58	5.42	488	$1.502 \cdot 10^5$	
160	3.64	5.52	492	$1.476 \cdot 10^5$	
180	3.71	5.63	496	$1.451 \cdot 10^5$	
200	3.78	5.74	500	$1.428 \cdot 10^5$	
220	3.84	5.84	504	$1.404 \cdot 10^5$	
240	3.91	5.94	509	$1.383 \cdot 10^5$	
260	3.96	6.03	509	$1.363 \cdot 10^5$	
280	4.02	6.13	509	$1.343 \cdot 10^5$	
300	4.08	6.22	507	$1.324 \cdot 10^5$	
320	4.14	6.31	507	$1.306 \cdot 10^5$	
340	4.2	6.40	506	$1.289 \cdot 10^5$	
360	4.25	6.49	505	$1.273 \cdot 10^5$	

380	4.31	6.58	505	$1.257 \cdot 10^5$	
400	4.37	6.67	504	$1.242 \cdot 10^5$	
420	4.43	6.76	504	$1.227 \cdot 10^5$	

A.3 CONCEPT_1_0, CONCEPT_1_1 HE MATERIAL THERMAL PROPERTIES FOR FEM MODEL

Table A.3-1 FEM thermal properties of Concept_1_0 HE at the welding interface

Temperature [°C]	Thermal cond [W/(m·K)]		Specific heat capacity [J/(kg·K)]	Electrical conductivity x[(Ω*m)$^{-1}$]	Mass density [kg/m^3]
	k_x, k_z	k_y			
20	6.31	8.13	542	$4.638 \cdot 10^5$	4885
40	6.46	8.33	546	$4.532 \cdot 10^5$	
60	6.61	8.53	549	$4.433 \cdot 10^5$	
80	6.76	8.72	559	$4.338 \cdot 10^5$	
100	6.89	8.89	569	$4.254 \cdot 10^5$	
120	7.03	9.07	578	$4.172 \cdot 10^5$	
140	7.17	9.25	588	$4.097 \cdot 10^5$	
160	7.31	9.44	605	$4.028 \cdot 10^5$	
180	7.45	9.61	623	$3.960 \cdot 10^5$	
200	7.56	9.80	634	$3.895 \cdot 10^5$	
220	7.73	9.98	745	$3.832 \cdot 10^5$	
240	7.85	10.15	654	$3.773 \cdot 10^5$	
260	7.98	10.31	661	$3.718 \cdot 10^5$	
280	8.10	10.47	666	$3.665 \cdot 10^5$	
300	8.23	10.64	670	$3.613 \cdot 10^5$	
320	8.35	10.80	700	$3.562 \cdot 10^5$	
340	8.47	10.95	793	$3.516 \cdot 10^5$	
360	8.59	11.11	662	$3.472 \cdot 10^5$	
380	8.71	11.27	665	$3.430 \cdot 10^5$	
400	8.83	11.42	666	$3.388 \cdot 10^4$	
420	8.95	11.58	667	$3.348 \cdot 10^4$	

Table A.3-2 FEM thermal properties of Concept_1_1 HE at the welding interface

Temperature [°C]	Thermal cond [W/(m·K)]		Specific heat capacity [J/(kg·K)]	Electrical conductivity x[(Ω*m)$^{-1}$]	Mass density [kg/m^3]
	k_x, k_z	k_y			
20	4.26	6.07	591	$3.313 \cdot 10^5$	3945
40	4.36	6.20	594	$3.237 \cdot 10^5$	
60	4.46	6.35	598	$3.166 \cdot 10^5$	
80	4.56	6.50	611	$3.099 \cdot 10^5$	
100	4.65	6.63	624	$3.038 \cdot 10^5$	
120	4.74	6.76	637	$2.980 \cdot 10^5$	
140	4.83	6.89	650	$2.927 \cdot 10^5$	
160	4.92	7.03	676	$2.877 \cdot 10^5$	
180	5.01	7.16	702	$2.829 \cdot 10^5$	
200	5.10	7.29	717	$2.782 \cdot 10^5$	
220	5.19	7.43	733	$2.737 \cdot 10^5$	
240	5.23	7.55	746	$2.695 \cdot 10^5$	
260	5.36	7.67	756	$2.656 \cdot 10^5$	
280	5.44	7.79	764	$2.618 \cdot 10^5$	
300	5.52	7.91	772	$2.580 \cdot 10^5$	
320	5.60	8.03	821	$2.544 \cdot 10^5$	
340	5.68	8.15	973	$2.511 \cdot 10^5$	

360	5.76	8.26	761	$2.480 \cdot 10^5$	
380	5.84	8.37	766	$2.450 \cdot 10^5$	
400	5.92	8.49	767	$2.420 \cdot 10^4$	
420	6.00	8.61	769	$2.391 \cdot 10^4$	

A.4 CONCEPT_2_0 HE STRIP MATERIAL THERMAL PROPERTIES FOR FEM MODEL

Table A.4-1 FEM thermal properties of Concept_2 HE of the strip between two conductive wires in Region 4

Temperature [°C]	Thermal cond [W/(m·K)]		Specific heat capacity [J/(kg·K)]	Electrical conductivity y,z[(Ω*m)$^{-1}$]	Mass density [kg/m^3]
	k_y, k_z	k_x			
20	2.73		751	$2.180 \cdot 10^5$	
40	2.79		753	$2.131 \cdot 10^5$	
60	2.85		755	$2.084 \cdot 10^5$	
80	2.92		780	$2.039 \cdot 10^5$	
100	2.97		804	$1.999 \cdot 10^5$	
120	3.03		829	$1.961 \cdot 10^5$	
140	3.08		853	$1.926 \cdot 10^5$	
160	3.14		907	$1.893 \cdot 10^5$	
180	3.2		960	$1.862 \cdot 10^5$	
200	3.25		989	$1.831 \cdot 10^5$	
220	3.31	0.3	1018	$1.801 \cdot 10^5$	2428
240	3.37		1042	$1.774 \cdot 10^5$	
260	3.42		1065	$1.748 \cdot 10^5$	
280	3.47		1084	$1.723 \cdot 10^5$	
300	3.52		1104	$1.698 \cdot 10^5$	
320	3.57		1214	$1.674 \cdot 10^5$	
340	3.62		1556	$1.653 \cdot 10^5$	
360	3.67		1080	$1.632 \cdot 10^5$	
380	3.72		1093	$1.612 \cdot 10^5$	
400	3.77		1097	$1.593 \cdot 10^5$	
420	3.82		1101	$1.574 \cdot 10^5$	

Table A.4-2 FEM thermal properties of Concept_2 HE of the strip between two conductive wires in Region 3

Temperature [°C]	Thermal cond [W/(m·K)]		Specific heat capacity [J/(kg·K)]	Electrical conductivity y,z[(Ω*m)$^{-1}$]	Mass density [kg/m^3]
	k_y, k_z	k_x			
20	1.73		847	$4.638 \cdot 10^5$	
40	1.76		848	$4.638 \cdot 10^5$	
60	1.8		850	$4.638 \cdot 10^5$	
80	1.84		881	$4.638 \cdot 10^5$	
100	1.87		913	$9.288 \cdot 10^4$	
120	1.9		944	$9.110 \cdot 10^4$	
140	1.94		975	$8.948 \cdot 10^4$	
160	1.97		1045	$8.795 \cdot 10^4$	
180	2.00	0.28	1115	$8.648 \cdot 10^4$	1971
200	2.04		1153	$8.505 \cdot 10^4$	
220	2.07		1189	$8.367 \cdot 10^4$	
240	2.10		1220	$8.240 \cdot 10^4$	
260	2.13		1250	$8.119 \cdot 10^4$	
280	2.16		1277	$8.002 \cdot 10^4$	
300	2.19		1303	$7.889 \cdot 10^4$	
320	2.23		1451	$7.778 \cdot 10^4$	
340	2.25		1907	$7.677 \cdot 10^4$	

360	2.28		1272	$7.582 \cdot 10^4$	
380	2.31		1290	$7.489 \cdot 10^4$	
400	2.34		1295	$7.399 \cdot 10^4$	
420	2.37		1301	$7.310 \cdot 10^4$	

A.5 CONCEPT_1_0 HE PROPERTIES AT THE TAILORED REGION FOR THE ELECTRIC SIMULATION ONLY

Table A.5-1 Concept_1_0 FEM thermal properties for the electrical simulation only

Temperature [°C]	Thermal cond [W/(m·K)]		Specific heat capacity [J/(kg·K)]	Electrical conductivity $[(\Omega*m)^{-1}]$	Mass density $[kg/m^3]$
	k_x, k_z	k_z			
20	6.05	7.95	464.1	$4.638 \cdot 10^5$	4254
40	6.2	8.14	468.2	$4.532 \cdot 10^5$	
60	6.35	8.34	472.2	$4.433 \cdot 10^5$	
80	6.49	8.53	476.3	$4.338 \cdot 10^5$	
100	6.63	8.71	480.4	$4.254 \cdot 10^5$	
120	6.76	8.88	484.5	$4.172 \cdot 10^5$	
140	6.89	9.06	488.6	$4.097 \cdot 10^5$	
160	7.04	9.24	492.7	$4.028 \cdot 10^5$	
180	7.17	9.42	496.7	$3.960 \cdot 10^5$	
200	7.31	9.60	500.9	$3.895 \cdot 10^5$	
220	7.45	9.78	504.8	$3.832 \cdot 10^5$	
240	7.57	9.95	509	$3.773 \cdot 10^5$	
260	7.70	10.11	509.4	$3.718 \cdot 10^5$	
280	7.82	10.23	508.6	$3.665 \cdot 10^5$	
300	7.94	10.43	507.8	$3.613 \cdot 10^5$	
320	8.06	10.59	507.8	$3.562 \cdot 10^5$	
340	8.18	10.75	506.3	$3.516 \cdot 10^5$	
360	8.30	10.90	505.5	$3.472 \cdot 10^5$	

A.6 PICTURES WITH MANUFACTURED HE

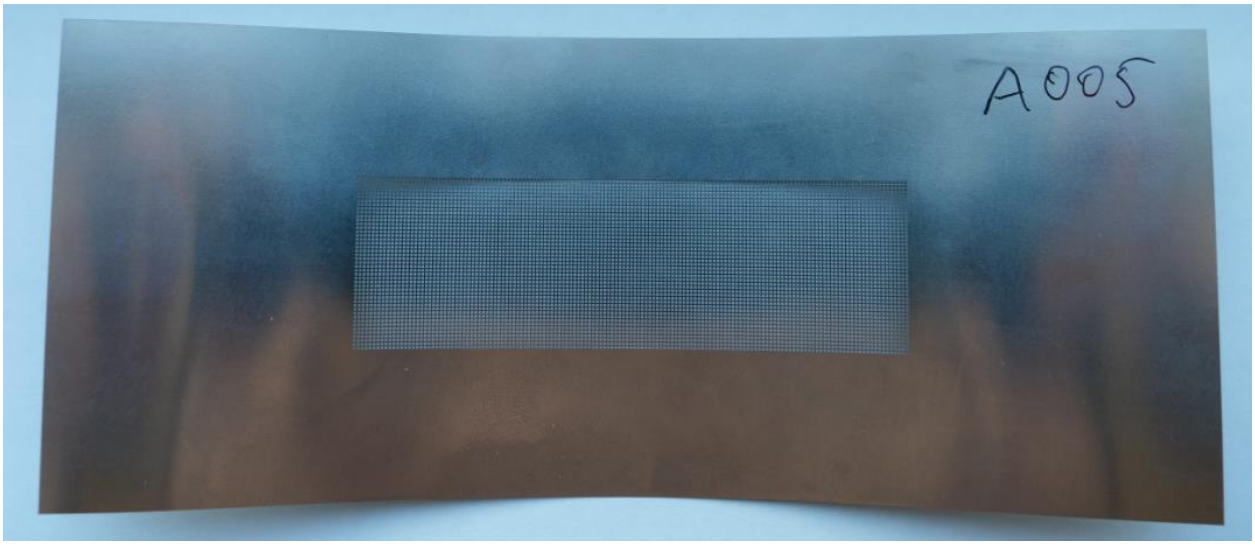

Figure A.6-1: Concept_1_0 type A005/A01

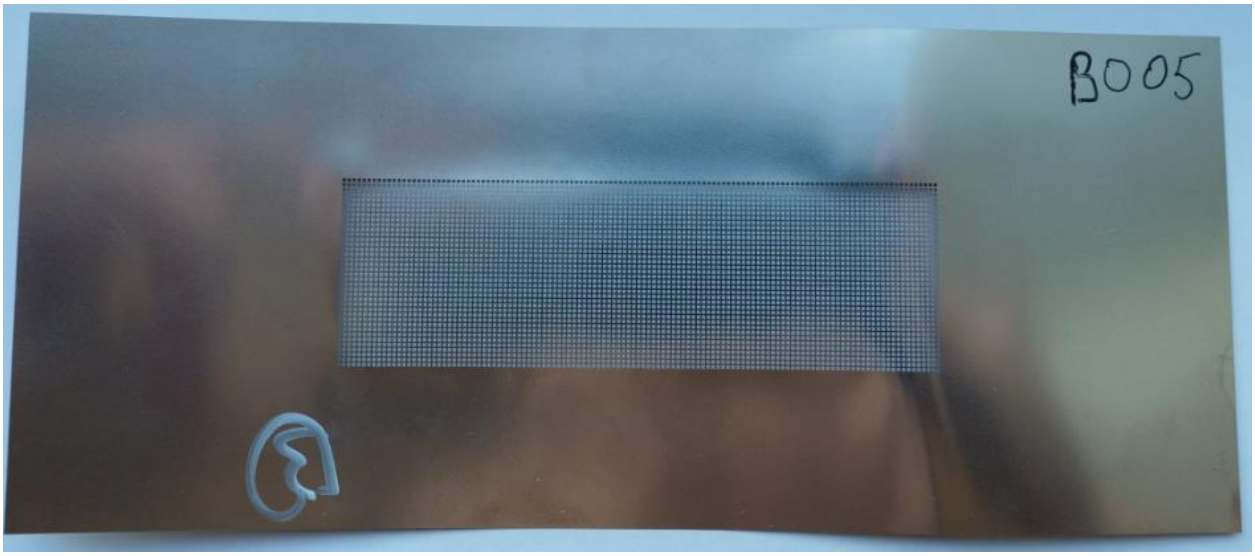

Figure A.6-2: Concept_1_0 type B005/B01

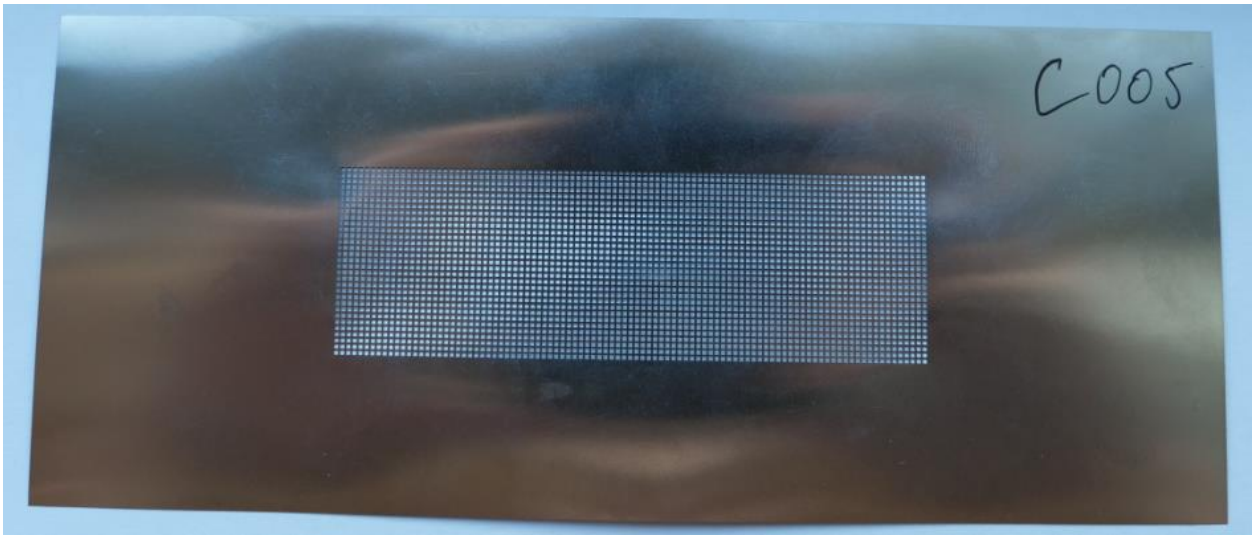

Figure A.6-3: Concept_1_0 type C005/C01

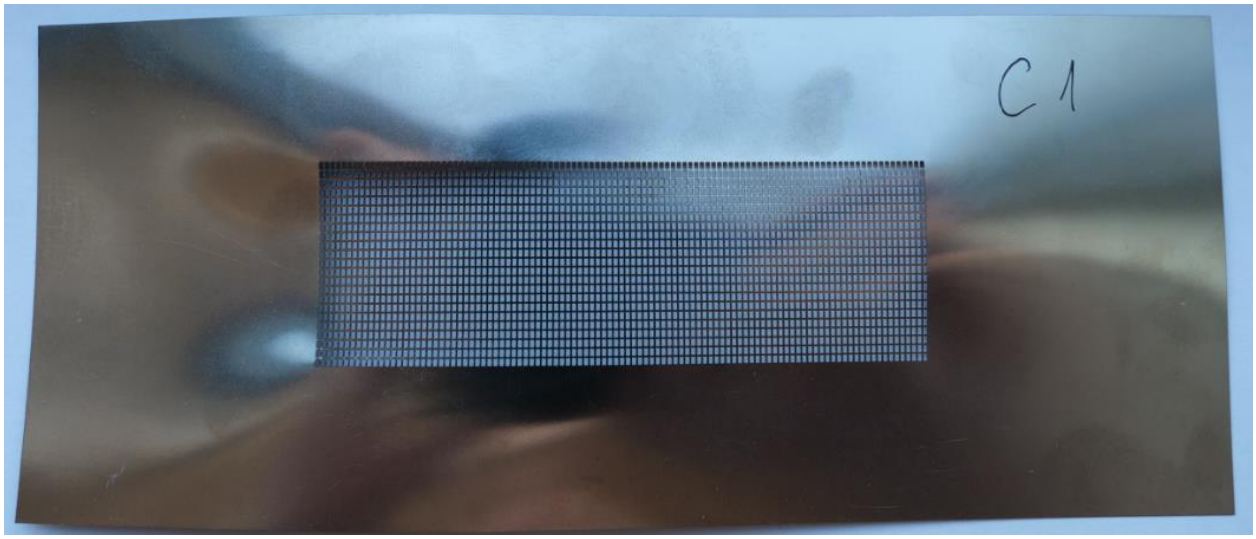

Figure A.6-4: Concept_1_1 C1

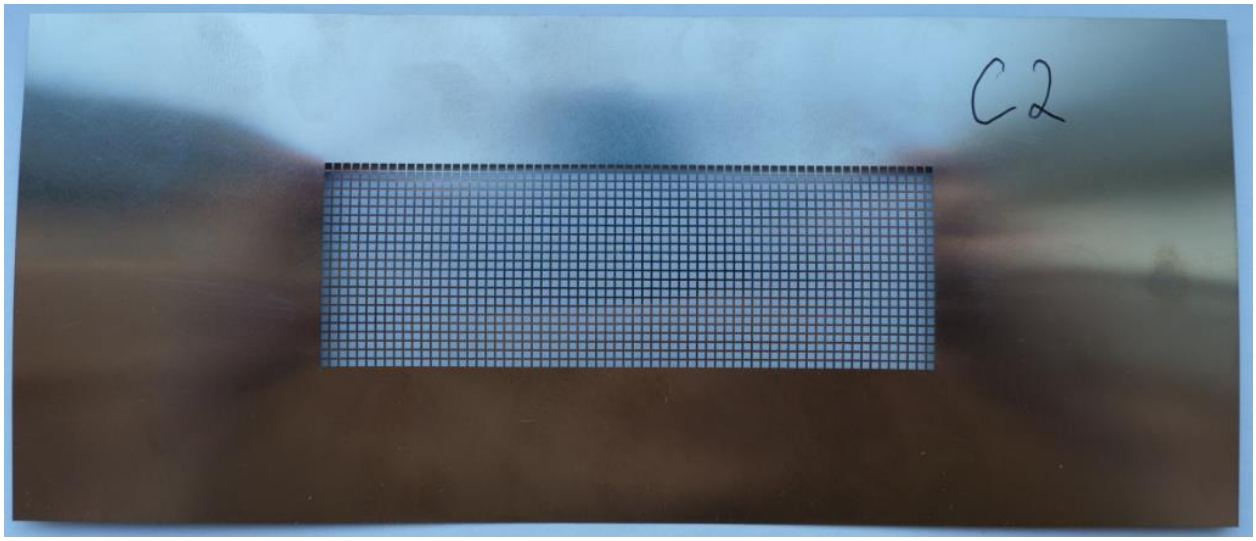

Figure A.6-5: Concept_1_1 C2

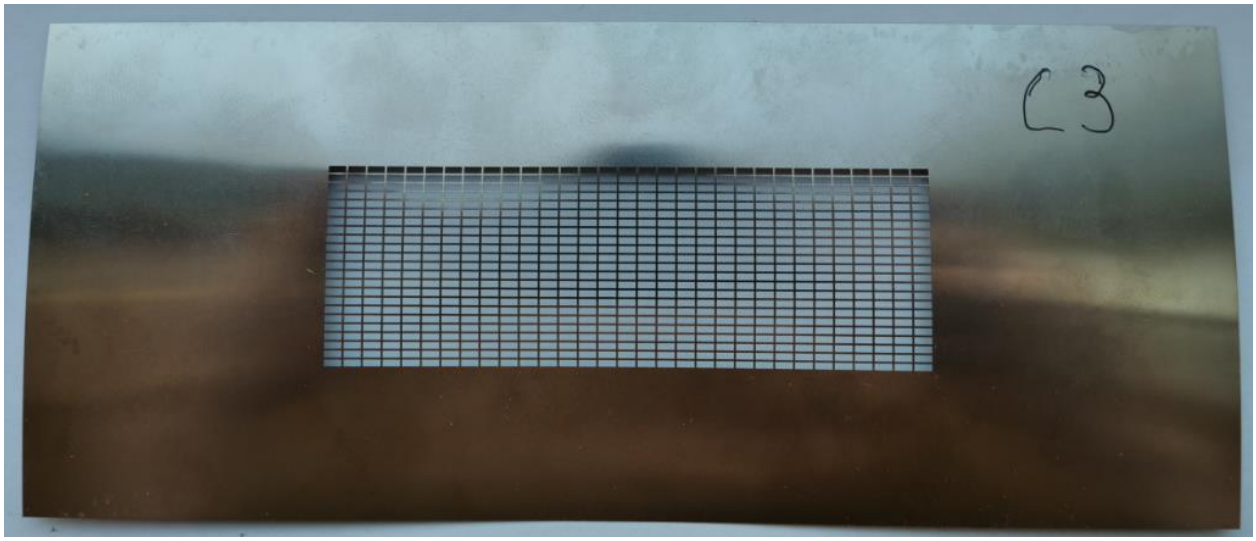

Figure A.6-6: Concept_1_1 C3

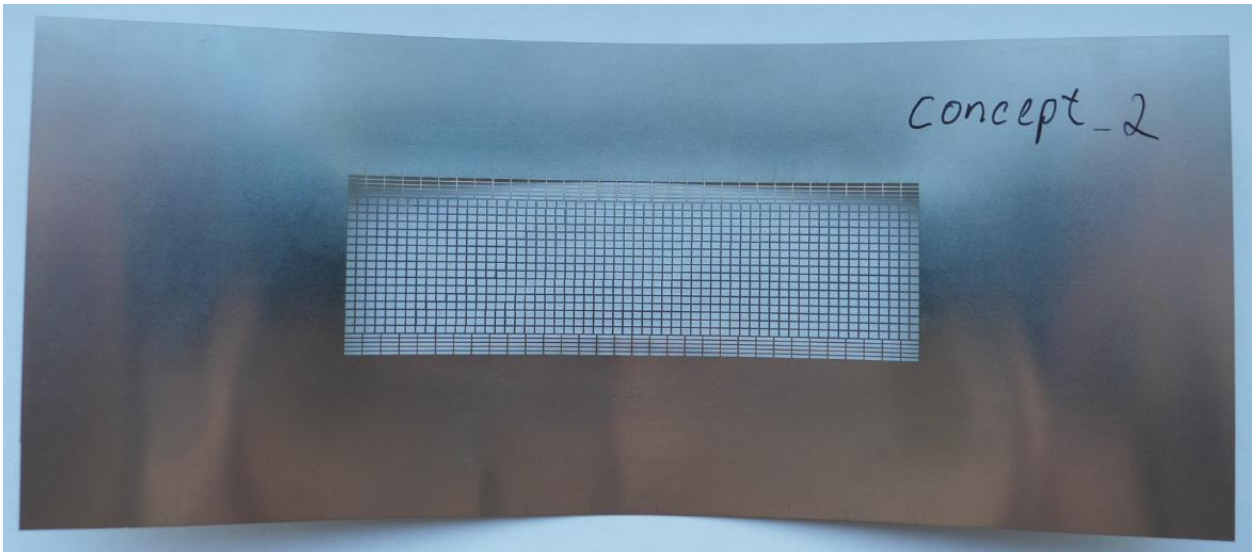

Figure A.6-7: Concept_2

A.7 JOINTS CROSS SECTION MICROSCOPIC VIEW IN THE TRANSVERSAL DIRECTION

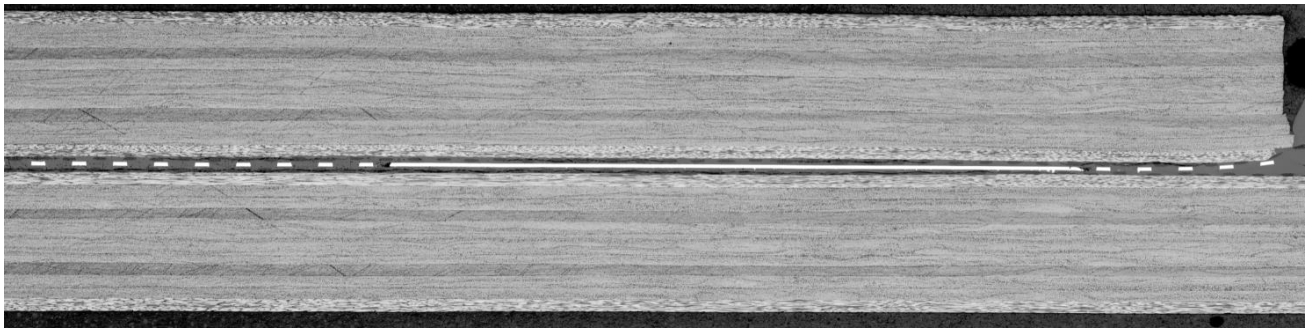

Figure A.7-1: Joint cross section microscopic view in the transversal direction of a joint welded with A005 HE

Figure A.7-2: Joint cross section microscopic view in the transversal direction of a joint welded with M200 HE

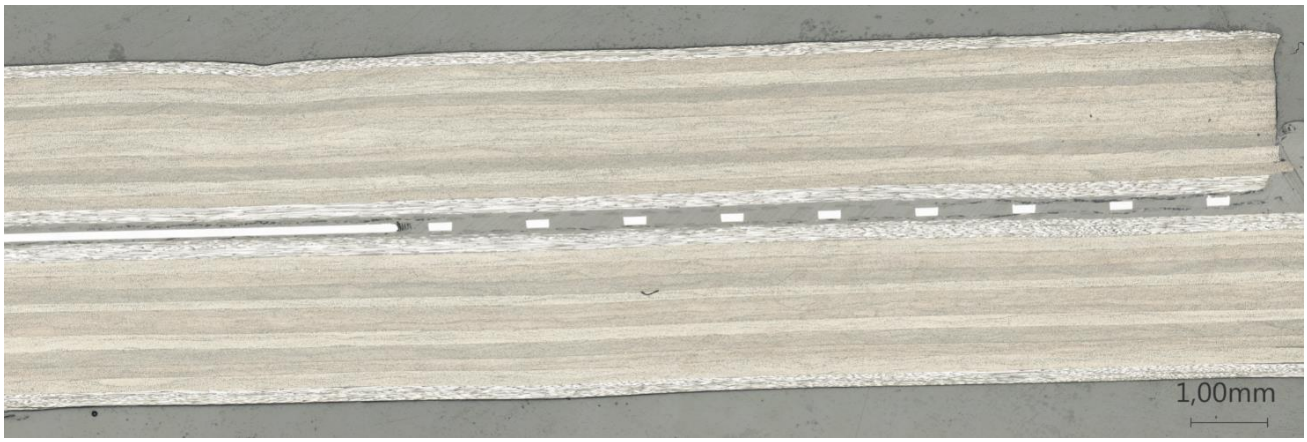

Figure A.7-3: Joint cross section microscopic view in the transversal direction of a joint welded with C1 HE

Figure A.7-4 Joint cross section microscopic view in the transversal direction of a joint welded with Concept 2 HE

A.8 MATHCAD CODE FOR M200 MESH HE MATERIAL PROPERTIES DERIVATION

Mesh HE material properties derivation for the FEM moc

AISI 304/ AISI 304L Steel properties

Temp range in degC for E_res_{steel} and k_{steel}

$$TempC := \begin{pmatrix} 20 \\ 27 \\ 77 \\ 127 \\ 227 \\ 327 \\ 427 \\ 527 \\ 627 \\ 727 \\ 827 \\ 927 \end{pmatrix}$$

Steel electrical resistivity for the temperature values in TempC

$$E\_res_{steel} := \begin{pmatrix} 71.3 \\ 71.9 \\ 76 \\ 79.8 \\ 86.8 \\ 93.3 \\ 99.2 \\ 104.3 \\ 108.6 \\ 112.5 \\ 115.8 \\ 118.7 \end{pmatrix} \cdot 10^{-8}\,\Omega\cdot m$$

Steel electrical conductivity for the temperature values in TempC

$$k_{steel} := \begin{pmatrix} 14.76 \\ 14.89 \\ 15.79 \\ 16.61 \\ 18.28 \\ 19.77 \\ 21.21 \\ 22.59 \\ 23.99 \\ 25.33 \\ 26.58 \\ 27.81 \end{pmatrix} \cdot \frac{W}{m\cdot K}$$

Temperature range in degC for Cp_{steel}

$$Temp2C := \begin{pmatrix} 0 \\ 245 \\ 500 \\ 800 \\ 1000 \end{pmatrix}$$

Steel specific heat capacity for the temperature values in Temp2C

$$Cp_{steel} := \begin{pmatrix} 460 \\ 510 \\ 500 \\ 610 \\ 660 \end{pmatrix} \cdot \frac{J}{kg\cdot K}$$

Steel mass density

$$\rho_{steel} := 7900\,\frac{kg}{m^3}$$

PEKK properties

PEKK density

$$\rho_{pekk} := 1300\,\frac{kg}{m^3}$$

PEKK conductivity

$$k_{pekk} := 0.25\,\frac{W}{m\cdot K}$$

Temperature range in degC for Cp_{pekk}

$$Temp3C := \begin{pmatrix} 20 \\ 60 \\ 100 \\ 140 \\ 180 \\ 220 \\ 260 \\ 300 \\ 320 \\ 340 \\ 360 \\ 380 \\ 400 \end{pmatrix}$$

PEKK specific heat capacity for temperature values in Temp3C

$$Cp_{pekk} := \begin{pmatrix} 1110 \\ 1110 \\ 1210 \\ 1310 \\ 1540 \\ 1660 \\ 1760 \\ 1850 \\ 2100 \\ 2870 \\ 1800 \\ 1830 \\ 1840 \end{pmatrix} \cdot \frac{J}{kg\cdot K}$$

Mesh HE geometric properties

HE width
$Width := 25.4mm$

HE Length sandwiched between the adherents
$Length := 88mm$

Gap length
$gap := 0.09mm$

Wire diameter
$d := 0.04mm$

FEM HE thickness
$th := 2.d = 0.08 \cdot mm$

Calculation of longitudinal wires number

Given
$N\_long := 3$
$N\_long \cdot (d + gap) = Width$
$N\_long := Find(N\_long)$
$N\_long := ceil(N\_long) = 196$

Calculation of transversal wires number

Given
$N\_trans := 4$
$N\_trans \cdot (gap + d) = Length$
$N\_trans := Find(N\_trans)$ $N\_trans = 676.923$
$N\_trans := ceil(N\_trans) = 677$

Mesh Open area ratio (OAR) calculation

$$OAR := 1 - \frac{(Length \cdot N\_long \cdot d) + N\_trans \cdot d \cdot (Width - N\_long \cdot d)}{Width \cdot Length} = 0.479$$

Length of the wires due to the waviness of the meshh

Length of the line conecting centers of the wires

$$c := \left[(gap + d)^2 + d^2\right]^{0.5} = 0.136 \cdot mm$$

Tangent line to two consequent circles defined by the neutral axis curvature

$$tn := \left[c^2 - \left(2 \cdot \frac{3d}{4}\right)^2\right]^{0.5} = 0.122 \cdot mm$$

Angle between circle distance and tangent

$$\gamma := asin\left(\frac{3d}{4} \cdot \frac{2}{c}\right) = 0.457$$

Angle between center line and horizontal line

$$\beta := atan\left(\frac{d}{gap + d}\right) = 0.298$$

Angle between tangent and vertical line

$$\alpha := (\gamma + \beta) = 0.755$$

Circle arc length

$$l_{arc} := 2\pi \cdot 3 \frac{d}{4} \cdot \frac{\alpha}{2\pi} = 0.023 \cdot mm$$

Longitudinal wire width between 2 transversal wires and vice versa

$$l := 2 \cdot l_{arc} + tn = 0.167 \cdot mm$$

One longitdinal wire length One transversal wire length

$Ll := l \cdot N\_trans = 0.113\ m$ $Lt := l \cdot N\_long = 0.033\ m$

Stainless steel Mesh volume

$$Vol_{mesh} := Ll \cdot N\_long \cdot \pi \left(\frac{d}{2}\right)^2 + Lt \cdot N\_trans \cdot \pi \left(\frac{d}{2}\right)^2 = 5.582 \times 10^{-5} \cdot L$$

PEKK volume in the modelled HE

$Vol_{pekk} := Width \cdot Length \cdot th - Vol_{mesh} = 1.23 \times 10^{-4} L$ c

Equivalent desnity of the modeled Mesh HE inside the wedling stack

$$\rho_{mesh\_eq\_ws} := \frac{\left(\rho_{pekk} \cdot Vol_{pekk} + \rho_{steel} \cdot Vol_{mesh}\right)}{Width \cdot Length \cdot th} = 3.36 \times 10^3 \frac{kg}{m^3}$$

Equivalent desnity of the modeled Mesh HE out of the wedling stack

$$\rho_{mesh\_eq\_ows} := \frac{\rho_{steel} \cdot Vol_{mesh}}{Width \cdot Length \cdot th} = 2.466 \times 10^3 \frac{kg}{m^3}$$

Temperature dependent specific heat capacity of the modeled Mesh HE inside the welding stack

Steel volume fraction of the FEM modeled HE inside the welding stack

$$\nu_{steel\_mesh\_eq} := \frac{Vol_{mesh}}{th \cdot Length \cdot Width} = 0.312$$

Temperature range x= (firts vaue, second value..last value) $x := 20, 40 .. 440$

$$c_{mesh\_eq\_ws}(x) := \frac{\rho_{steel} \cdot \left(\nu_{steel\_mesh\_eq}\right) \cdot linterp\left(Temp2C, Cp_{steel}, x\right) \ldots + \rho_{pekk} \cdot \left(1 - \nu_{steel\_mesh\_eq}\right) linterp\left(Temp3C, Cp_{pekk}, x\right)}{\rho_{mesh\_eq\_ws}}$$

$i := 0, 1 .. \frac{440}{20}$ $Cp_{mesh\_eq\_ws_{0,i}} := i \cdot 20 + 20$

$$Cp_{mesh\_eq\_ws_{1,i}} := c_{mesh\_eq\_ws}[(i+1) \cdot 20] \cdot \left(\frac{J}{kg \cdot K}\right)^{-1}$$

Resulted specific heat capacity

$Cp_{mesh\_eq\_ws} =$

20	40	60	80	100
635.956	638.952	641.948	658.248	...

T [C]
Cp [J/kg*C]

Temperature dependent specific heat capacity of the modeled Mesh HE outside the welding stack

$$c_{mesh\_eq\_ows}(x) := \frac{\rho_{steel} \cdot \left(\nu_{steel\_mesh\_eq}\right) \cdot linterp\left(Temp2C, Cp_{steel}, x\right)}{\rho_{mesh\_eq\_ows}}$$

$i := 0, 1 .. \frac{440}{20}$ $Cp_{mesh\_eq\_ows_{0,i}} := i \cdot 20 + 20$

$$Cp_{mesh\_eq\_ows_{1,i}} := c_{mesh\_eq\_ows}[(i+1)\cdot 20]\cdot\left(\frac{J}{kg\cdot K}\right)^{-1}$$

$Cp_{mesh\_eq\_ows} =$	20	40	60	80	100	120
	464.082	468.163	472.245	476.327	480.408	...

T [C]
Cp [J/kg*C]

Thermal conductivity of the modeled Mesh HE inside the welding stack

Volume fraction of constituents

$\nu_{steel\_mesh\_eq} = 0.312$

$\nu_{pekk\_mesh\_eq} := 1 - \nu_{steel\_mesh\_eq}$

Interpolated conductivity of steel

$k_{steel}(x) := linterp(TempC, k_{steel}, x)$

Through thickness thermal conductivity of the modelled heating element

$ky(x) := \nu_{steel\_mesh\_eq}\cdot k_{steel}(x) + \left(1 - \nu_{steel\_mesh\_eq}\right)k_{pekk}$

Inplane thermal conductivity

$$kx1(x) := k_{pekk}\cdot\left(\nu_{pekk\_mesh\_eq}\right)^{0.5} + k_{steel}(x)\cdot\left[1 - \left(\nu_{pekk\_mesh\_eq}\right)^{0.5}\right]$$

$$kx(x) := \left[\frac{\nu_{pekk\_mesh\_eq}^{0.5}}{kx1(x)} + \frac{1 - \left(\nu_{pekk\_mesh\_eq}\right)^{0.5}}{k_{steel}(x)}\right]^{-1}$$

$i := 0, 1 .. \frac{440}{20}$ $K_{mesh\_eq\_ws_{0,i}} := i\cdot 20 + 20$

$$K_{mesh\_eq\_ws_{2,i}} := ky[(i+1)\cdot 20]\cdot\left(\frac{W}{m\cdot K}\right)^{-1} \quad K_{mesh\_eq\_ws_{1,i}} := kx[(i+1)\cdot 20]\cdot\left(\frac{W}{m\cdot K}\right)^{-1}$$

$K_{mesh\_eq\_ws} =$	20	40	60	80	100	120	140
	3.167	3.239	3.311	3.381	3.446	3.512	3.578
	4.78	4.893	5.006	5.117	5.219	5.321	...

T [C]
kx[W/m*C]
ky[W/m*C]

Calculation of the equivalent conductivity of the modelled heating element

$E\_res_{steel}(x) := linterp(TempC, E\_res_{steel}, x)$

Total resistance of the plate assuming that only longitudinal wires are conductive

$$R(x) := E\_res_{steel}(x)\cdot\frac{Length}{\pi\cdot\left(\frac{d}{2}\right)^2\cdot N\_long}$$

Equivalent resistivity of the modelled Heating element

$$E\_res_{mesh.eq}(x) := \frac{R(x)\cdot Width\cdot th}{Length}$$

Temperature range $x := 20, 60 .. 520$

echivalent conductivity

$\sigma_{eq_{0,i}} := i \cdot 20 + 20$ $\sigma_{eq_{1,i}} := \frac{1}{E\_res_{mesh.eq}[(i+1)\cdot 20]} \cdot \left(\frac{1}{ohm \cdot m}\right)^{-1}$

$\sigma_{eq} =$

20	40	60	80	100	120
$1.7 \cdot 10^5$	$1.661 \cdot 10^5$	$1.625 \cdot 10^5$	$1.59 \cdot 10^5$	$1.559 \cdot 10^5$	...

T [C]

σ [1/(ohm*m)]

Curent intensity calculation:

Given

$I := 2A$

Introduce desired power per surface at the welding interface

$P_s := 51 \frac{kW}{m^2}$

$P_s = \frac{I^2 \cdot R(22)}{Width \cdot Length}$

$I := Find(I)$

$I = 21.129\,A$

Current per surface input for FEM

$I_s := \frac{I}{Width \cdot th} = 1.039788426 \times 10^7 \frac{A}{m^2}$

Power generation at the welding interface in fuction of the temperature on the welding interface

$P_{0,i} := i \cdot 20 + 20$ $P_{s_{1,i}} := \frac{I^2 \cdot R[(i+1)\cdot 20]}{Width \cdot Length} \cdot \left(\frac{kW}{m^2}\right)^{-1}$

$P_s =$

20	40	60	80	100	120	140
50.878	52.066	53.237	54.394	55.479	56.563	...

T [C]

P [kW/m^2)

A.9 MATHCAD CODE FOR CONCEPT_1_0 AND CONCEPT_1_1 HE MATERIAL PROPERTIES DERIVATION

Plate HE material properties derivation for the FEM mode

AISI 304/ AISI 304L Steel properties

Temp range in degC for E_res_{steel} and k_{steel}

$$TempC := \begin{pmatrix} 20 \\ 27 \\ 77 \\ 127 \\ 227 \\ 327 \\ 427 \\ 527 \\ 627 \\ 727 \\ 827 \\ 927 \end{pmatrix}$$

Steel electrical resistivity for the temperature values in TempC

$$E\_res_{steel} := \begin{pmatrix} 71.3 \\ 71.9 \\ 76 \\ 79.8 \\ 86.8 \\ 93.3 \\ 99.2 \\ 104.3 \\ 108.6 \\ 112.5 \\ 115.8 \\ 118.7 \end{pmatrix} \cdot 10^{-8}\,\Omega\cdot m$$

Steel electrical conductivity for the temperature values in TempC

$$k_{steel} := \begin{pmatrix} 14.76 \\ 14.89 \\ 15.79 \\ 16.61 \\ 18.28 \\ 19.77 \\ 21.21 \\ 22.59 \\ 23.99 \\ 25.33 \\ 26.58 \\ 27.81 \end{pmatrix} \cdot \frac{W}{m\cdot K}$$

Temperature range in degC for Cp_{steel}

$$Temp2C := \begin{pmatrix} 0 \\ 245 \\ 500 \\ 800 \\ 1000 \end{pmatrix}$$

Steel specific heat capacity for the temperature values in Temp2C

$$Cp_{steel} := \begin{pmatrix} 460 \\ 510 \\ 500 \\ 610 \\ 660 \end{pmatrix} \cdot \frac{J}{kg\cdot K}$$

Steel mass density

$$\rho_{steel} := 7900\,\frac{kg}{m^3}$$

PEKK properties

PEKK conductivity

$$k_{pekk} := 0.25\,\frac{W}{m\cdot K}$$

PEKK density

$$\rho_{pekk} := 1300\,\frac{kg}{m^3}$$

Temperature range in degC for Cp_{pekk}

$$Temp3C := \begin{pmatrix} 20 \\ 60 \\ 100 \\ 140 \\ 180 \\ 220 \\ 260 \\ 300 \\ 320 \\ 340 \\ 360 \\ 380 \\ 400 \end{pmatrix}$$

PEKK specific heat capacity for the temperature values in Temp3C

$$Cp_{pekk} := \begin{pmatrix} 1110 \\ 1110 \\ 1210 \\ 1310 \\ 1540 \\ 1660 \\ 1760 \\ 1850 \\ 2100 \\ 2870 \\ 1800 \\ 1830 \\ 1840 \end{pmatrix} \cdot \frac{J}{kg\cdot K}$$

Plate HE geometric properties

HE width

Width := 25.4mm

Length of the welding interface (perforated interface)

Length := 88mm

HE thickness

th := 0.1mm

Gap dimesnions

Gap length

gap_l := 0.5mm

Path dimension

Longitudinal path width

w_l := 0.24mm

Gap width

gap_w := 0.5mm

Transversal path width

w_t := 0.24mm

Number of longitudinal conductive paths

Given

N_long := 3

(N_long)·(gap_w + w_l) = Width

N_long := Find(N_long)

N_long = 34.324

N_long := ceil(N_long) = 35

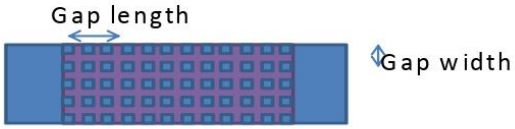

Number of transversal paths

Given

N_trans := 4

(N_trans)·(gap_l + w_t) + gap_l = Length

N_trans := Find(N_trans)

N_trans = 118.243

N_trans := ceil(N_trans) = 119

N_trans := 118

Resulted length of the tailore region

L_R := N_trans·(w_t + gap_l) + gap_w = 87.82·mm

Resulted width of tailored region

W_R := N_long·(w_t + gap_l) = 25.9·mm

Open area ratio

$$OAR := \frac{gap\_l \cdot (N\_trans + 1) \cdot gap\_w \cdot (N\_long)}{Length \cdot Width} = 0.466$$

HE density in the welding stack

$$\rho_{plate\_qe\_ws} := OAR \cdot \rho_{pekk} + (1 - OAR) \cdot \rho_{steel} = 4.825 \times 10^3 \frac{kg}{m^3}$$

Temperature dependent specific heat capacity of the modeled Mesh HE inside the welding stack

Temperature range x= (firts vaue, second value..last value) $x := 20, 40 .. 440$

$$c_{plate\_eq\_ws}(x) := \frac{\rho_{steel} \cdot (1 - OAR) \cdot linterp(Temp2C, Cp_{steel}, x) \ldots + \rho_{pekk} \cdot (OAR)\, linterp(Temp3C, Cp_{pekk}, x)}{\rho_{plate\_qe\_ws}}$$

$i := 0, 1 .. \frac{440}{20}$ $Cp_{plate\_eq\_ws_{0,i}} := i \cdot 20 + 20$

$Cp_{plate\_eq\_ws_{1,i}} := c_{plate\_eq\_ws}[(i+1)\cdot 20] \cdot \left(\frac{J}{kg \cdot K}\right)^{-1}$

Resulted specific heat capacity

$Cp_{plate\_eq\_ws} =$

20	40	60	80	100
545.145	548.714	552.283	562.128	...

T [C]
Cp [J/kg*C]

Thermal conductivity of the modeled Mesh HE inside the welding stack

Volume fraction of constituents

$\nu_{steel\_plate\_eq} := 1 - OAR = 0.534$

$\nu_{pekk\_plate\_eq} := OAR = 0.466$

Interpolated conductivity of steel

$k_{steel}(x) := linterp(TempC, k_{steel}, x)$

Through thickness thermal conductivity of the modelled heating element

$ky(x) := \nu_{steel\_plate\_eq} \cdot k_{steel}(x) + (\nu_{pekk\_plate\_eq}) k_{pekk}$

Through thickness thermal conductivity of the modelled heating element

$ky(x) := \nu_{steel\_plate\_eq} \cdot k_{steel}(x) + \nu_{pekk\_plate\_eq} k_{pekk}$

Inplane thermal conductivity

$kx1(x) := k_{pekk} \cdot (\nu_{pekk\_plate\_eq})^{0.5} + k_{steel}(x) \cdot \left[1 - (\nu_{pekk\_plate\_eq})^{0.5}\right]$

$kx(x) := \left[\frac{\nu_{pekk\_plate\_eq}^{0.5}}{kx1(x)} + \frac{1 - (\nu_{pekk\_plate\_eq})^{0.5}}{k_{steel}(x)}\right]^{-1}$

$i := 0, 1 .. \frac{440}{20}$ $K_{mesh\_eq\_ws_{0,i}} := i \cdot 20 + 20$

$K_{mesh\_eq\_ws_{2,i}} := ky[(i+1)\cdot 20] \cdot \left(\frac{W}{m \cdot K}\right)^{-1}$ $K_{mesh\_eq\_ws_{1,i}} := kx[(i+1)\cdot 20] \cdot \left(\frac{W}{m \cdot K}\right)^{-1}$

$K_{mesh\_eq\_ws} =$

	0	1	2	3	4	5	6
0	20	40	60	80	100	120	140
1	6.171	6.319	6.465	6.609	6.741	6.874	7.009
2	8.001	8.195	8.387	8.577	8.752	8.928	...

kx[W/m*C]
ky[W/m*C]

Calculation of the equivalent conductivity of the modelled heating element

$E\_res_{steel}(x) := linterp(TempC, E\_res_{steel}, x)$

Total resistance of the plate assuming that only longitudinal wires are conductive

$R(x) := E\_res_{steel}(x) \cdot \frac{Length}{th \cdot w\_l \cdot N\_long}$

Equivalent resistivity of the modelled Heating element

$$E\_res_{mesh.eq}(x) := \frac{R(x)\cdot Width\cdot th}{Length}$$

Temperature range $x := 20, 60 .. 520$

echivalent conductivity

$$\sigma_{eq_{0,i}} := i\cdot 20 + 20 \qquad \sigma_{eq_{1,i}} := \frac{1}{E\_res_{mesh.eq}[(i+1)\cdot 20]}\cdot\left(\frac{1}{ohm\cdot m}\right)^{-1}$$

σ_{eq} =		0	1	2	3	4
	0	20	40	60	80	100
	1	$4.638\cdot 10^5$	$4.532\cdot 10^5$	$4.433\cdot 10^5$	$4.338\cdot 10^5$	...

T [C]

σ [1/(ohm*m)]

Curent intensity calculation:

Given

$I := 2A$

Introduce desired power per surface at the welding interface

$$P_s := 71.4\frac{kW}{m^2}$$

$$P_s = \frac{I^2\cdot R(22)}{Width\cdot Length}$$

Current per surface input for FEM

$$I_s := \frac{I}{Width\cdot th} = 1.817630741\times 10^7\frac{A}{m^2}$$

$I := Find(I)$

$I = 46.168\,A$

Power generation at the welding interface in fuction of the temperature on the welding interface

$$P_{s_{0,i}} := i\cdot 20 + 20 \qquad P_{s_{1,i}} := \frac{I^2\cdot R[(i+1)\cdot 20]}{Width\cdot Length}\cdot\left(\frac{kW}{m^2}\right)^{-1}$$

P_s =	20	40	60	80	100	120
	71.229	72.893	74.531	76.152	77.67	...

T [C]

P [kW/m^2)]

Power per surface generation in the uncovered area

$$P_{so}(x) := I^2\frac{E\_res_{steel}[(i+1)\cdot 20]}{Width^2\cdot th}$$

$$P_{so_{0,i}} := i\cdot 20 + 20 \qquad P_{so_{1,i}} := I^2\frac{E\_res_{steel}[(i+1)\cdot 20]}{Width^2\cdot th}\cdot\left(\frac{kW}{m^2}\right)^{-1}$$

P_{so} =	20	40	60	80	100
	23.556	24.106	24.648	25.184	...

T [C]

P [kW/m^2)]

A.10 MATHCAD CODE FOR CONCEPT_2 HE MATERIAL PROPERTIES DERIVATION

Plate HE material properties derivation for the FEM mode

AISI 304/ AISI 304L Steel properties

Temp range in degC for E_res_{steel} and k_{steel}

$$TempC := \begin{pmatrix} 20 \\ 27 \\ 77 \\ 127 \\ 227 \\ 327 \\ 427 \\ 527 \\ 627 \\ 727 \\ 827 \\ 927 \end{pmatrix}$$

Steel electrical resistivity for the temperature values in TempC

$$E\_res_{steel} := \begin{pmatrix} 71.3 \\ 71.9 \\ 76 \\ 79.8 \\ 86.8 \\ 93.3 \\ 99.2 \\ 104.3 \\ 108.6 \\ 112.5 \\ 115.8 \\ 118.7 \end{pmatrix} \cdot 10^{-8}\ \Omega \cdot m$$

Steel electrical conductivity for the temperature values in TempC

$$k_{steel} := \begin{pmatrix} 14.76 \\ 14.89 \\ 15.79 \\ 16.61 \\ 18.28 \\ 19.77 \\ 21.21 \\ 22.59 \\ 23.99 \\ 25.33 \\ 26.58 \\ 27.81 \end{pmatrix} \cdot \frac{W}{m \cdot K}$$

Temperature range in degC for Cp_{steel}

$$Temp2C := \begin{pmatrix} 0 \\ 245 \\ 500 \\ 800 \\ 1000 \end{pmatrix}$$

Steel specific heat capacity for the temperature values in Temp2C

$$Cp_{steel} := \begin{pmatrix} 460 \\ 510 \\ 500 \\ 610 \\ 660 \end{pmatrix} \cdot \frac{J}{kg \cdot K}$$

Steel mass density

$$\rho_{steel} := 7900 \frac{kg}{m^3}$$

PEKK properties

PEKK conductivity

$$k_{pekk} := 0.25 \frac{W}{m \cdot K}$$

PEKK density

$$\rho_{pekk} := 1300 \frac{kg}{m^3}$$

Temperature range in degC for Cp_{pekk}

$$Temp3C := \begin{pmatrix} 20 \\ 60 \\ 100 \\ 140 \\ 180 \\ 220 \\ 260 \\ 300 \\ 320 \\ 340 \\ 360 \\ 380 \\ 400 \end{pmatrix}$$

PEKK specific heat capacity for the temperature values in Temp3C

$$Cp_{pekk} := \begin{pmatrix} 1110 \\ 1110 \\ 1210 \\ 1310 \\ 1540 \\ 1660 \\ 1760 \\ 1850 \\ 2100 \\ 2870 \\ 1800 \\ 1830 \\ 1840 \end{pmatrix} \cdot \frac{J}{kg \cdot K}$$

HE properties Region 4

Region 4 width

Width4 := 21mm

Length of the welding interface (tailored interface)

Length := 88mm

Total HE width

Width_t := 25.4mm

HE thickness

th := 0.1mm

Desired material width zone1

M4 := 4.34mm

gap of the mesh

gap_l4 := 1.28mm

gap_w4 := 0.982mm

longitudinal wire width

w_l4 := 0.24mm

transversal wire width

w_t4 := 0.24mm

Number of longitudinal wires region 1

$$N\_long4 := \frac{M4}{w\_l4} = 18.083$$

Given

N_long4 := 3

(N_long4)·(gap_w4 + w_l4) − gap_w4 = Width4

N_long4 := Find(N_long4)

N_long4 = 17.989

N_long4 := ceil(N_long4) = 18

N_long4 := 18

Number of transversal wires region 4

Given

N_trans4 := 4

(N_trans4)·(gap_l4 + w_t4) + gap_l4 = Length

N_trans4 := Find(N_trans4)

N_trans4 = 57.053

N_trans4 := 57

ReWidth4 := (N_long4)·(gap_w4 + w_l4) − gap_w4 = 21.014·mm

ReLength4 := (N_trans4)·(gap_l4 + w_t4) + gap_l4 = 87.92·mm

Region3

Desired material width zone3

M3 := 0.608mm

gap_l3 := 2.55mm

gap_w3 := 0.456mm

w_l3 := 0.205mm

w_t3 := 0.205mm

$$Width3 := \frac{Width\_t - ReWidth4}{2} - 0.5gap\_w3 = 1.965\cdot mm$$

Calculculuso f the wires number longitudinal and transversal

$$N\_long3 := \frac{M3}{w\_l3} = 2.966$$

Given

$N\_long3 := 3$

$(N\_long3)\cdot(gap\_w3 + w\_t3) = Width3$

$N\_long3 := Find(N\_long3)$

$N\_long3 = 2.973$

$N\_long3 := ceil(N\_long3) = 3$

Given

$N\_trans3 := 4$

$(N\_trans3)\cdot(gap\_l3 + w\_t3) + gap\_l3 = Length$

$N\_trans3 := Find(N\_trans3)$

$N\_trans3 = 31.016$

$N\_trans3 := ceil(N\_trans3) = 32$

$N\_trans3 := 31$

$ReWidth3 := (N\_long3)\cdot(gap\_w3 + w\_l3) = 1.983\cdot mm$

$ReLength3 := (N\_trans3)\cdot(gap\_l3 + w\_t3) + gap\_l3 = 87.955\cdot mm$

$ReWidth := ReWidth4 + gap\_w3 + 2(ReWidth3) = 25.436\cdot mm$

OAR region 4

$$OAR4 := \frac{[gap\_w4\cdot(N\_long4 - 1)]\cdot gap\_l4\cdot(N\_trans4 + 1)}{Length\cdot(ReWidth4 + gap\_w3)} = 0.656$$

OAR region 3

$$OAR3 := \frac{(N\_long3)\cdot gap\_w3\cdot[gap\_l3\cdot(N\_trans3 + 1)]}{Length\cdot(ReWidth3)} = 0.64$$

Thermal properties

$$OAR_{str4} := \frac{gap\_l4\cdot N\_trans4\cdot gap\_w4}{gap\_w4\cdot Length} = 0.829 \qquad OAR_{str3} := \frac{gap\_l3\cdot N\_trans3\cdot gap\_w3}{gap\_w3\cdot Length} = 0.898$$

Strip density region 1

$$\rho_{strip4} := OAR_{str4}\cdot\rho_{pekk} + \left(1 - OAR_{str4}\right)\cdot\rho_{steel} = 2.428 \times 10^{3}\ \frac{kg}{m^3}$$

Strip specific heat capacity region1

Temperature range x= (firts vaue, second value..last value) $x := 20, 40 .. 440$

$$c_{strip4}(x) := \frac{\rho_{steel}\cdot\left(1 - OAR_{str4}\right)\cdot linterp\left(Temp2C, Cp_{steel}, x\right) \ldots + \rho_{pekk}\cdot\left(OAR_{str4}\right) linterp\left(Temp3C, Cp_{pekk}, x\right)}{\rho_{strip4}}$$

$$i := 0, 1 .. \frac{440}{20} \quad Cp_{strip4_{0,i}} := i\cdot 20 + 20$$

$$Cp_{strip4_{1,i}} := c_{strip4}[(i + 1)\cdot 20]\cdot\left(\frac{J}{kg\cdot K}\right)^{-1}$$

Resulted specific heat capacity strip region 4

$Cp_{strip4} =$

	0	1	2	3	4
0	20	40	60	80	100
1	750.813	753.082	755.352	779.817	...

T [C]
Cp [J/kg*C]

Strip density region 3

$$\rho_{strip3} := OAR_{str3}\cdot\rho_{pekk} + \left(1 - OAR_{str3}\right)\cdot\rho_{steel} = 1.971 \times 10^3 \frac{kg}{m^3}$$

Strip specific heat capacity region 3

Temperature range x= (firts vaue, second value..last value)

$$c_{strip3}(x) := \frac{\rho_{steel}\cdot\left(1 - OAR_{str3}\right)\cdot linterp\left(Temp2C, Cp_{steel}, x\right) \ldots + \rho_{pekk}\cdot\left(OAR_{str3}\right) linterp\left(Temp3C, Cp_{pekk}, x\right)}{\rho_{strip3}}$$

$$i := 0, 1 .. \frac{440}{20} \quad Cp_{strip3_{0,i}} := i\cdot 20 + 20$$

$$Cp_{strip3_{1,i}} := c_{strip3}[(i + 1)\cdot 20]\cdot\left(\frac{J}{kg\cdot K}\right)^{-1}$$

Resulted specific heat capacity strip region 3

$Cp_{strip3} =$

	0	1	2	3	4
0	20	40	60	80	100
1	846.729	848.392	850.056	881.34	...

T [C]
Cp [J/kg*C]

Thermal conductivity strip 4

Interpolated conductivity of steel

$$k_{steel}(x) := linterp\left(TempC, k_{steel}, x\right)$$

$$kyz4(x) := \left(1 - OAR_{str4}\right)\cdot k_{steel}(x) + \left(OAR_{str4}\right)k_{pekk}$$

$$kx4(x) := \left(\frac{OAR_{str4}}{k_{pekk}} + \frac{1 - OAR_{str4}}{k_{steel}(x)} \right)^{-1}$$

$$i := 0, 1 .. \frac{440}{20} \quad K_{strip4_{0,i}} := i \cdot 20 + 20$$

$$K_{strip4_{2,i}} := kyz4[(i + 1) \cdot 20] \cdot \left(\frac{W}{m \cdot K} \right)^{-1} \qquad K_{strip4_{1,i}} := kx4[(i + 1) \cdot 20] \cdot \left(\frac{W}{m \cdot K} \right)^{-1}$$

$K_{strip4} =$

	0	1	2	3	4	5	6	
0	20	40	60	80	100	120	140	T [C]
1	0.3	0.301	0.301	0.301	0.301	0.301	0.301	kx[W/m*C]
2	2.73	2.792	2.854	2.914	2.97	3.026	...	kyz[W/m*C]

Thermal conductivity strip 3

$$kyz3(x) := (1 - OAR_{str3}) \cdot k_{steel}(x) + (OAR_{str3}) k_{pekk}$$

$$kx3(x) := \left(\frac{OAR_{str3}}{k_{pekk}} + \frac{1 - OAR_{str3}}{k_{steel}(x)} \right)^{-1}$$

$$i := 0, 1 .. \frac{440}{20} \quad K_{strip3_{0,i}} := i \cdot 20 + 20$$

$$K_{strip3_{2,i}} := kyz3[(i + 1) \cdot 20] \cdot \left(\frac{W}{m \cdot K} \right)^{-1} \qquad K_{strip3_{1,i}} := kx3[(i + 1) \cdot 20] \cdot \left(\frac{W}{m \cdot K} \right)^{-1}$$

$K_{strip3} =$

	0	1	2	3	4	5	6	
0	20	40	60	80	100	120	140	T [C]
1	0.278	0.278	0.278	0.278	0.278	0.278	0.278	kx[W/m*C]
2	1.726	1.763	1.799	1.835	1.869	1.902	...	kyz[W/m*C]

Calculation of the equivalent conductivity of the modelled heating element

$$E\_res_{steel}(x) := linterp(TempC, E\_res_{steel}, x)$$

Strip4

$$\sigma_{strip4}(x) := \frac{w\_t4 \cdot N\_trans4}{E\_res_{steel}(x) \cdot Length}$$

eq conductivity strip 4

$$\sigma_{strip4_{1,i}} := \sigma_{strip4}[(i + 1) \cdot 20] \cdot \left(\frac{1}{ohm \cdot m} \right)^{-1} \qquad \sigma_{strip4_{0,i}} := i \cdot 20 + 20$$

$\sigma_{strip4} =$

	0	1	2	3	4	
0	20	40	60	80	100	T [C]
1	$2.18 \cdot 10^5$	$2.131 \cdot 10^5$	$2.084 \cdot 10^5$	$2.039 \cdot 10^5$	...	σ [1/(ohm*m)]

Strip3

$$\sigma_{strip3}(x) := \frac{w\_t3 \cdot N\_trans3}{E\_res_{steel}(x) \cdot Length}$$

$$\sigma_{strip3}{}_{1,i} := \sigma_{strip3}[(i+1)\cdot 20] \cdot \left(\frac{1}{ohm \cdot m}\right)^{-1} \qquad \sigma_{strip3}{}_{0,i} := i \cdot 20 + 20$$

$\sigma_{strip3} =$

	0	1	2	3	4	
0	20	40	60	80	100	T [C]
1	$1.013 \cdot 10^5$	$9.897 \cdot 10^4$	$9.68 \cdot 10^4$	$9.474 \cdot 10^4$	...	σ [1/(ohm*m)]

Curent intensity calculation:

Resistance of Region1

$$R4(x) := \frac{E\_res_{steel}(x) \cdot \frac{Length}{th \cdot w\_l4}}{N\_long4}$$

Resitace of Region 2

$$R3(x) := \frac{E\_res_{steel}(x) \cdot \frac{Length}{th \cdot w\_l3}}{N\_long3}$$

Total Resitance of the tailored region ar RT

$$Rt := \left(\frac{2 \cdot R4(22) + R3(22)}{R3(22) \cdot R4(22)}\right)^{-1} = 0.113\,\Omega$$

Given

$I := 39A \quad I4 := 1A \quad I3 := 2A$

$I4 + 2 \cdot I3 = I$

$$I4 = I \cdot \frac{Rt}{R4(22)}$$

$$\begin{pmatrix} I4 \\ I3 \end{pmatrix} := Find(I4, I3)$$

$$\begin{pmatrix} I4 \\ I3 \\ I \end{pmatrix} = \begin{pmatrix} 30.357 \\ 4.322 \\ 39 \end{pmatrix} A$$

Zone4

$$Ps4 := \frac{I4^2 \cdot R4(22)}{(ReWidth4 + gap\_w3) \cdot Length} = \blacksquare \cdot \frac{kW}{m^2}$$

$$Ps3 := \frac{I3^2 \cdot R3(22)}{\left[\frac{Width\_t - (ReWidth4 + gap\_w3)}{2}\right] \cdot Length} = 110.456 \cdot \frac{kW}{m^2}$$

$$Ps3(x) := \frac{I^2 \frac{E\_res_{steel}(x)}{Width\_t \cdot th}}{Width\_t}$$

Curent per surface inout data for FEM

$$I_s := \frac{I}{(Width\_t) \cdot th} = 1.535433071 \times 10^7 \frac{A}{m^2}$$

A.11 EXPERTA REPORT

EXPERTA | TESTING

Canadastraat 20
NL-5651 CG Eindhoven
www.experta-testing.com

Test Report: Thermal Conductivity & Heat Capacity of Laminated Composite Materials

Company:	**CTC AIRBUS** DA/355/19/9721 Airbus Straße 1 D-21684 Stade Germany
Contact:	Mr. Harald Dankers Mr. Victor Şutîi
Date:	October 22th, 2019
Written by:	**EXPERTA | TESTING** Mr. Wim Pinnoo Technical & Application Manager

Canadastraat 20
NL-5651 CG Eindhoven
www.experta-testing.com

Table of Contents

Canadastraat 20
NL-5651 CG Eindhoven
www.experta-testing.com

OBJECTIVE

The objective was to determine the thermal conductivity & heat capacity, as important thermal physical properties, of laminated composite samples (PEKK material).

The goal of the measurements is to build (improve) the FEM Model for resistance welding of the thermoplastics. The FEM model will be used to predict the temperature of the welded parts.

APPARATUS

Two different techniques and thus instruments were used for this study.

1) DSC Mettler-Toledo 823e with a Sensor FRS5

A DSC Mettler-Toledo 823e with Sensor FRS, equipped with a gas box for N2 dosing and Haake 90EK intra-cooler was used to perform the Cp-scan from RT till 430°C.

The following test method was programmed:
- Step 1: 50°C for 10min. isothermal
- Step 2: 50°C to 450°C with 5°C/min.
- Step 3: 450°C for 10min. isothermal

During the experiment a 50 ml N2 purge gas and 200 ml N2 dry gas for the intra-cooler were used.

The sample pans used were a 40µl aluminum ref. cup (Weight = 48.159 mg with lid); a 40µl aluminum sample cup (1) (Weight = 48.597 mg with lid) and a second 40µl aluminum sample cup (Weight = 48.191 mg with lid)

2) TCi C-Therm Technologies with a max K HR-sensor

The TCi - Thermal Conductivity instrument from C-Therm Technologies Ltd. was used in this study to perform all the thermal conductivity measurements.

The TCi employs the MTPS - Modified Transient Plane Source – Technology for thermal conductivity measurement.

Canadastraat 20
NL-5651 CG Eindhoven
www.experta-testing.com

SAMPLES

SAMPLE NAME: PEKK

QIL = Quasi Isothermal Laminate
UD = Unidirectional laminate
Insulator Material

Photo 1: QIL

Photo 2: UD

Photo 3 : Insulator

Photo 4 : Glues blocks for all samples (with X direction indicated)

Canadastraat 20
NL-5651 CG Eindhoven
www.experta-testing.com

Reference Test

1) Heat Capacity (Cp) via DSC

To validate the DSC instrument to be able to perform Cp-analysis, several “blanc” & “sapphire runs” must be performed (with an identical temperature program) to ensure a good reproducibility of the results.

For this specific study, two “blanc runs” and two “sapphire runs” were executed. Afterwards, the samples were measured and Cp was calculated via software acc. DIN51007 method.

The standard reference material was a Sapphire 99,999% pure (Weight = 22.818 mg).

The blanc & sapphire runs are shown with the result curves, below.

2) Thermal Conducivity with TCi

An instrument validation was performed prior to running any tests.

NIST-standard reference materials were used. This test confirmed the instrument was performing well, within the stated accuracy specification of <5% and precision <1%.

The accuracy of the measurements conducted under specific environmental conditions can be examined by measuring reference materials with externally certified thermal conductivity values.

In comparing the observed measurements of the materials with the known thermal conductivity values of the materials, the accuracy of the measurements for unknown samples can be evaluated and the precision of the instrument can be determined.

The results for the reference validation for the measurements carried out in this study are listed below:

Pyrex (Polymer Calibration):
Nominal Value = 1.137W/mK: Measured Value 1.158W/mK (Error = +1.80%)

Pyroceram (Ceramic Calibration)
Nominal Value = 4.080W/mK: Measured Value = 4.226W/mK (Error = +3.45%)

Canadastraat 20
NL-5651 CG Eindhoven
www.experta-testing.com

RESULTS

Heat Capacity (Cp) via DSC:

Sample: DSC CP Sample 1 QIL specimens, 18.2930 mg
Cp by Sapphire

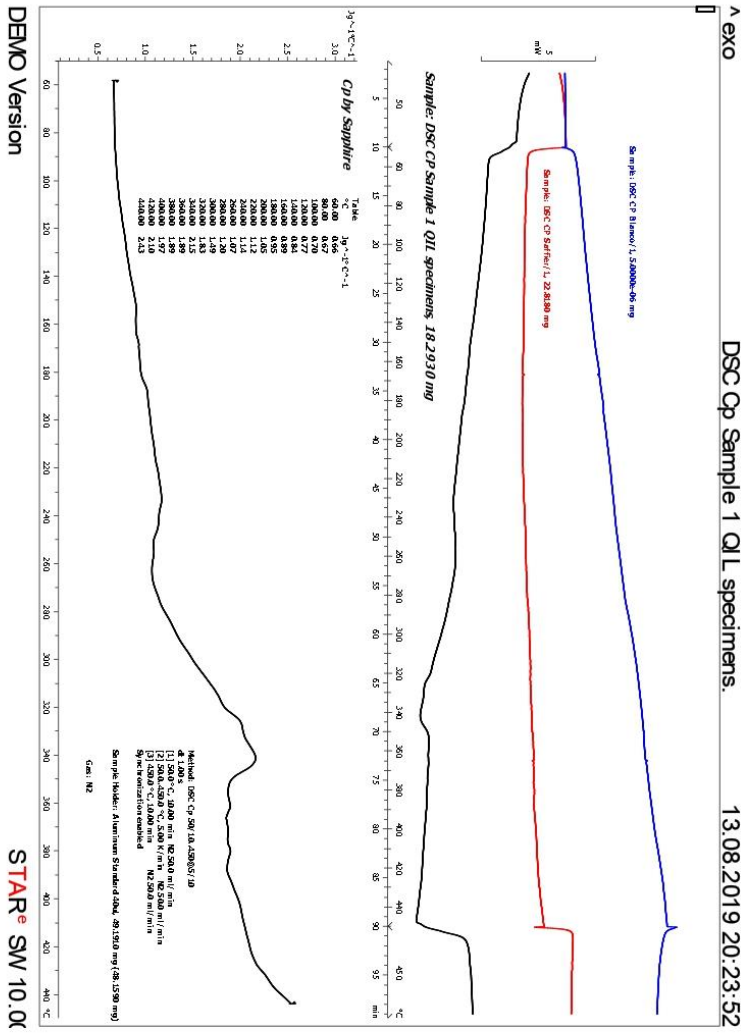

Canadastraat 20
NL-5651 CG Eindhoven
www.experta-testing.com

Quasi-isotrop

X - Direction	Thermal Conductivity (TC)	Heat Capacity (Cp)	Corrected by DSC data Heat Capacity (Cp)	Checked by DSC Scan	Density
@RT	2.240	1263.45	1263.45		1546
@40°C	2.405		1274.09		1545
@60°C	2.571		1284.73		1545
@80°C	2.736		1295.37		1544
@100°C	2.901	1306.01	1306.01		1543
@120°C	2.954		1311.15		1541
@140°C	3.008		1316.29		1539
@160°C	3.061		1321.42		1537
@180°C	3.114	1326.56	1326.56		1535
@200°C	3.122		1330.01		1539
@220°C	3.130		1333.47		1543
@240°C	3.138		1336.93		1547
@260°C	3.147		1340.41		1551
@280°C	3.155		1343.90		1555
@300°C	3.163		1347.39		1559
@320°C	3.171		1350.89		1563
@340°C	3.179		1354.40		1567
@360°C	3.188		1357.93		1571
@380°C	3.196		1361.46		1575
@400°C	3.204		1365.00		1579
@420°C	3.213		1368.55		1583
@440°C	3.221		1372.10		1588

Z - Direction	Thermal Conductivity (TC)	Heat Capacity (Cp)	Corrected by DSC data Heat Capacity (Cp)	Checked by DSC Scan	Density
@RT	0.676	1038.81	621.76	620	1546
@40°C	0.685	1040.57	641.76	640	1545
@60°C	0.693	1042.34	661.76	660	1545
@80°C	0.702	1044.10	681.76	670	1544
@100°C	0.710	1045.86	701.76	700	1543
@120°C	0.722	1051.33	768.40	770	1541
@140°C	0.733	1056.80	835.03	840	1539

Canadastraat 20
NL-5651 CG Eindhoven
www.experta-testing.com

@160°C	0.745	1062.27	901.67	890	1537
@180°C	0.756	1067.74	968.30	950	1535
@200°C	0.768	1073.21	1034.93	1050	1533
@220°C	0.779	1078.68	1101.57	1120	1531
@240°C	0.791	1084.15	1168.20	1140	1529
@260°C	0.802	1089.62	1234.84	1070	1527
@280°C	0.814	1095.09	1301.47	1200	1524
@300°C	0.825	1100.56	1368.11	1490	1522
@320°C	0.837	1106.03	1434.74	1830	1520
@340°C	0.848	1111.50	1501.38	2150	1518
@360°C	0.860	1116.97	1568.01	1890	1516
@380°C	0.871	1122.44	1634.64	1890	1514
@400°C	0.883	1127.91	1701.28	1970	1512
@420°C	0.894	1133.38	1767.91	2100	1510
@440°C	0.906	1138.85	1834.55	2430	1508

Canadastraat 20
NL-5651 CG Eindhoven
www.experta-testing.com

Sample: DSC CP Sample 1 UD ply specimens, 18.3440 mg
Cp by Sapphire

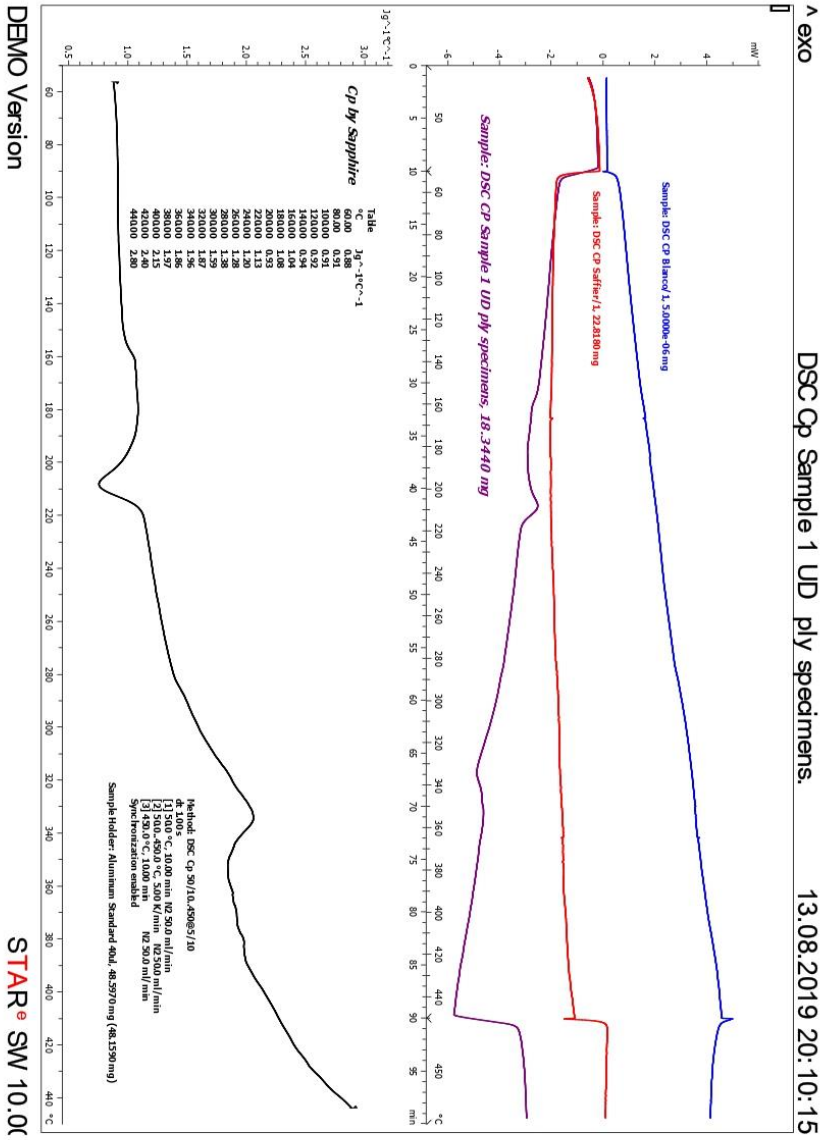

Canadastraat 20
NL-5651 CG Eindhoven
www.experta-testing.com

Uni-directional

X - Direction	Thermal Conductivity (TC)	Heat Capacity (Cp)	Corrected by DSC data Heat Capacity (Cp)	Checked by DSC Scan	Density
@RT	3.301	1330.53	1330.53		1547
@40°C	3.529		1346.200		1522
@60°C	3.756		1361.870		1496
@80°C	3.984		1377.540		1471
@100°C	4.211	1393.21	1393.21		1445
@120°C	4.263		1398.488		1388
@140°C	4.315		1403.765		1331
@160°C	4.366		1409.043		1274
@180°C	4.418	1414.32	1414.32		1217
@200°C	4.424		1416.280		1215
@220°C	4.430		1418.243		1214
@240°C	4.436		1420.209		1212
@260°C	4.443		1422.177		1210
@280°C	4.449		1424.148		1209
@300°C	4.455		1426.122		1207
@320°C	4.461		1428.099		1205
@340°C	4.467		1430.078		1204
@360°C	4.473		1432.060		1202
@380°C	4.480		1434.045		1200
@400°C	4.486		1436.033		1199
@420°C	4.492		1438.023		1197
@440°C	4.498		1440.016		1195
Y - Direction	Thermal Conductivity (TC)	Heat Capacity (Cp)	Corrected by DSC data Heat Capacity (Cp)	Checked by DSC Scan	Density
@RT	0.676	1038.81	827.15	820	1547
@40°C	0.685	1045.96	849.65	850	1546
@60°C	0.693	1053.11	872.15	880	1546
@80°C	0.702	1060.26	894.65	910	1545
@100°C	0.755	1067.41	917.15	910	1544
@120°C	0.767	1073.45	959.65	920	1542
@140°C	0.778	1079.48	1002.15	940	1540

Canadastraat 20
NL-5651 CG Eindhoven
www.experta-testing.com

@160°C	0.790	1085.52	1044.65	1040	1538
@180°C	0.811	1091.55	1087.15	1080	1536
@200°C	0.823	1097.59	1129.65	930	1534
@220°C	0.834	1103.62	1172.15	1130	1532
@240°C	0.846	1109.66	1214.65	1200	1530
@260°C	0.857	1115.69	1257.15	1280	1528
@280°C	0.869	1121.73	1299.65	1380	1525
@300°C	0.880	1127.76	1342.15	1590	1523
@320°C	0.892	1133.80	1384.65	1870	1521
@340°C	0.903	1139.83	1427.15	1960	1519
@360°C	0.915	1145.87	1469.65	1860	1517
@380°C	0.926	1151.90	1512.15	1970	1515
@400°C	0.938	1157.94	1554.65	2150	1513
@420°C	0.949	1163.97	1597.15	2400	1511
@440°C	0.961	1170.01	1639.65	2800	1509

Insulator Material

Z - Direction	Thermal Conductivity (TC)	Heat Capacity (Cp)	Density
@RT	0.346	684.21	2127

CONCLUSION

We were able measure the thermal conductivity according the TCi - instrument (C-Therm Technologies) specification at room temperature (RT); 100°C & 180°C.

All TC measurements were conducted with contact agent; and a weight of 500g to ensure a low contact resistance between the sample surface (smoothed by the customer) and the sensor surface.

For this study the main uncertainties are:

- Std. reference materials (<5% from Nominal value is guaranteed by NIST)
- Calibration TCi sensor (see validation data and accepted to be <5%)
- DSC calibration (acc. DIN51007 = <3%)

Further we were able to calculate (extrapolate) the thermal conductivity above the 180°C, based on the results obtained by DSC acc. DIN51007 method "

EXPERTA | TESTING cannot be held responsible for possible inaccuracies, errors or miscalculations in the results, nor can it be held responsible for any damage resulting from these inaccuracies, errors or miscalculations.